Understanding the degradation mechanisms of organic-inorganic halide perovskite solar cells

トゥメンウルズィ, ガンバータル

https://hdl.handle.net/2324/4110481

出版情報：Kyushu University, 2020, 博士（工学）, 課程博士
バージョン：
権利関係：

2020

Doctor Thesis

Understanding the degradation mechanisms of organic-inorganic halide perovskite solar cells

Ganbaatar Tumen-Ulzii

Department of Chemistry and Biochemistry
Graduate School of Engineering
Kyushu University

Contents

Chapter 1:

General introduction

1.1 Perovskite materials

1.1.1 Crystalline structures

A mineral of calcium titanate ($CaTiO_3$) was found in the Ural Mountains of Russia by Russian mineralogists in the nineteenth century. Later, the crystalline structure of this mineral was studied by German scientist, Gustav Rose, in 1839.[1] He reported that this material had a three-dimensional (3D) crystal structure with corner-sharing TiO_6 octahedra and Ca atoms being present in the cavity of the cubic unit cell as shown in **Fig. 1-1**. Then, he named the mineral as “perovskite” in honor of Count Lev Aleksevich von Perovski, a Russian mineralogist. After this discovery, the term “perovskite” has been used to refer to a wide variety of materials with the ABX_3 crystalline structure with different composition.

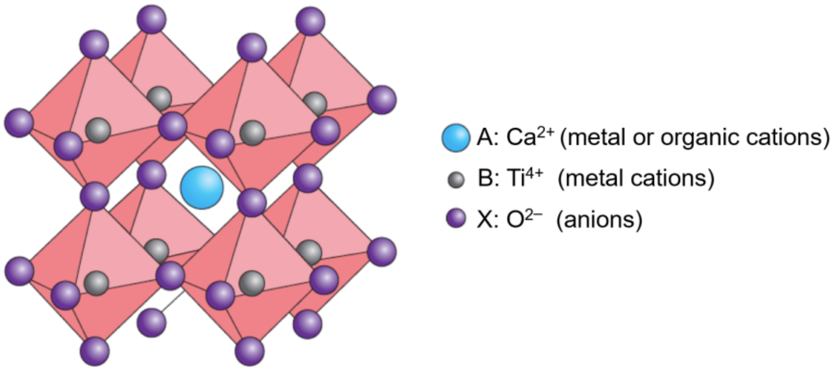

Figure 1-1. General crystalline structure of a perovskite.

Organic-inorganic halide hybrid perovskites are known as a family of the aforementioned perovskites. The first example of hybrid perovskites with the ABX_3 structure, where A is the organic cation (for example, methylammonium, MA); B is the lead (II) ion, and X is the halogen (Cl, Br, or I), was developed by Weber in 1978.[2] Recently, hybrid perovskites have emerged for use in opto-electronic applications. The simplest composition of a hybrid perovskite is methylammonium lead triiodide ($MAPbI_3$), which has been studied thoroughly by many researchers. For the crystal structure of $MAPbI_3$, it is known that the corner sharing PbI_6 octahedra is connected with MA cations in the octahedral interstices by van der Waals attraction as shown in **Fig. 1-2**a.

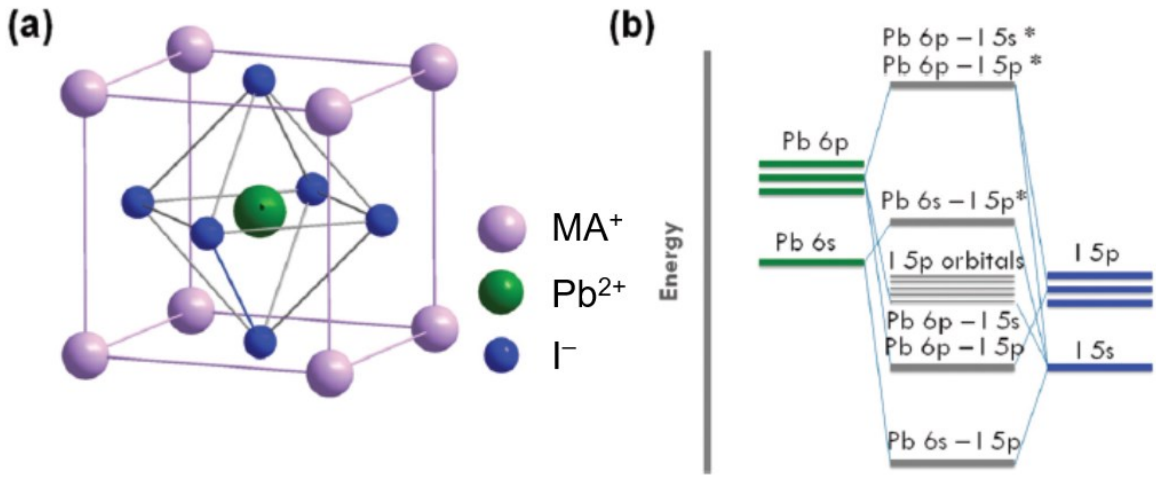

Figure 1-2. a) Crystal structure of a hybrid perovskite material. b) Electronic band structure of the representative $MAPbI_3$ perovskite. Green and blue lines refer to atomic orbital energies (p and s) of Pb and I, respectively. These figures are reproduced from Ref. 8.

Several crystal phases, such as tetragonal, orthorhombic, trigonal and cubic polymorphs, which have different lattice tilting angles of the octahedra, were discovered in the perovskite-structured materials. Furthermore, depending on external stimulus of temperature, electrical bias and environment, phase transitions between their polymorphs take place.[3] The crystal phases and stability of the perovskites are determined by the Goldschmidt tolerance factor which takes account of the ionic radii.[4] The Goldschmidt tolerance factor (t) is introduced with eq. 1-1:

$$t = \frac{r_A + r_X}{\sqrt{2}(r_B + r_X)} \qquad (1\text{-}1)$$

where r_A, r_B and r_X are the radii of ions at the A, B and X sites, respectively, in the perovskites. The t value of the ideal 3D cubic perovskite is equal to 1.0. However, experimentally, t values of most cubic perovskites are in the range of 0.8–0.9.[5] If the t

value is lower than 0.8 or larger than 1.0, the perovskite structure is distorted, and less symmetric tetragonal and orthorhombic phases are observed.[3] Especially, with the *t* value greater than 1.0, 3D perovskite structures are split into lower-dimensional perovskite structures, such as two-dimensional (2D) perovskites.[6] In this regard, large organic cations are typically used to make 2D perovskites.

Besides the crystal structure, charge balancing should be kept at zero in the perovskites' ABX_3 composition. The charge balancing is expressed by the following eq. 1-2.

$$q^A + q^B + 3q^X = 0 \qquad (1\text{-}2)$$

where q^A, q^B and q^X are the charges of ions at the A, B and X sites, respectively. Following eq. 1-2, various types of perovskites can be designed. For example, hybrid perovskites can be formed by using different metal ions (II) on the B site and halogens (Cl, Br, I) on the X site. The well-known hybrid perovskite family used in opto-electronics is methylammonium lead halides such as $MAPbCl_3$, $MAPbBr_3$, and $MAPbI_3$.

1.1.2 Perovskite material properties

While the organic cations at the A site mainly moderate the crystalline structure by tuning the *t* factor, B and X sites determine the opto-electronic properties.[7] The band structure of the perovskite is mainly dependent on the inorganic PbI_6 octahedra. In $MAPbI_3$, while the valence band maxima (VBM) originates from the σ bonding orbital composed of Pb 6s–I 5p, the conduction band minima (CBM) originates from σ and π antibonding orbitals of Pb 6p–I 5s and Pb 6p–I 5p, respectively.[8] Indeed, the band gap of $MAPbI_3$ is mainly related to the PbI_6 octahedra, which is consistent with results from first principles modelling.[9,10] The organic cation of the A site has no direct effect on the electronic structure, but there is an indirect influence because it can be responsible for a change in the crystal structure. A replacement of A-site cations with bigger or smaller cations with different ionic radii affects the Pb–I bond length or Pb–I–Pb bond angle, resulting in a small change in the band structure and band gap.[11] By replacing the iodine (I) at the X site of $MAPbI_3$ by Br or Cl, a significant change in bandgap is observed, while there is a negligible change by replacing the A site of $MAPbI_3$ with bigger ions, such as the formamidinium (FA) cation.[11] The bandgaps of $MAPbI_3$, $MAPbBr_3$ and $MAPbCl_3$ are reported at 1.51, 2.22 and 3.11 eV, respectively.[12,13] Furthermore, by using a mixed composition of halogens at the X site ($MAPbI_{3-x-y}Br_xCl_y$), the bandgaps are continuously tunable between 1.51–3.11 eV.[11]

A sharp absorption edge around the bandgap energy with negligible absorption below the bandgap for $MAPbI_3$ leads to a low Urbach energy of ~14 meV, which indicates the highly ordered crystalline structure.[13] The absorption coefficient of $MAPbI_3$ is greater than 10^5 cm^{-1} over the visible light spectrum. Furthermore, the exciton binding energy of this perovskite is only ~10 meV. Indeed, excitons are easily separated into free charges at room temperature.[13] The room-temperature thermal energy of ~26 meV is already enough to dissociate the photogenerated excitons with such low binding energy into free electrons and holes. Additionally, perovskites have high carrier mobilities of tens of $cm^2/(V\ s)$[14] and long charge-carrier diffusion lengths in the micrometer (μm) range[15] even in solution-processed films.

With the unique opto-electronic properties, such as tunable band gaps, high absorption coefficients, low exciton binding energy, high carrier mobilities, and long carrier diffusion lengths, perovskites are excellent materials for diverse opto-electronic applications such as solar cells, light-emitting diode, field-effect transistors and lasing applications.

1.2 Perovskite solar cells

In 2009, the research group of Professor Tsutomu Miyasaka in Toin University of Yokohama, Japan discovered the first solar cells using hybrid perovskite materials as the light absorber.[16] By taking the aforementioned advantages, perovskites can be used for efficient harvesting of solar energy into electricity. Especially, the tunable bandgaps make the perovskites promising for use in solar cells to reach the Shockley–Queisser limit of power conversion efficiency.[17] Additionally, compatibility with simple solution processing is an additional advantage of using perovskites,[18] which lowers the fabrication cost of perovskite solar cells (PSCs) compared to widely used silicon-based technology in future. **Figure 1-3** shows the certified power conversion efficiencies (PCEs) of silicon-based solar cells and PSCs, which are provided from the National Renewable Energy Laboratory (NREL, USA).[19] The certified PCEs of PSCs have already reached a very high level of up to 25.2 %, which is comparable to silicon solar cell technology. This high efficiency was achieved within <10 years of research after the first discovery by Prof. Miyasaka.

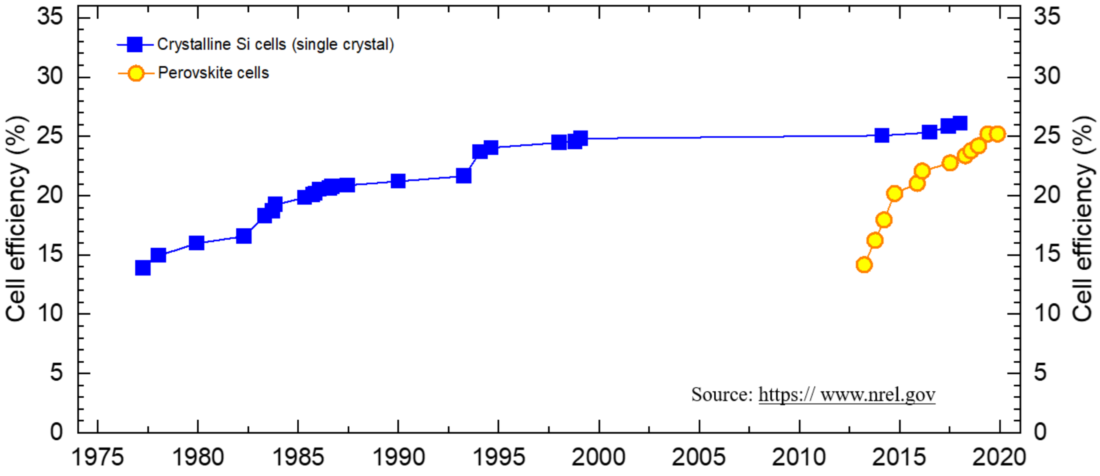

Figure 1-3. Efficiency evolution of silicon-based solar cells and PSCs.

1.2.1 Working principles of perovskite solar cells

Solar cells are devices that convert light energy (photons) into electrochemical energy (charged carriers or electricity). Here, the general working principle of solar cells will be explained (see **Fig. 1-4**).

(i). The light (photons) transmitted through a glass substrate and transparent conductive oxide (TCO) electrode is absorbed by the perovskite layer. The photons with an energy equal to or larger than the bandgap of the perovskite layer optically excite the electrons from the valence band to the conduction band to form excitons.

(ii). The excitons then dissociate into free electrons and holes by thermal energy since the exciton binding energy of the perovskite is typically lower than the room-temperature thermal energy.

(iii). The dissociated free electrons and holes diffuse and are extracted into a neighboring electron transport layer (ETL) and hole transport layer (HTL) by an internal electric field as the driving force to reach the electrodes.

(iv). Then, the respective electrons and holes are transported through the ETL and HTL and finally collected by the cathode and anode.

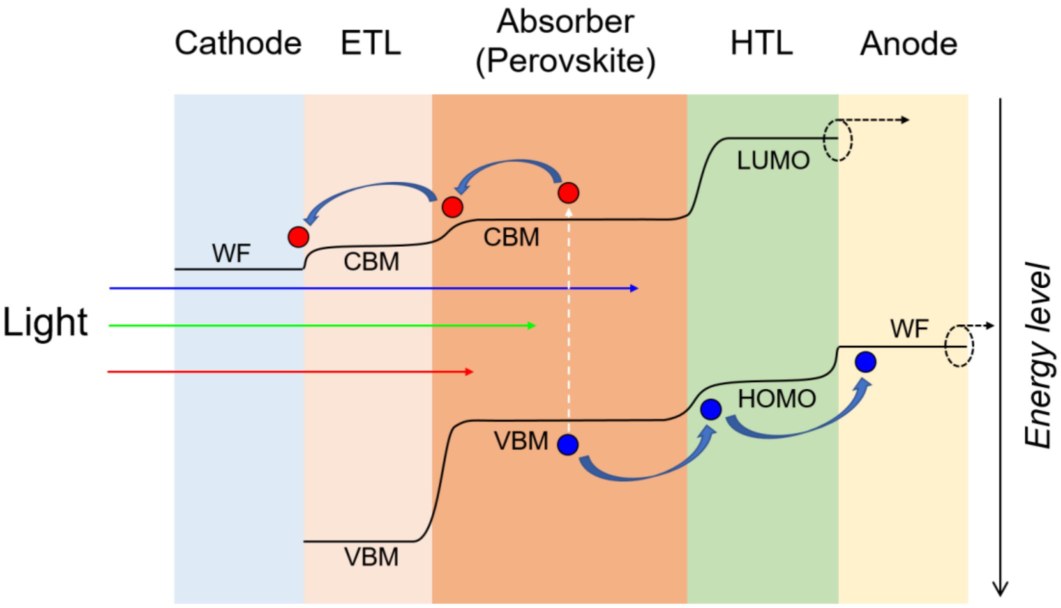

Figure 1-4. a) Device architecture of PSCs and their working mechanisms. WF: Work function; CBM: Conduction band minima; VBM: Valence band maxima; LUMO: Lowest unoccupied molecular orbital; HOMO: Highest occupied molecular orbital;

The standard performance of PSCs can be derived from current density versus voltage (*J*–*V*) curves under illumination measured under solar light illumination with an intensity of 100 mW cm^{-2} at room temperature (~25 °C). The solar light source has a spectrum of air mass 1.5 global radiation (AM 1.5G). The AM 1.5G spectrum is defined as light reaching on the surface of the earth at a zenith angle of 48.2°. **Figure 1-5** shows a typical *J*–*V* curve of PSCs. From the *J*–*V* curve, the current densities (*J*) are measured as a function of applied voltages (*V*). The output powers (*P*) generated from PSCs can be calculated as the product of *J* and *V*. The *P*–*V* curve is drawn in the same figure. From the *J*–*V* and *P*–*V* curves, the following parameters are extracted:

P_{max}: maximum power	MPP: maximum power point
J_{max}: maximum current density	J_{SC}: short-circuit current density

$V_{\max}$: maximum voltage V_{OC}: open-circuit voltage

The MPP is the point, at which the $P_{\max}$ is obtained. The values of J and V at the MPP are called $J_{\max}$ and $V_{\max}$, respectively. J_{SC} indicates the generated current density at the short-circuit condition (zero voltage), and V_{OC} indicates the generated voltage at the open circuit condition (zero current). The power conversion efficiency (PCE) is calculated by Equ. 1-3:

$$\mathrm{PCE} = \frac{P_{\max}}{P_{in}} = \frac{J_{\max} \times V_{\max}}{P_{in}} = \frac{J_{SC} \times V_{OC} \times \mathrm{FF}}{P_{in}} \qquad (1\text{-}3)$$

where P_{in} is the incident power, which is typically 100 mW cm^{-2}. FF is the fill factor, which indicates how efficiently the PSC generates the power. The FF is calculated by Equ. 1-4 below:

$$\mathrm{FF} = \frac{J_{\max} \times V_{\max}}{J_{SC} \times V_{OC}} \qquad (1\text{-}4)$$

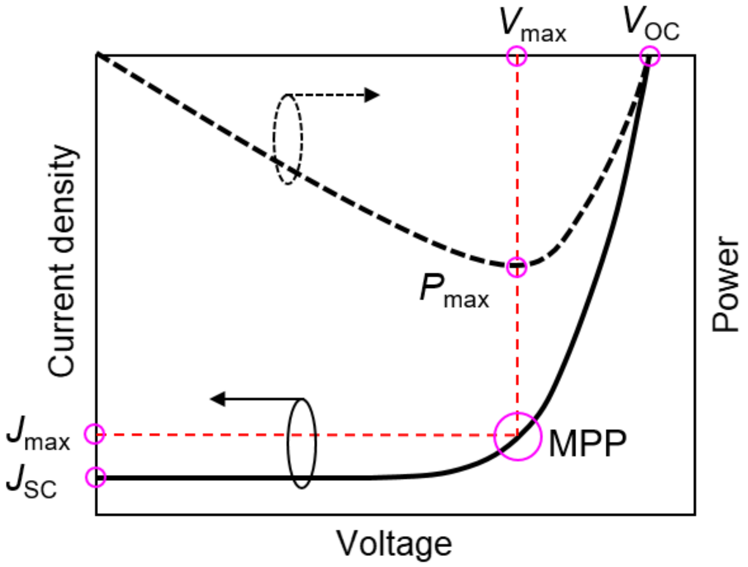

Figure 1-5. Typical J–V and P–V curves of PSCs.

1.2.2 Device architecture

As illustrated in **Fig. 1-6**, the device architectures of PSCs can be divided into three categories: (1) mesoporous n-i-p heterojunction (hereafter abbreviated as “meso”), (2) planar n-i-p heterojunction (hereafter abbreviated as “planar”), and (3) p-i-n heterojunction (hereafter abbreviated as “inverted” because the layer sequence in this architecture is completely opposite from the meso and planar architectures).

Figure 1-6a illustrates the mesoporous architecture. Up to now, titanium dioxide (TiO_2) has been used as the porous ETL in this mesoporous architecture. A part of the perovskite material fills the pores of a TiO_2-based porous network and the other perovskite material forms a continuous perovskite layer on top of it. Then, the HTL is deposited on top of the perovskite layer. Finally, the metal electrode is deposited. The advantage of this architecture is that excellent electron extraction can be obtained even though perovskites have a short carrier diffusion length compared to the film thickness. For example, the reported diffusion length of $CH_3NH_3PbI_3$ is ∼100 nm,[15,20] but $CH_3NH_3PbI_3$ with a thickness >300 nm is required to efficiently absorb the light.[21] Therefore, a mesoporous TiO_2 network is necessary for efficiently transporting the electrons and holes to the collecting electrodes. However, the mesoporous TiO_2-based architecture has a disadvantage of the significant PSC degradation associated with UV-light induced photocatalytic activity of the TiO_2 layer. In addition, high-temperature processing at ~500 °C for the mesoporous TiO_2 layer makes the PSC fabrication cost higher.

In contrast, the planar heterojunction architecture is simpler than the mesoporous architecture as illustrated in **Fig. 1-6**b. The difference between these two architectures is that no mesoporous layer is included in the planar architecture. However, the planar architecture is not suitable for PSCs with thick perovskite films, if the diffusion length of the perovskite layer is shorter than the film thickness, as mentioned in the previous paragraph. However, perovskites with mixed halide composition have longer carrier diffusion length over 1 μm,[15] which, therefore, makes it possible to use the planar heterojunction architecture in PSCs. Thus, this architecture has widely been used in recent years in combination with a wide-bandgap tin oxide (SnO_2) based ETL. SnO_2 is more stable than TiO_2 in terms of UV-light induced degradation being suppressed. In addition, SnO_2-based ETLs can be prepared at a low temperature of < 150 °C.[22] Therefore, I have chose this planar device architecture with SnO_2 for the experiments in this thesis.

Figure 1-6c illustrates the inverted architecture, which is mainly based on a poly(3,4-ethylenedioxythiophene) polystyrene sulfonate (PEDOT: PSS) HTL. This architecture allows the low-temperature fabrication similar to the planar architecture. However, PCEs of PSCs fabricated with this architecture are usually lower than those of the other two architectures. The reason of lower PCEs is still not clear. Nevertheless, it could be related to different quality of perovskite films on top of PEDOT: PSS and TiO_2/SnO_2, and different energy level alignment between different device architectures. Furthermore, the device stability associated with unstable PEDOT: PSS under ambient conditions is a serious problem hindering the use of this architecture.

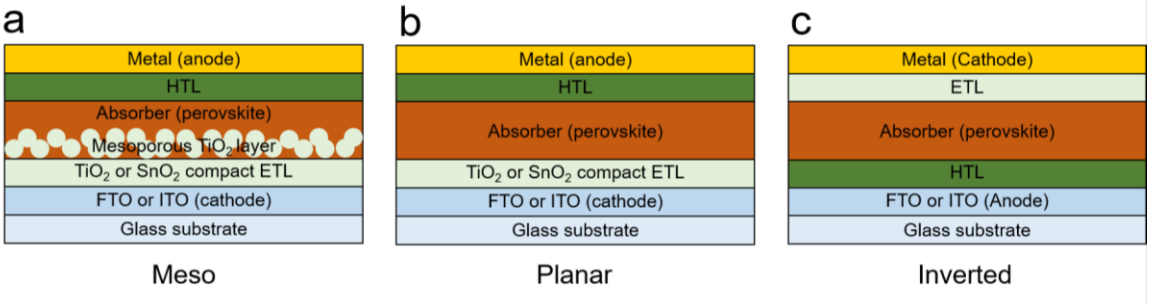

Figure 1-6. a) Meso, b) planar, and c) inverted architectures of PSCs.

1.2.3 Deposition methods for the perovskite absorber layer

Solution-processed PSCs have shown a remarkable performance development in the last decade. The PCEs of PSCs have climbed to 25.2% from 3.8% after their first discovery in 2009.[16,19] One of the most important contributions to this great performance development is the improvement of crystal growth to obtain higher-quality perovskite films by solution processing.[23] The solvent engineering is a key to control the crystal growth, which indeed affects the uniformity and surface morphology of the perovskite layer.

Spin coating has usually been used to deposit a perovskite film on substrates. The spin-coating processes include that a small amount of a precursor solution is dropped onto a substrate and then the substrate is rotated (spun) to form a film. The film thickness can be controlled by the concentration of the precursor solution and the rotation speed. Below, the development of spin coating techniques for the perovskite film deposition is summarized.

Two-step deposition (in other words, sequential solution deposition).

At the earlier stage of the spin-coting development, the perovskite films were deposited through a one-step spin coating technique, for which a precursor solution in

N,N-dimethylformamide (DMF) is dropped onto the substrate and this substrate is rotated at a certain speed for a certain time.[16] However, the film quality was poor because of many pinholes and small grains being formed in films. In addition, the reproducibility was not good.

Later, Prof. Michael Graetzel's group developed a two-step deposition (sequential) process to achieve more uniform, dense perovskite films.[24] To fabricate $MAPbI_3$ films with this method, a lead iodide (PbI_2) film is firstly deposited by spin-coating. Subsequently, this PbI_2 film is immersed into a MAI solution in isopropanol. The MAI is infiltrated into the PbI_2 film, forming dense and uniform perovskite films. With this method, MAI is difficult to reach the bottom of the PbI_2 film, so a large amount of unreacted PbI_2 remains at the bottom of the films, resulting in the incomplete conversion to the perovskite and limited PSC performance.

One-step deposition with anti-solvent.

It has been understood that the reason for the poor film quality when the perovskite film is prepared by the one-step deposition method from a DMF solution is due to rapid formation of perovskite crystals during the spin-coating.[24] Recently, the formation of PbI_2- dimethyl sulfoxide (DMSO)-MAI adduct approach has been discovered. Using the adduct slows down the formation of crystals during the spin-coating because of the formation of an intermediate phase in films. After annealing, the intermediate phase is converted into the perovskite structure.[25] In addition, introducing an anti-solvent such as toluene, chlorobenzene, diethyl ether, etc. into the intermediate phase during the substrate spinning improves the quality of resulting perovskite films very much.[23] The solvent that is used as the anti-solvent should not dissolve the perovskite layer.[26] This anti-solvent engineering enabled uniform, pinhole-free, highly crystalline perovskite films. Furthermore, the PSCs with the highest PCEs achieved so far were processed with this anti-solvent method.

In contrast, the spin-coating methods could be incompatible with the large-area film fabrication for industrial applications. Spin-coated large-area perovskite films are not uniform over a large substrate. In addition, during the spin-coating, a large amount of a precursor solution and an anti-solvent are wasted. Therefore, using spin-coating for large-area films is still challenging. Nevertheless, spin-coating is a very useful technique to study PSCs at the fundamental scientific level before the industrial stage.

Scalable deposition methods

For the large-scale production of PSCs, researchers have investigated various coating methods for perovskite films. The examples of solution-based large-scale perovskite film fabrication processes are roll-to-roll printing, spray coating, slot-die coating, and doctor blading.[18] In addition, vacuum evaporation and chemical vapor deposition methods are also promising[18].

1.2.4 Progress of perovskite solar cells

The progress of PSCs is summarized in **Table 1**, along with their device architectures, perovskite absorber compositions and deposition methods for the perovskite layers. Regarding the architectures, the mesoporous TiO_2-based architecture had mainly achieved the highest PCEs until 2018. However, the SnO_2-based planar heterojunction architecture has emerged very recently because of its high PCEs and operational stability. For the deposition methods, the one-step anti-solvent spin coating method has widely been used for fabricating highly efficient PSCs. Sometimes, the champion PCEs have been obtained independent of deposition methods if the film quality is high enough.[27,28]

The most widely studied perovskite absorber material used in PSCs was $MAPbI_3$ since the world-first PSCs were fabricated using this perovskite.[16] The first PSCs with $MAPbI_3$ and liquid electrolyte delivered a PCE of 3.8%. However, it was difficult to obtain stable and reproducible results because of dissolution of the perovskite layer in the electrolyte.[16] Later in 2012, a solid hole conductor 2,2',7,7'-tetrakis[*N*,*N*-di(4-methoxyphenyl)amino]-9,9'-spirobifluorene (spiro–OMeTAD) was employed instead of the liquid electrolyte, leading to PCEs of 9%, with good operational stability.[29] However, fabricating a dense, uniform, highly crystalline $MAPbI_3$ film with the simple one-step deposition method was difficult at this stage. In 2013, the two-step sequential deposition method was found to fabricate higher quality perovskite films. PSCs fabricated with this method offered over 15% of PCE.[24] At the earlier stage of the PSC development, researchers mainly focused on the fabrication methods such as one-step or two-step methods to obtain higher-quality $MAPbI_3$ perovskite films. However, $MAPbI_3$ has many disadvantages such as carrier trap formation, easy phase transition and instability at high temperature.[30] Therefore, it was required to find other light absorber candidates or methods to improve the quality of perovskite films. In this flow of the research, the partial replacement of iodine with other halogens (Br or Cl) provided an increase in perovskite film quality and PCEs of PSCs.[23]

Prof. Sang Il Seok's group used the mixed halide composition of $MAPbI_{3-x}Br_x$ with a small fraction of Br. This mixed composition led to the formation of the more stable cubic perovskite phase along with improved charge transport. They reported that

15% of Br substitution is effective in improving the PCEs and stability. In addition, they introduced a novel spin-coating method, which is one-step spin-coating with anti-solvent quenching. With this anti-solvent technique and mixed halide perovskite composition, they achieved a PCE of 16.15% in 2014.[23] After their work, the anti-solvent-based one-step spin coating method has been used frequently.

Another commonly studied perovskite material is formamidinium lead triiodide ($FAPbI_3$). It is more stable at high temperature compared with $MAPbI_3$ because of bigger organic cations at the A site of the perovskite structure. Furthermore, the bandgap of $FAPbI_3$ is ~1.46 eV, which is slightly smaller than the band gap of $MAPbI_3$ (1.53 eV). Thus, it is expected that $FAPbI_3$ is able to absorb light more efficiently at longer wavelengths and deliver a higher PCE. In 2015, Lee et al. reported a 16.3% PCE by using the $FAPbI_3$ absorber.[31] $FAPbI_3$ has two polymorphs such as a metastable cubic α-phase and a stable hexagonal δ-phase. Although α-$FAPbI_3$ is stable at high temperature, it is easily transferred into photoinactive δ-$FAPbI_3$ at room temperature in the presence of moisture. Therefore, it is challenging to stabilize the photoactive α-$FAPbI_3$ phase at room temperature.

In 2016, Prof. Sang Il Seok's group developed compositional engineering such as mixing small amount of MA-based perovskite into FA-based perovskites to stabilize the perovskite structure, while using a mixed halide composition to maintain the stability.[32] This is called a "mixed" perovskite. They achieved 18.4% PCEs using the mixed perovskite absorber with the composition of $FA_{0.85}MA_{0.15}Pb(I_{0.85}Br_{0.15})_3$. Furthermore, they discovered that using an excess amount of lead iodide (PbI_2) is beneficial for fabricating less-trap, dense, high-quality mixed perovskite films. Indeed, highly efficient PSCs with over 20% PCE were achieved in other group.[33]

Inorganic alkali cations such as Cs^+, Rb^+, and K^+ are another option to stabilize the perovskite structure by tuning the *t* because of their small ionic radii. Saliba et al. introduced a small amount of Cs^+, into the $FA_{0.85}MA_{0.15}Pb(I_{0.85}Br_{0.15})_3$ mixed perovskite. They found that ~5 mol% of Cs^+ with the composition of $Cs_{0.05}(FA_{0.85}MA_{0.15})Pb(I_{0.85}Br_{0.15})_3$ is enough to improve the phase stability of the perovskite structure. The PCEs of PSCs with this absorber material were as high as 21.1%, with very high reproducibility.[34] Furthermore, the devices had very good operational stability. Since this discovery, Cs containing triple cation perovskites with the composition of $Cs_{0.05}(FA_{0.85}MA_{0.15})Pb(I_{0.85}Br_{0.15})_3$ have frequently been used for highly efficient and stable PSCs up to date.

Very recently, the PSCs with 23.2 and 23.5% champion PCEs were achieved by using modified spiro-OMeTAD and a surface passivation of the perovskite absorber, respectively.[28,35] Also, the highest PCE of 25.2% was certified by NREL, USA in 2019.[19] However, there is no scientific paper escribing this result yet.

Table 1. Progress of perovskite solar cells

Year	Device architecture	Perovskite absorber composite	Deposition method	Main finding and development	PCE (%)	Ref #
2009	Meso	$MAPbI_3$ and $MAPbBr_3$	Simple one-step	The perovskite absorber was used for the first time in solar cell applications. However, its stability and reproducibility were poor due to liquid electrolyte.	3.8	16
2012	Meso	$MAPbI_3$	Simple one-step	A solid HTM of spiro-OMeTAD was employed instead of a liquid electrolyte.	9	29
2013	Meso	$MAPbI_3$	Two-step	A two-step sequential deposition of a perovskite layer was developed.	15.0	24
2014	Meso	$MAPb(I_{0.85}Br_{0.15})_3$	One-step (anti-solvent)	The PbI_2-DMSO based adduct approach with an anti-solvent spin-coating method was reported.	16.1	23
2015	Planar	$FAPbI_3$	One-step (anti-solvent)	FA-based perovskites were used as the absorber layer. But the α-$FAPbI_3$ phase was not stable.	16.3	31
2016	Meso	$FA_{0.85}MA_{0.15}(PbI_{0.85}Br_{0.15})_3$	One-step (anti-solvent)	Mixed cation and mixed anion-based perovskite composition with high stability was reported.	18.4	32
2016	Meso	$FA_{0.85}MA_{0.15}(PbI_{0.85}Br_{0.15})_3$ with excess PbI_2	One-step (anti-solvent)	Excess PbI_2 was used to improve the quality of mixed perovskite films.	20.1	33
2016	Meso	$Cs_{0.05}(FA_{0.85}MA_{0.15})_{0.95}(PbI_{0.85}Br_{0.15})_3$	One-step (anti-solvent)	Cs-containing triple cation mixed perovskites with high stability was reported.	21.1	34
2018	Meso	$FA_{0.95}MA_{0.05}(PbI_{0.95}Br_{0.05})_3$	One-step (anti-solvent)	Use of a modified HTL of spiro-OMeTAD with a suitable HOMO level delivered high PCEs.	23.2	27
2019	Planar	$FA_{0.92}MA_{0.08}PbI_3$	Two-step	Surface passivation of perovskite films by forming a thin layer of 2-D perovskite on top of a 3-D perovskite layer was reported.	23.5	28
2020	N/A	N/A	N/A	N/A	25.2	19

1.3 Open questions for perovskite solar cells

Despite the high PCEs, the degradation of PSCs is still serious and needs to be suppressed for commercialization of this technology[36,37]. The degradation of PSCs mainly proceeds under oxygen and moisture environment. However, it is possible to rule out these extrinsic factors of the degradation by using reliable encapsulation technology. On the other hand, intrinsic degradation factors such as light illumination, ion migration and high temperature are still difficult to solve for realizing stable PSCs.

Excess PbI_2 crystals are often used to obtain high-quality perovskite films for high-performance PSCs[34,38,39]. In contrast, photo-decomposition (photolysis) of PbI_2 under light illumination was reported by Dawood et al.[40]. Schoonman et al. suggested that the photolysis of lead halide is a possible reason for the instability of hybrid perovskites[41]. Thus, the presence of PbI_2 crystals in films is a potential source of perovskite's instability under light illumination. However, how excess PbI_2 crystals affect the long-term stability of PSCs under light illumination has been rarely studied[42–44].

On the other hand, owing to the ionic character of halide perovskite materials, the ion migration through the perovskite absorber layer of PSCs during operation is a potential obstacle for efficient and stable solar power conversion. Ion migration frequently causes *J–V* hysteresis and reduces operational stability[37,45–47]. Various approaches have been employed to reduce ion migration. The reported approaches include compositional engineering of perovskite materials[48], reducing grain boundary density by increasing grain size[49,50], and passivation of grain boundaries using organic materials[28]. However, the current situation is still far from completely blocking the ion migration in perovskite films and devices. Therefore, it is required to understand degradation mechanisms of PSCs associated with the ion migration.

Most of high-performing PSCs reported to date contain a small molecular HTL material of spiro-OMeTAD with proper dopants[27,28,51]. The chemical structure of spiro-OMeTAD is shown in **Fig. 1-7**. Although other small molecules[52–54], polymers[55–57] and inorganics[58–60] have been developed for the HTLs of PSCs, spiro-OMeTAD is still excellent among the reported HTL materials in terms of PCEs. PSCs with spiro-OMeTAD are comparably stable at room temperature[32,51]. However, the stability of PSCs with spiro-OMeTAD at high temperature is poor[61–64]. For future commercialization, it is necessary to ensure the high-temperature stability of PSCs. On the basis of the 2010 International Summit on Organic PV Stability (ISOS) protocol (Roskilde, Denmark)[65], solar cells need to work properly even at high temperatures ranging from 65 to 85 °C.

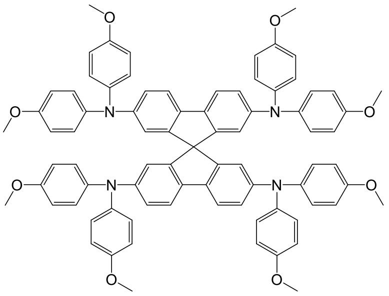

Figure 1-7. Chemical structure of spiro-OMeTAD.

1.4 Aims and outline of this thesis

This thesis focuses on clarifying the degradation mechanisms of PSCs associated with light illumination, ion migration and high-temperature operation. By understanding the degradation mechanisms, I developed highly stable PSCs under operation. In Chapter 2, I investigate the effect of stoichiometry of precursor solutions of perovskites on the stability of PSCs under continuous light illumination. In Chapter 3, I investigate the ion migration induced degradation mechanisms of PSCs. In Chapter 4, I investigate the effect of high temperature on the stability of PSCs. In Chapter 5, I summarize the obtained results in this thesis and point out future perspectives.

References

[1] G. Rose, *Ann. Phys.* **1839**, *124*, 551.

[2] D. Weber, *Z. Naturforsch.* **1978**, *33b*, 1443.

[3] A. M. Glazer, *Acta Cryst.* **1972**, *B28*, 3384.

[4] V. M. Goldschmidt, *Naturwissenschaften* **1926**, *14*, 477.

[5] A. Amat, E. Mosconi, E. Ronca, C. Quarti, P. Umari, M. K. Nazeeruddin, M. Grätzel, F. De Angelis, *Nano Lett.* **2014**, *14*, 3608.

[6] D. B. Mitzi, *J. Chem. Soc. Dalt. Trans.* **2001**, 1–12.

[7] A. Walsh, *J. Phys. Chem. C* **2015**, *119*, 5755.

[8] T. Umebayashi, K. Asai, T. Kondo, A. Nakao, *Phys. Rev. B* **2003**, *67*, 155405.

[9] F. Brivio, A. B. Walker, A. Walsh, *APL Mater.* **2013**, *1*, 042111.

[10] E. Mosconi, A. Amat, M. K. Nazeeruddin, M. Grätzel, F. De Angelis, *J. Phys. Chem. C* **2013**, *117*, 13902.

[11] T. Jesper Jacobsson, J. P. Correa-Baena, M. Pazoki, M. Saliba, K. Schenk, M. Grätzel, A. Hagfeldt, *Energy Environ. Sci.* **2016**, *9*, 1706.

[12] N. Kitazawa, Y. Watanabe, Y. Nakamura, *J. Mater. Sci.* **2002**, *37*, 3585.

[13] S. De Wolf, J. Holovsky, S. J. Moon, P. Löper, B. Niesen, M. Ledinsky, F. J. Haug, J. H. Yum, C. Ballif, *J. Phys. Chem. Lett.* **2014**, *5*, 1035.

[14] L. M. Herz, *ACS Energy Lett.* **2017**, *2*, 1539.

[15] S. D. Stranks, G. E. Eperon, G. Grancini, C. Menelaou, M. J. P. Alcocer, T. Leijtens, L. M. Herz, A. Petrozza, H. J. Snaith, *Science* **2013**, *342*, 341.

[16] A. Kojima, K. Teshima, Y. Shirai, T. Miyasaka, *J. Am. Chem. Soc.* **2009**, *131*, 6050.

[17] Z. Yang, A. Rajagopal, A. K. Y. Jen, *Adv. Mater.* **2017**, *29*, 1704418.

[18] L. Qiu, L. K. Ono, Y. Qi, *Mater. Today Energy* **2018**, *7*, 169.

[19] National renewable energy laboratory. Best research-cell efficiency chart. https://www.nrel.gov/pv/assets/pdfs/best-research-cell-efficiencies.20200406.pdf. (accessed: April 14, 2020).

[20] G. Xing, N. Mathews, S. Sun, S. S. Lim, Y. M. Lam, M. Graẗzel, S. Mhaisalkar, T. C. Sum, *Science* **2013**, *342*, 344.

[21] Y. Liu, B. Jin, H. Zhang, Y. Zhang, Y. Kim, C. Wang, S. Wen, B. Xu, C. Im, W. Tian, *ACS Appl. Mater. Interfaces* **2019**, *11*, 14810.

[22] Q. Jiang, L. Zhang, H. Wang, X. Yang, J. Meng, H. Liu, Z. Yin, J. Wu, X. Zhang, J. You, *Nat. Energy* **2017**, *2*, 16177.

[23] N. J. Jeon, J. H. Noh, Y. C. Kim, W. S. Yang, S. Ryu, S. Il Seok, *Nat. Mater.* **2014**, *13*, 897.

[24] J. Burschka, N. Pellet, S. J. Moon, R. Humphry-Baker, P. Gao, M. K. Nazeeruddin, M. Grätzel, *Nature* **2013**, *499*, 316.

[25] N. Ahn, D. Y. Son, I. H. Jang, S. M. Kang, M. Choi, N. G. Park, *J. Am. Chem. Soc.* **2015**, *137*, 8696.

[26] M. Jung, S. G. Ji, G. Kim, S. Il Seok, *Chem. Soc. Rev.* **2019**, *48*, 2011.

[27] N. J. Jeon, H. Na, E. H. Jung, T. Y. Yang, Y. G. Lee, G. Kim, H. W. Shin, S. Il Seok, J. Lee, J. Seo, *Nat. Energy* **2018**, *3*, 682.

[28] Q. Jiang, Y. Zhao, X. Zhang, X. Yang, Y. Chen, Z. Chu, Q. Ye, X. Li, Z. Yin, J. You, *Nat. Photonics* **2019**, *13*, 460.

[29] H. S. Kim, C. R. Lee, J. H. Im, K. B. Lee, T. Moehl, A. Marchioro, S. J. Moon, R. Humphry-Baker, J. H. Yum, J. E. Moser, M. Grätzel, N. G. Park, *Sci. Rep.* **2012**, *2*, 591.

[30] C. Qin, T. Matsushima, T. Fujihara, W. J. Potscavage, C. Adachi, *Adv. Mater.* **2016**, *28*, 466.

[31] J. W. Lee, D. H. Kim, H. S. Kim, S. W. Seo, S. M. Cho, N. G. Park, *Adv. Energy Mater.* **2015**, *5*, 1501310.

[32] N. J. Jeon, J. H. Noh, W. S. Yang, Y. C. Kim, S. Ryu, J. Seo, S. Il Seok, *Nature* **2015**, *517*, 476.

[33] Y. C. Kim, N. J. Jeon, J. H. Noh, W. S. Yang, J. Seo, J. S. Yun, A. Ho-Baillie, S. Huang, M. A. Green, J. Seidel, T. K. Ahn, S. Il Seok, *Adv. Energy Mater.* **2016**, *6*, 1502104.

[34] M. Saliba, T. Matsui, J. Y. Seo, K. Domanski, J. P. Correa-Baena, M. K. Nazeeruddin, S. M. Zakeeruddin, W. Tress, A. Abate, A. Hagfeldt, M. Grätzel, *Energy Environ. Sci.* **2016**, *9*, 1989.

[35] N. J. Jeon, H. Na, E. H. Jung, T. Yang, Y. G. Lee, G. Kim, H. Shin, S. Il Seok, J. Lee, J. Seo, *Nat. Energy* **2018**, *3*, 682.

[36] J. P. Correa-Baena, M. Saliba, T. Buonassisi, M. Grätzel, A. Abate, W. Tress, A. Hagfeldt, *Science* **2017**, *358*, 739.

[37] L. Meng, J. You, Y. Yang, *Nat. Commun.* **2018**, *9*, 5265.

[38] M. Saliba, J. P. Correa-Baena, C. M. Wolff, M. Stolterfoht, N. Phung, S. Albrecht, D. Neher, A. Abate, *Chem. Mater.* **2018**, *30*, 4193.

[39] B. Wook Park, N. Kedem, M. Kulbak, D. Y. Lee, W. S. Yang, N. J. Jeon, J. Seo, G. Kim, K. J. Kim, T. J. Shin, G. Hodes, D. Cahen, S. Il Seok, *Nat. Commun.* **2018**, *9*, 3301.

[40] R. I. Dawood A. J. Forty, M. R. Tubbs, *Proc. R. Soc. A. Math. Phys. Sci.* **1965**, *284*, 272.

[41] J. Schoonman, *Chem. Phys. Lett.* **2015**, *619*, 193.

[42] T. P. Gujar, T. Unger, A. Schönleber, M. Fried, F. Panzer, S. Van Smaalen, A. Köhler, M. Thelakkat, *Phys. Chem. Chem. Phys.* **2017**, *20*, 605.

[43] A. S. Yerramilli, Y. Chen, D. Sanni, J. Asare, N. D. Theodore, T. L. Alford, *Org. Electron.* 2018, 59, 107.

[44] F. Liu, Q. Dong, M. K. Wong, A. B. Djurišić, A. Ng, Z. Ren, Q. Shen, C. Surya, W. K. Chan, J. Wang, A. M. C. Ng, C. Liao, H. Li, K. Shih, C. Wei, H. Su, J. Dai, *Adv. Energy Mater.* **2016**, *6*, 1502206.

[45] C. Eames, J. M. Frost, P. R. F. Barnes, B. C. O'Regan, A. Walsh, M. S. Islam, *Nat. Commun.* **2015**, *6*, 7497.

[46] W. Tress, N. Marinova, T. Moehl, S. M. Zakeeruddin, M. K. Nazeeruddin, M. Grätzel, *Energy Environ. Sci.* **2015**, *8*, 995.

[47] S. Meloni, T. Moehl, W. Tress, M. Franckeviius, M. Saliba, Y. H. Lee, P. Gao, M. K. Nazeeruddin, S. M. Zakeeruddin, U. Rothlisberger, M. Graetzel, *Nat. Commun.* **2016**, *7*, 10334.

[48] T. Bu, X. Liu, Y. Zhou, J. Yi, X. Huang, L. Luo, J. Xiao, Z. Ku, Y. Peng, F. Huang, Y. B. Cheng, J. Zhong, *Energy Environ. Sci.* **2017**, *10*, 2509.

[49] J. Xing, Q. Wang, Q. Dong, Y. Yuan, Y. Fang, J. Huang, *Phys. Chem. Chem. Phys.* **2016**, *18*, 30484.

[50] Y. Hou, S. Scheiner, X. Tang, N. Gasparini, M. Richter, N. Li, P. Schweizer, S. Chen, H. Chen, C. O. R. Quiroz, X. Du, G. J. Matt, A. Osvet, E. Spiecker, R. H. Fink, A. Hirsch, M. Halik, C. J. Brabec, *Adv. Mater. Interfaces* **2017**, *4*, 1700007.

[51] H. Min, M. Kim, S. U. Lee, H. Kim, G. Kim, K. Choi, J. H. Lee, S. Il Seok, *Science* **2019**, *366*, 749.

[52] T. H. Schloemer, T. S. Gehan, J. A. Christians, D. G. Mitchell, A. Dixon, Z. Li, K. Zhu, J. J. Berry, J. M. Luther, A. Sellinger, *ACS Energy Lett.* **2019**, *4*, 473.

[53] Y. C. Kim, T. Y. Yang, N. J. Jeon, J. Im, S. Jang, T. J. Shin, H. W. Shin, S. Kim, E. Lee, S. Kim, J. H. Noh, S. I. Seok, J. Seo, *Energy Environ. Sci.* **2017**, *10*, 2109.

[54] T. Duong, J. Peng, D. Walter, J. Xiang, H. Shen, D. Chugh, M. Lockrey, D. Zhong, J. Li, K. Weber, T. P. White, K. R. Catchpole, *ACS Energy Lett.* **2018**, *3*, 2441.

[55] K. Choi, J. Lee, H. Il Kim, C. W. Park, G. W. Kim, H. Choi, S. Park, S. A. Park, T. Park, *Energy Environ. Sci.* **2018**, *11*, 3238.

[56] S. W. Tong, J. Balapanuru, D. Fu, K. P. Loh, *ACS Appl. Mater. Interfaces* **2016**, *8*, 29496.

[57] L. Meng, C. Sun, R. Wang, W. Huang, Z. Zhao, P. Sun, T. Huang, J. Xue, J. W. Lee, C. Zhu, Y. Huang, Y. Li, Y. Yang, *J. Am. Chem. Soc.* **2018**, *140*, 17255.

[58] N. Arora, M. I. Dar, A. Hinderhofer, N. Pellet, F. Schreiber, S. M. Zakeeruddin, M. Grätzel, *Science* **2017**, *358*, 768.

[59] S. S. Mali, J. V. Patil, H. Kim, R. Luque, C. K. Hong, *Mater. Today* **2019**, *26*, 8.

[60] J. Cao, H. Yu, S. Zhou, M. Qin, T. K. Lau, X. Lu, N. Zhao, C. P. Wong, *J. Mater. Chem. A* **2017**, *5*, 11071.

[61] X. Zhao, H. S. Kim, J. Y. Seo, N. G. Park, *ACS Appl. Mater. Interfaces* **2017**, *9*, 7148.

[62] A. K. Jena, Y. Numata, M. Ikegami, T. Miyasaka, *J. Mater. Chem. A* **2018**, *6*, 2219.

[63] A. K. Jena, M. Ikegami, T. Miyasaka, *ACS Energy Lett.* **2017**, *2*, 1760.

[64] K. Domanski, J. P. Correa-Baena, N. Mine, M. K. Nazeeruddin, A. Abate, M. Saliba, W. Tress, A. Hagfeldt, M. Grätzel, *ACS Nano* **2016**, *10*, 6306.

[65] M. O. Reese, S. A. Gevorgyan, M. Jørgensen, E. Bundgaard, S. R. Kurtz, D. S. Ginley, D. C. Olson, M. T. Lloyd, P. Morvillo, E. A. Katz, A. Elschner, O. Haillant, T. R. Currier, V. Shrotriya, M. Hermenau, M. Riede, K. R. Kirov, G. Trimmel, T. Rath, O. Inganäs, F. Zhang, M. Andersson, K. Tvingstedt, M. Lira-Cantu, D. Laird, C. McGuiness, S. Gowrisanker, M. Pannone, M. Xiao, J. Hauch, R. Steim, D. M. Delongchamp, R. Rösch, H. Hoppe, N. Espinosa, A. Urbina, G. Yaman-Uzunoglu, J. B. Bonekamp, A. J. J. M. Van Breemen, C. Girotto, E. Voroshazi, F. C. Krebs, *Sol. Energy Mater. Sol. Cells* **2011**, *95*, 1253.

Chapter 2

Stoichiometric effect of precursor solutions on the light induced degradation

G. Tumen-Ulzii, C. Qin, D. Klotz, M. R. Leyden, P. Wang, M. Auffray, T. Fujihara, T. Matsushima, J-W. Lee, S-J. Lee, Y. Yang, and C. Adachi, *Advanced Materials*, **32**, 1905035 (2020).

2.1 Introduction

Among reported perovskite composites, cesium containing triple cation mixed perovskites with the composition of $Cs_{0.05}(FA_{1-x}MA_x)_{0.95}Pb(I_{1-y}Br_y)_3$ is known to have excellent solar power conversion with high reproducibility[1–5] as I mentioned in Chapter 1. Thus, I used this perovskite composition for the PSCs fabrication.

To obtain highly efficient PSCs, an excess amount of PbI_2 is usually used for PSCs fabrication.[3,6–8] On the other hand, there are less studies in literature focusing on the effect of excess PbI_2 on the stability of PSCs.[9–13] Therefore, the clarification of basic degradation mechanisms is needed to further improve the stability of PSCs.

I investigated the influence of excess PbI_2 on the long-term stability and related degradation mechanisms of PSCs in this Chapter. I fabricated PSCs using three kinds of different precursor solutions having different concentrations of PbI_2. I found that unreacted PbI_2 crystals tend to form in films when the PbI_2 concentrations in precursor solutions increase. While the PCEs of all PSCs were similar and were not strongly correlated with the PbI_2 content, the solutions with higher concentrations of PbI_2 produced PSCs with accelerated degradation. This degradation could be related to the decomposition of PbI_2 into metallic lead and iodine under light irradiation.

2.2 Experimental section

Materials. A SnO_2 colloidal precursor solution [tin(IV) oxide, 15% in H_2O colloidal dispersion] was purchased from Alfa Aesar. All precursor materials, such as cesium iodide (CsI), formamidinium iodide (FAI), methylammonium bromide (MABr), PbI_2 and lead bromide ($PbBr_2$) for the perovskite fabrication were purchased from Tokyo

Chemical Industry (TCI). Spiro-OMeTAD was purchased from Merck. The solvents, such as chlorobenzene (CB), DMF, and DMSO, and the dopants for the spiro-OMeTAD such as lithium bis(trifluoromethanesulfonyl)imide (LiTFSI), 4-tert-butylpyridine (4-tBP) and tris(2-(1H-pyrazol-1-yl)-4-*tert*-butylpyridine)-cobalt(III)tri[bis-(trifluoromethane)sulfonimide] (FK-209) were purchased from Sigma-Aldrich. These purchased materials were used as-received without further purification.

Preparation of precursor solutions. A precursor solution of perovskite was prepared by dissolving 1.10 M of FAI, 0.2 M of MABr, 0.2 M of $PbBr_2$ and 1.12 M of PbI_2 in anhydrous DMF/DMSO (4:1 in volume). Additionally, 0.08 M CsI solution in DMSO was added into the aforementioned precursor solution to obtain the desired composition of $Cs_{0.05}(FA_{85}MA_{15})_{0.95}Pb(I_{85}Br_{15})_3$. This solution had a total concentration of cation of 1.38 M and a total concentration of lead halide of 1.32 M. I used two additional precursor solutions with increased molar concentrations of PbI_2 (1.15 M, and 1.18 M). The highest concentration of PbI_2 (1.18 M) provides a solution with stoichiometric balance. Hereafter, perovskite films fabricated from the PbI_2 solutions with the concentrations of 1.12, 1.15, and 1.18 M are called S-1, S-2, and S-3, respectively. The precursor solution was stirred at 70 °C for 3 hours and then filtered with a 0.2 μm polytetrafluoroethylene (PTFE) filter before use. A precursor solution for the HTL fabrication was prepared by dissolving 70 mM of spiro-OMeTAD in CB. This solution was doped with 4-tBP, LiTFSI, and FK-209 at the molar ratio of spiro-OMeTAD : LiTFSI : TBP : FK-209 = 1: 0.5 : 3.3 : 0.03. Pre-prepared stock solutions of LiTFSI (520 mg ml^{-1} in acetonitrile) and FK-209 (300 mg ml^{-1} in acetonitrile) were used.

Device fabrication. Using the aforementioned S-1, S-2 and S-3 solutions, I fabricated PSCs with a device architecture of glass substrate/indium tin oxide (ITO) electrode (100 nm)/SnO_2 ETL (30 nm)/ $Cs_{0.05}(FA_{85}MA_{15})_{0.95}Pb(I_{85}Br_{15})_3$ perovskite light absorber (650 nm)/spiro-OMeTAD HTL (150 nm)/Au electrode (80 nm). Glass substrates coated with a pre-patterned ITO layer with a thickness of 100 nm (Atsugi Micro, Japan) and a sheet resistance of 10 Ω $sq.^{-1}$ were cleaned sequentially by ultrasonication in detergent, pure water, acetone, and isopropanol for 10 min each and then subjected to UV-ozone treatment for 15 min. Next a SnO_2 film was deposited on the ITO surface by spin-coating at 3,000 rpm for 30 sec using an aqueous SnO_2 colloidal solution, which was diluted to 2.67% in water. This SnO_2 film was annealed at 150 °C for 30 min, and treated with UV-ozone for 15 min. The perovskite layer was prepared from the precursor solution. A perovskite film was spin-coated at 1,000 rpm for 10 sec and then at 6,000 rpm for 30 sec. Ten seconds before the end of the substrate rotation, 120 μl of CB was dropped onto the spinning substrate. Subsequently, the perovskite layer was annealed at 100 °C for 45 min. The preparation of the perovskite and spiro-OMeTAD films was done in a nitrogen-filled glove box while the SnO_2 films were fabricated in air. Finally, an 80–100-nm-thick Au electrode was thermally deposited in vacuum to complete the devices. The deposition rate was 0.1 nm s^{-1} and the base pressure was 10^{-4} Pa for the Au deposition. The fabricated PSCs were encapsulated using a glass lid and UV-cured sealant without exposure to air.

PSC characterization. $J-V$ curve measurements were performed on the PSCs using a computer-controlled Keithley 2400 source unit under the simulated AM1.5G solar illumination from a Xe lamp-based solar simulator (SRO-25 GD, Bunko-Keiki, Japan) with a scan rate of 200 mV s^{-1}. While the original PSCs' area defined by the overlap of the ITO and Au electrodes was 4 mm^2, the illumination area during the $J-V$ measurements was defined at 3.24 mm^2 (1.8 × 1.8 mm^2) using a black shadow mask. The lamp power was carefully calibrated at 100 mW cm^{-2} (1 sun) using a crystalline Si reference cell with an amorphous Si optical filter (Bunko-Keiki), which was certificated by the National Institute of Advanced Industrial Science and Technology of Japan.

PSC lifetime measurements. Light from a white light-emitting diode array with an intensity of 100 mW cm^{-2} was continuously illuminated on the encapsulated PSCs in ambient air at room temperature (~25 °C). The evolution of V_{OC}, J_{SC}, FF and PCE was automatically measured using a lifetime measurement system (System Engineers). In between scans, the PSCs were connected with a 1 kΩ resistor to operate the PSC near the MPP.

SEM measurements. SEM and high-resolution SEM (HR-SEM) images of the perovskite films were taken with a JEOL JCM-5700 and a HITACHI SU8000 system at an acceleration voltage of 5 kV and 1 kV with magnifications of ×10,000 and ×40,000, respectively. Quantitative elemental analysis was performed on the samples with a HITACHI SU8000 SEM-Energy Dispersive Spectroscopy (EDS) system equipped with an energy dispersive X-ray analyzer.

XRD measurements. XRD patterns of the perovskite films were evaluated with an XRD system using a typical 2 θ/θ technique [λ = 1.54 Å (CuKα)] (Rigaku, Ultima IV).

Steady-state photoluminescence (PL) measurements. PL spectra of perovskite films were measured using a JASCO FP-8600 spectrofluorometer. The excitation wavelength used here was 460 nm. The excitation light was irradiated from the glass substrate side.

X-ray photoelectron spectroscopy (XPS) measurements. XPS (PHI5000-VersaProbeII, monochromated Al Kα = 1486.6 eV) was used. The binding energies were calibrated using the Au-4f$^{7/2}$ peak (84.0 eV) measured from a vacuum-deposited Au sample.

2.3 Results and Discussion

Figure 2-1 shows SEM images and XRD patterns of S-1, S-2 and S-3 perovskite films fabricated with different PbI_2 concentrations. SEM images of perovskite films in **Fig. 2-1**(a-c) show the dense and uniform morphologies. But, some of abnormal grains (white grains) were observed on S-3 films (**Fig. 2-1**c). In literature, similar grains were observed, which was assigned to unreacted or excess PbI_2.[14] From the XRD patterns of perovskite films in **Fig. 2-1**(d-f), an additional peak at 12.5° was observed only in S-3 films (**Fig. 2-1**f), which was assigned to the (0 0 *l*) plane of PbI_2 crystals.[6,14–16] All the other peaks originated from the cubic perovskite structure in **Fig. 2-1**(d–f), which is consistent with the previous literature.[1] This would suggest that the white grains in **Fig. 2-1**c are PbI_2 crystals, although the precursor solution (S-3) provides the stoichiometric balance of organic cations and lead halides as mentioned in experimental section. The formation of PbI_2 crystals in films could have different reasons such as saturated dissolution of PbI_2 in precursor solution, or some part of organic salt is washed away by anti-solvent dripping process of CB during the spin-coating of films.

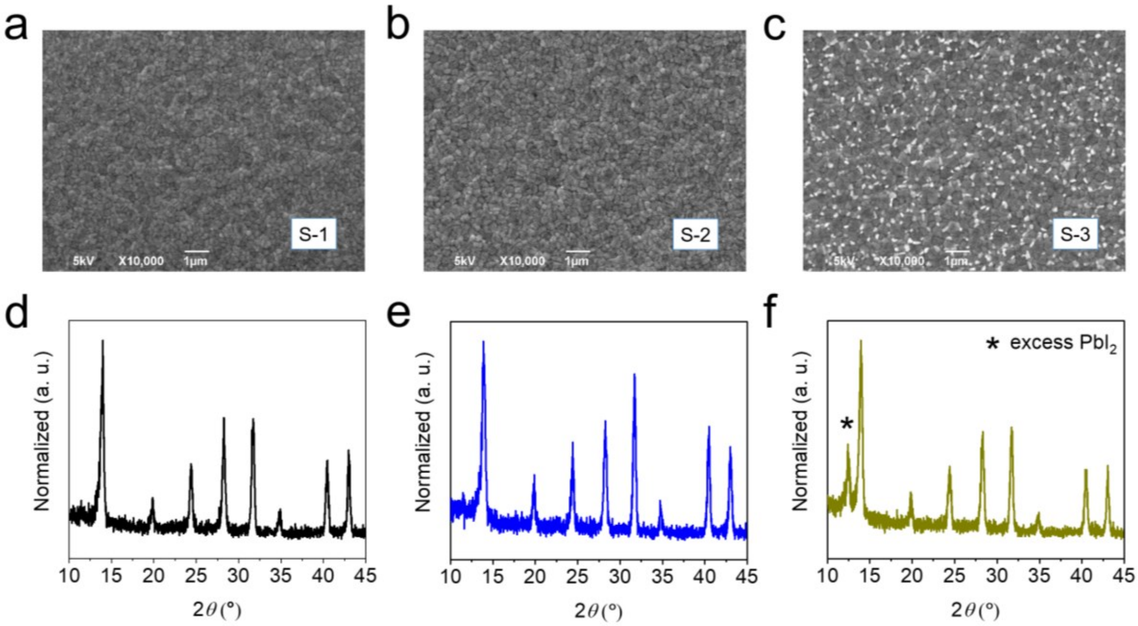

Figure 2-1. Top-surface SEM images and XRD patterns of a, d) S-1, b, e) S-2, and c, f) S-3 perovskite films.

Using the aforementioned S-1, S-2 and S-3 solutions, I fabricated PSCs with a device architecture shown in **Fig. 2-2**a. (Note that I used this device architecture through the studies in this thesis.) *J-V* characteristics of representative PSCs with S-1, S-2, or S-3 films are shown in **Fig. 2-2**b, and solar cell parameters estimated from this figure are summarized in **Table 2-1**. The S-1, S-2 and S-3 devices exhibited PCEs of 18.0, 19.0 and 18.4%, respectively. PCEs' statistics is shown in **Fig. 2-2**c with the average PCEs being 17.3, 17.6 and 16.9% for S-1, S-2 and S-3 devices, respectively. Although the S-2 devices had the slightly higher PCEs, the differences in PCE among the S-1, S-2, or S-3 devices were less than 1%, meaning that the PbI_2 concentrations in the precursor solutions had little influence on the initial PCEs.

Next, I studied the stability of S-1, S-2 and S-3 PSCs under continuous illumination from a white LED with a light intensity of 100 mW cm^{-2}. **Figure 2-2**d shows the PCE evolution of S-1, S-2 and S-3 PSCs. The S-1 and S-2 PSCs retained 92% and 99% of their initial PCEs after 520 h of continuous illumination, respectively. On the contrary, the PCEs of the S-3 PSCs decreased to 47% of its initial value. I believe that the observed quick degradation of the S-3 PSCs was caused by the presence of PbI_2 crystals in the perovskite films, which was confirmed in **Fig. 2-1**.

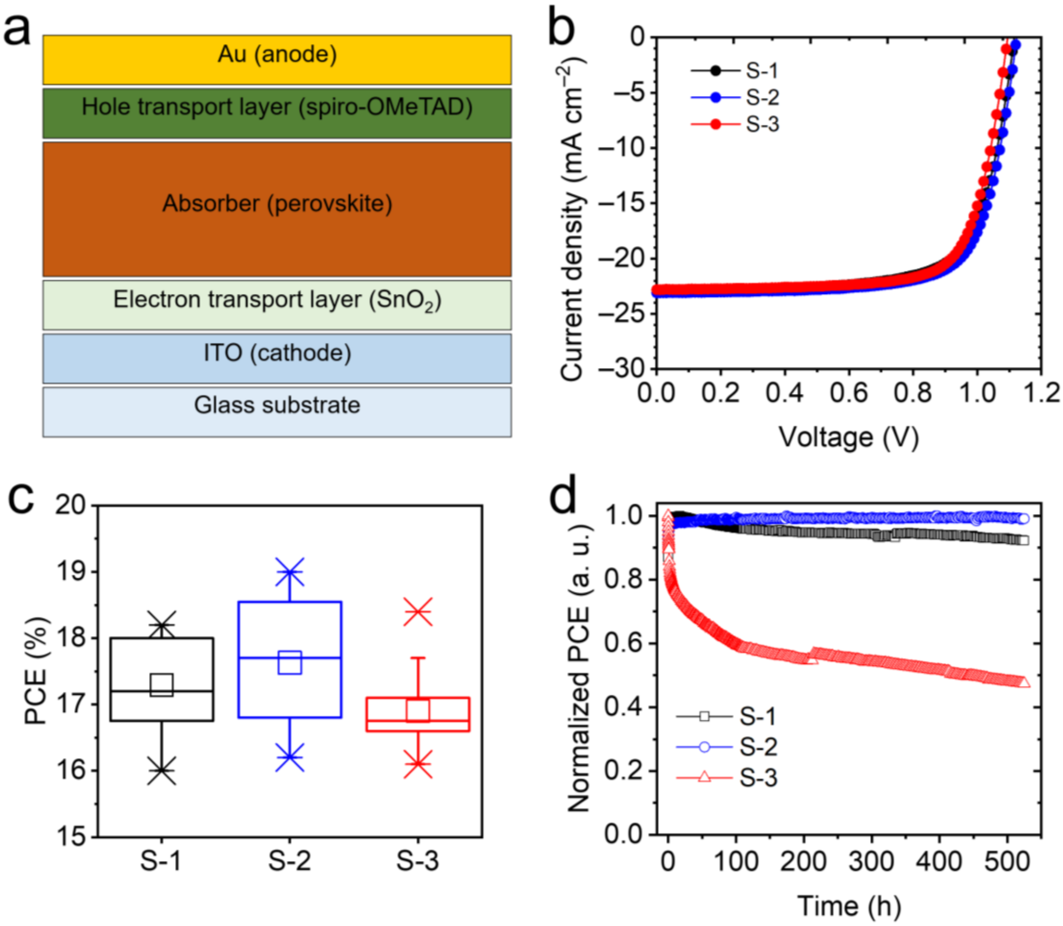

Figure 2-2. Device architecture (a), *J–V* curves (b), PCEs' statistics (c) and PCEs' evolution (d) of PSCs.

Table 2-1. Summary of device parameters extracted from Fig. 2-2b.

Sample	J_{sc} (mA cm^{-2})	V_{oc} (V)	FF	PCE (%)
S-1	22.87	1.12	0.71	17.97
S-2	23.10	1.12	0.73	19.01
S-3	22.81	1.09	0.74	18.44

Although I achieved stable PSCs with the S-1 and S-2 compositions, it is crucial to find the origin of the degradation of S-3 PSCs with excess PbI_2. To investigate the degradation of S-3 PSCs, I performed morphological characterizations on S-3 films after carefully removing the Au electrode and the spiro-OMeTAD HTL from devices as illustrated in **Fig. 2-3**a. In detail, i) scotch tape was attached on top of the Au electrode; ii) the Au electrode was removed by peeling off scotch tape; iii) 1 ml of CB was dropped on the substrate, followed by the substrate rotation at 2000 rpm for 60 sec. During the substrate rotation, 3 ml of CB was continuously dropped onto the substrate to remove the spiro-OMeTAD layer completely.

First, a HR-SEM measurement was used to check the morphology of an un-illuminated and degraded perovskite film used in PSCs. The morphology of the S-3 film significantly changed after degradation as shown in **Fig. 2-3**b and c. The S-3 perovskite films without pinholes and defects were observed in unilluminated samples (**Fig. 2-3**b). This points that the process of removing the HTL and the Au electrode had negligible damage to the perovskite film. Also, the PbI_2 crystals are present in the unilluminated perovskite films. However, in the degraded film, the PbI_2 crystals almost disappeared, and defects and pinholes became more frequent (**Fig. 2-3**c). The disappearance of PbI_2 in S-3 films was supported by XRD patterns. The peak intensity at 12.5°, which originates from PbI_2, significantly decreased in a degraded film compared with that of an un-illuminated film (**Fig. 2-3**d). On the contrary, the morphology of the degraded S-1 and S-2 films exhibited a negligible change, as shown in **Fig. 2-3**e.

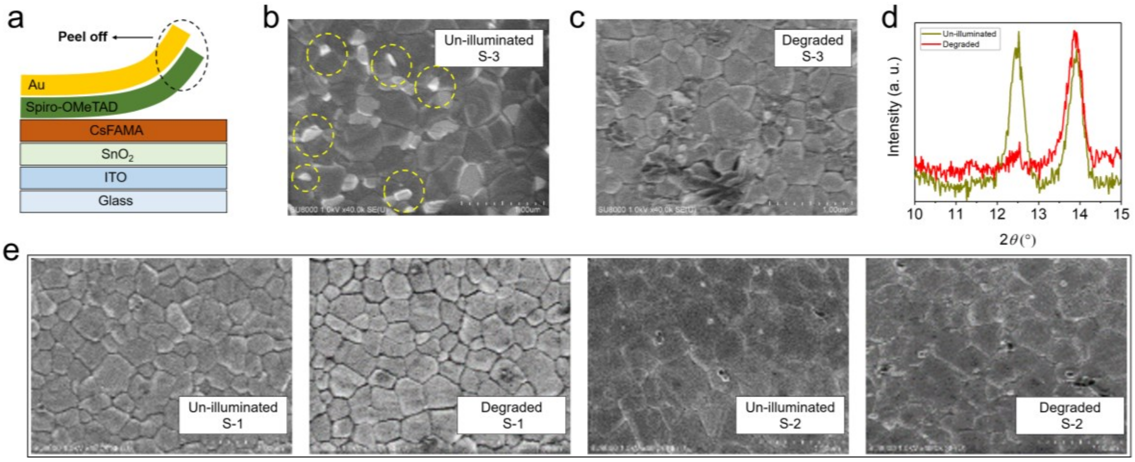

Figure 2-3. a) Illustration showing the removal of the Au electrode and the spiro-OMeTAD layer. b,c) Top-surface HR-SEM images of b) un-illuminated and c) degraded S-3 films. d) XRD patterns of un-illuminated and degraded S-3 films. e) Top-surface HR-SEM images of un-illuminated and degraded S-1 and S-2 films.

The disappearance of PbI_2 crystals in S-3 perovskite films could be related to photo-decomposition of PbI_2. In fact, the photo-decomposition of PbI_2 has been reported by a number of researchers, who showed that PbI_2 decomposes into metallic lead when illumination energy is above the bandgap of PbI_2 at elevated temperature[9,17,18]. Recently, Prof. Qi group confirmed photo-decomposition of PbI_2 thin films[19] by detecting the production of Pb^0 and I_2 gas under light illumination of 0.55 sun. Mono and di-iodine gas was detected by mass spectrometry. Newly formed Pb^0 in films was confirmed by the emergence of an XRD peak at ~31°, which was assigned to cubic Pb^0. Additionally, XPS was used to further confirm Pb^0, peaks of which were observed at 137.0 and 141.9 eV.[19] Therefore, I conducted XPS measurements on degraded and un-illuminated S-3 films. There was almost no difference between the two XPS spectra (**Fig. 2-4**a), indicating no formation of metallic Pb at the film surfaces. Further, I conducted XRD measurements on the degraded and un-illuminated S-3 films to observe the Pb^0 component on the surface or bulk of perovskite films but did not observe any XRD peak coming from Pb^0 as shown in **Fig.**

2-4b. I supposed that Pb^0 is mainly formed near the SnO_2/perovskite interface of the opposite side, as I will discuss next.

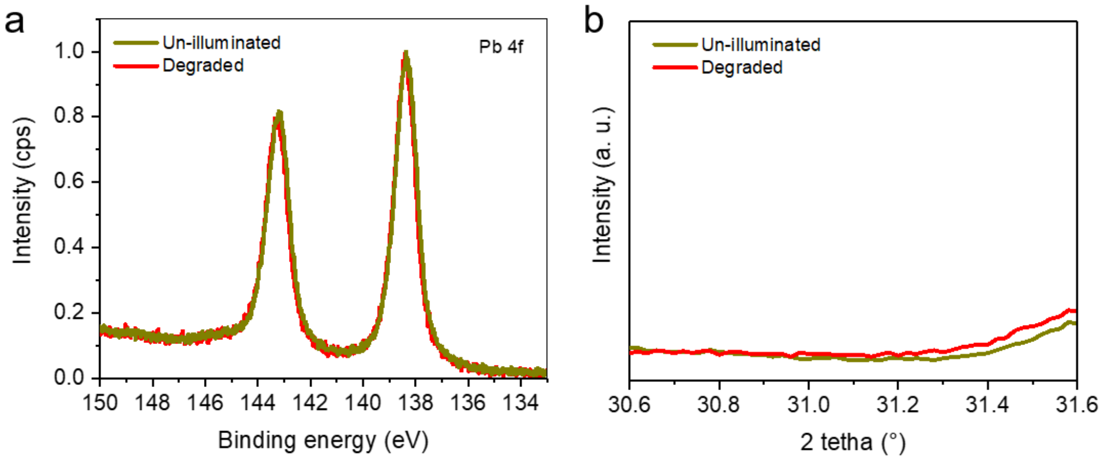

Figure 2-4. a) XPS results (Pb 4f core levels) and b) XRD patterns of un-illuminated and degraded S-3 perovskite films after removing the HTL and the Au electrode.

I observed a grey colored film formed on the bottom of the degraded S-3 devices although there was no grey colored film in the degraded S-1 and S-2 PSCs (**Figures 2-5** and **2-6**). Additionally, the grey colored film was only formed in the light-exposed area of the S-3 devices. These results indicate that the color change might stem from the decomposition of PbI_2 crystals in the perovskite films of the S-3 device and is related to the device degradation.

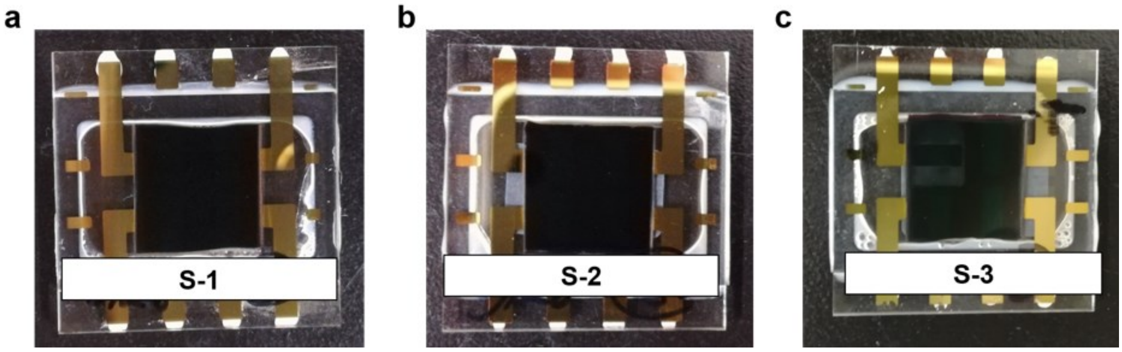

Figure 2-5. Photographs of a) S-1, b) S-2, and c) S-3 PSCs after 520 h of continuous light illumination. These photographs were taken from the substrate side.

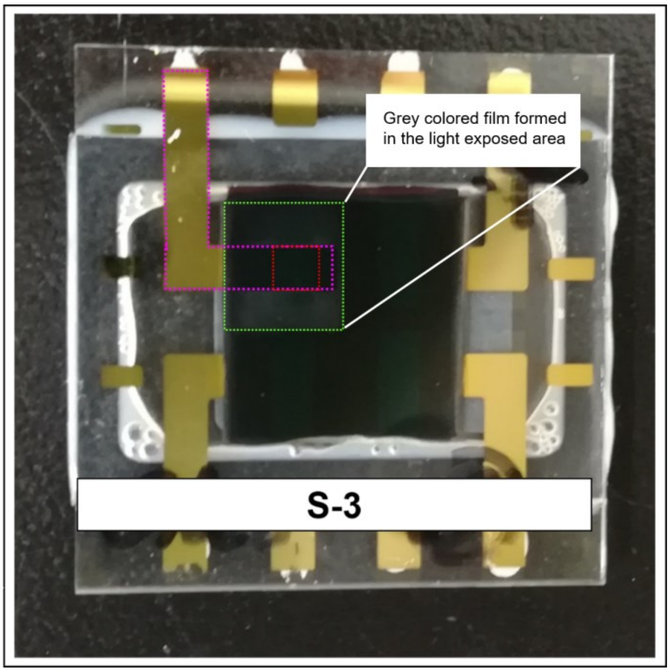

Figure 2-6. Photograph of the S-3 PSC degraded after 520 h of illumination. This photograph was taken from the substrate side. The green and pink dashed lines indicate the region exposed to light and the region coated by the gold electrode, respectively. The red dashed line indicates the active area of the device. A grey colored film appeared in the light exposed area only, but no grey color appeared under the gold electrode because of the encapsulation effect with the gold electrode.

To confirm the photolysis of unreacted PbI_2, I measured XRD patterns of SnO_2 of un-illuminated and degraded PSCs after removing the perovskite, spiro-OMeTAD, and Au layers. XRD patterns of the SnO_2 films are shown in **Fig. 2-7**a and b. The XRD peaks coming from polycrystalline SnO_2 were seen in both un-illuminated and degraded S-3 samples, which is consistent with literature[15]. A new peak at ~31° appeared in degraded S-3 samples (see enlarged figure in **Fig. 2-7**c), which was assigned to metallic Pb.

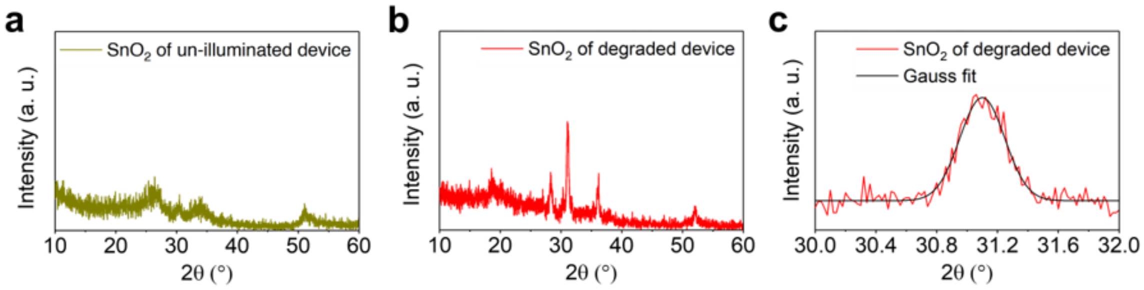

Figure 2-7. XRD patterns measured at the surface of SnO_2 films, which were prepared from un-illuminated (a) and degraded S-3 PSCs (b). (c) is the magnified XRD peak from (b).

Furthermore, SEM-EDS was performed on the degraded and un-illuminated SnO_2 samples to confirm a change in Pb content. The atomic percentage of Pb was 1.28% in the degraded sample, which was about two-fold higher than that in the un-illuminated sample (0.54%) (see **Table 2-2**).

Table 2-2. Atomic percentages of Pb and I, which were measured from un-illuminated and degraded S-3 samples using SEM-EDS. "Others" in this table means the sum of percentages of atoms other than Pb and I.

Atom	**Atomic percentage (%)**	
	Un-illuminated sample	**Degraded sample**
Pb (M-shell)	0.54	1.28
I (L-shell)	0.50	0.52
Others	98.96	98.20

The increased percentage of Pb likely originated from the decomposition of PbI_2 crystals. Therefore, these results support the photolysis of PbI_2 crystals in perovskite films happening according to **eq. 2-1**.

$$PbI_2 \rightarrow Pb(s) + I_2(g) \tag{2-1}$$

Metallic Pb formed at the SnO_2/perovskite interface would act as carrier recombination centers as illustrated in **Fig. 2-8**a, which is one of the reasons of the observed degradation of S-3 PSCs. This is supported by decreased steady-state PL intensities in degraded perovskite films because of exciton quenching by Pb (**Fig. 2-8**b).

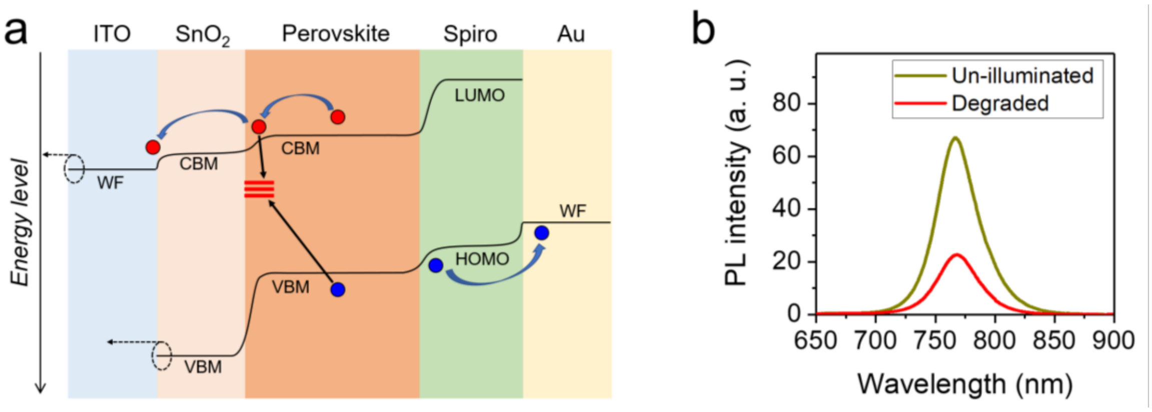

Figure 2-8. a) Energy level diagram of PSCs and b) steady-state PL spectra of S-3 samples (ITO/SnO_2/perovskite) before and after degradation.

2.4 Conclusions

In summary, I revealed that, although the excess PbI_2 does not significantly impact the initial performance of PSCs, the long-term stability of PSCs under light illumination is very sensitive to the presence of PbI_2 crystals in perovskite films. By controlling the excess PbI_2, it is possible to improve the stability of PSCs under illumination. While the PCEs of PSCs, in which excess PbI_2 crystals were not present, retained 99% of the initial value after 520 h of continuous illumination, the PCE of PSC with excess PbI_2 crystals reduced to 47% of the initial value. The degradation of PSCs was related to the photo-decomposition of excess PbI_2 crystals into metallic Pb and I_2 under light illumination. Interestingly, the formed metallic Pb was detected only at the interface of the SnO_2 layer and the perovskite layer after the degradation of PSCs. Metallic Pb thus generated at the SnO_2/perovskite interface acted as a quencher for carriers, which gradually made the PCEs lower.

This result suggests that reducing the existence of PbI_2 crystals in resulting perovskite films by preparing a precursor solution with an appropriate composition for spin-coating is crucial to fabricating stable PSCs. In addition, more detailed study is needed to understand why metallic Pb forms only at the SnO_2/perovskite interface for limiting the PSC degradation associated with detrimental Pb.

References

[1] M. Saliba, T. Matsui, J. Y. Seo, K. Domanski, J. P. Correa-Baena, M. K. Nazeeruddin, S. M. Zakeeruddin, W. Tress, A. Abate, A. Hagfeldt, M. Grätzel, *Energy Environ. Sci.* **2016**, *9*, 1989.

[2] M. Deepa, M. Salado, L. Calio, S. Kazim, *Phys. Chem. Chem. Phys.* **2017**, *19*, 4069.

[3] Y. Hu, E. M. Hutter, P. Rieder, I. Grill, J. Hanisch, M. F. Aygüler, A. G. Hufnagel, M. Handloser, T. Bein, A. Hartschuh, K. Tvingstedt, V. Dyakonov, A. Baumann, T. J. Savenije, M. L. Petrus, P. Docampo, *Adv. Energy Mater.* **2018**, *8*, 1703057.

[4] J. Y. Seo, H. S. Kim, S. Akin, M. Stojanovic, E. Simon, M. Fleischer, A. Hagfeldt, S. M. Zakeeruddin, M. Grätzel, *Energy Environ. Sci.* **2018**, *11*, 2985.

[5] T. Bu, J. Li, F. Zheng, W. Chen, X. Wen, Z. Ku, Y. Peng, J. Zhong, Y.-B. Cheng, F. Huang, *Nat. Commun.* **2018**, *9*, 4609.

[6] M. Abdi-Jalebi, Z. Andaji-Garmaroudi, S. Cacovich, C. Stavrakas, B. Philippe, J. M. Richter, M. Alsari, E. P. Booker, E. M. Hutter, A. J. Pearson, S. Lilliu, T. J. Savenije, H. Rensmo, G. Divitini, C. Ducati, R. H. Friend, S. D. Stranks, *Nature* **2018**, *555*, 497.

[7] T. Bu, X. Liu, Y. Zhou, J. Yi, X. Huang, L. Luo, J. Xiao, Z. Ku, Y. Peng, F. Huang, Y. B. Cheng, J. Zhong, *Energy Environ. Sci.* **2017**, *10*, 2509.

[8] Y. Zhang, J. S. Yun, Y. Zeng, J. Huang, X. Liu, Z. Liu, X. Hao, A. Pu, J. A. Stride, J. Seidel, L. Shi, M. A. Green, K. Sun, Z. Hameiri, *Adv. Energy Mater.* **2018**, *8*, 1800138.

[9] R. I. Dawood A. J. Forty, M. R. Tubbs, *Proc. R. Soc. A. Math. Phys. Sci.* **1965**, *284*, 272.

[10] J. Schoonman, *Chem. Phys. Lett.* **2015**, *619*, 193.

[11] T. P. Gujar, T. Unger, A. Schönleber, M. Fried, F. Panzer, S. Van Smaalen, A. Köhler, M. Thelakkat, *Phys. Chem. Chem. Phys.* **2017**, *20*, 605.

[12] A. S. Yerramilli, Y. Chen, D. Sanni, J. Asare, N. D. Theodore, T. L. Alford, *Org. Electron.* 2018, 59, 107.

[13] F. Liu, Q. Dong, M. K. Wong, A. B. Djurišić, A. Ng, Z. Ren, Q. Shen, C. Surya, W. K. Chan, J. Wang, A. M. C. Ng, C. Liao, H. Li, K. Shih, C. Wei, H. Su, J. Dai, *Adv. Energy Mater.* **2016**, *6*, 1502206.

[14] Q. Jiang, Z. Chu, P. Wang, X. Yang, H. Liu, Y. Wang, Z. Yin, J. Wu, X. Zhang, J. You, *Adv. Mater.* **2017**, *29*, 1703852.

[15] Q. Jiang, L. Zhang, H. Wang, X. Yang, J. Meng, H. Liu, Z. Yin, J. Wu, X. Zhang, J. You, *Nat. Energy* **2017**, *2*, 16177.

[16] B. Shi, X. Yao, F. Hou, S. Guo, Y. Li, C. Wei, Y. Ding, Y. Li, Y. Zhao, X. Zhang, *J. Phys. Chem. C* **2018**, *122*, 21269.

[17] J. F. Verwey, *J. Phys. Chem. Solids* **1970**, *31*, 163.

[18] M. G. Albrecht, M. Green, *J. Phys. Chem. Solids* **1977**, *38*, 297.

[19] E. J. Juarez-Perez, L. K. Ono, M. Maeda, Y. Jiang, Z. Hawash, Y. Qi, *J. Mater. Chem. A* **2018**, *6*, 9604.

Chapter 3

Study on ion migration induced degradation

G. Tumen-Ulzii, T. Matsushima, D. Klotz, M. R. Leyden, P. Wang, C. Qin, J-W. Lee, S-J. Lee, Y. Yang, and C. Adachi, *Communications Materials,* **1***,* 31 (2020). https://doi.org/10.1038/s43246-020-0028-z

3.1 Introduction

Although the highly efficient PSCs have been obtained, with over 20% of PCE,[1] these reported PCE values are questionable because of the presence of *J*–*V* hysteresis when measure in the consecutive forward and reverse scans.[2] One of the potential origins of *J*–*V* hysteresis is ion migration through PSCs.[3–6] Furthermore, ion migration would induce the degradation of PSCs.[7] Therefore, it is necessary to clarify the relation between ion migration and *J*–*V* hysteresis to obtain hysteresis-free, stable PSCs.

It was reported that positive ions move to the interface between the perovskite layer and the ETL and that negative ions move to the opposite interface between the perovskite layer and the HTL by applying forward bias.[8,9] During this abnormal movement of ions, researchers conducted the transient photocurrent measurement and observed the inverted photocurrent, which means that electrons are extracted via the anode electrode.[9] This effect directly explains the movement direction of the abnormal ions. In light of the ions movement, a number of researchers reported the relationship between ion migration and *J*–*V* hysteresis in PSCs.[10-12]

Weber et al. recently reported that the localization of positively charged ions at the interface between the perovskite layer and the ETL causes the *J*–*V* hysteresis in PSCs.[12] The localized positive ions accelerate non-radiative recombination, leading to the quick degradation of PSCs as well.[12–14] However, the reason of such ionic localization at the ETL interface is still unclear. Therefore, it is also necessary to clarify mechanisms of the ion migration in detail.

In this chapter, I studied the effect of ion localization at the interface between a perovskite and an ETL, and its effect on the long-term stability of PSCs. I found that the presence of hydroxyl groups (–OH) at a metal oxide ETL like SnO_2 is one possible origin of this ionic localization. To avoid the localization of the positive ions, I deactivated the hydroxyl groups by chemically modifying the SnO_2 surface with a self-assembled monolayer (SAM) of a fullerene derivative. Introducing this interfacial SAM significantly reduced the *J–V* hysteresis. With this SAM treatment, I obtained almost no degradation of PSCs at room temperature under continuous illumination for 1,000 hours.

3.2 Results and discussion

Perovskite films and PSCs with the composition of $Cs_{0.05}(FA_{85}MA_{15})_{0.95}Pb(I_{85}Br_{15})_3$ were prepared from the S-3 solution. I note that the detailed experimental procedures of the device fabrication and characterization are the same as those described in the experimental section of chapter 2.

To identify the existence of the ion migration, temperature-dependent electrical conductivity measurements were carried out by measuring current–voltage (*I–V*) curves of perovskite films in a lateral-electrode architecture. This lateral device architecture is illustrated in **Fig. 3-1**a. The distance between two Au electrodes is 100 μm. This measurement was designed to highlight ionic conduction, as ions would not contribute to the conductivity at low temperatures but would contribute when the temperature was sufficiently high to provide the energy required to form mobile ions.[15]

Figure 3-1b shows *I–V* curves and revealed that the hysteresis increased with increasing temperature. I speculated that the observed *I–V* hysteresis at higher temperatures is probably related to the migration of ionic species. The possible ions are

I^-, Br^-, MA^+, FA^+, Cs^+ and Pb^{2+}. Although the most probable mobile ions with low activation energy (E_a) in the perovskite films are I^- and MA^+ as reported in literature,[16] it is challenging to determine the distinct ionic effect on the observed hysteresis. Nevertheless, the *I*–*V* hysteresis observed here indicates the existence of the ion migration in our perovskite films and is consistent with the previous reports.[17–20]

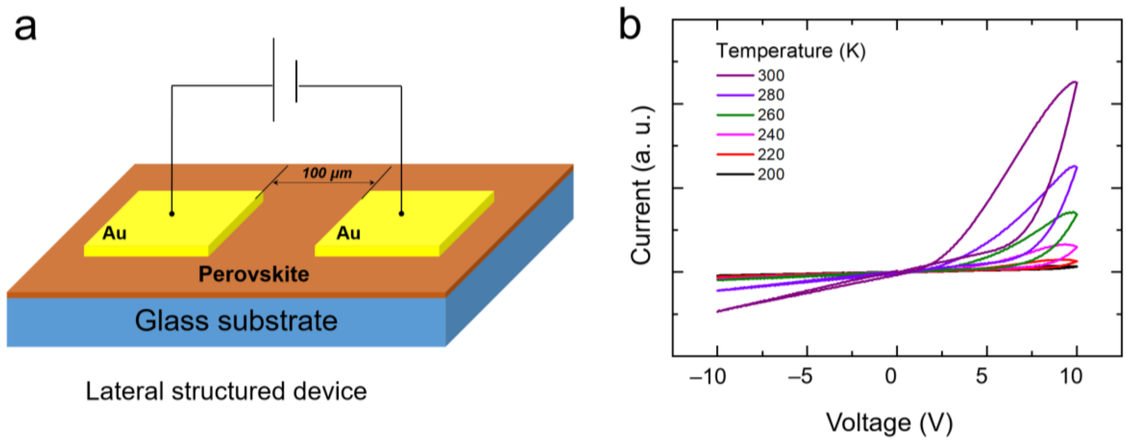

Figure 3-1. a) Lateral device architecture and b) temperature dependent *I*-*V* curves. The thicknesses of the perovskite and Au layers are ~650 and ~100 nm, respectively.

Next, I fabricated S-3 PSCs and measured their *J*-*V* curves at a scan rate of 200 mV s^{-1} (**Table 3-1**). Here I defined that the voltage scan from −0.1 V to 1.2 V is the forward scan and the voltage scan from 1.2 V to −0.1 V is the reverse scan. In this study, I carried out the consecutive forward-to-reverse scans for the PSC evaluation unless otherwise mentioned. Eight devices fabricated in the same batch had the average PCEs of 17.4% and 17.7% in the forward and reverse scans, respectively (**Table 3-1**).

Table 3-1. J_{sc}, V_{oc}, FF, and PCE, and HI values of PSCs. These parameters were extracted from *J*–*V* curves measured at a scan rate of 200 mV s^{-1}.

	Scan direction	***Jsc* (mA cm^{-2})**	***Voc* (V)**	**FF**	**PCE (%)**	**HI**
Average (8 devices)	Forward	−22.04	1.10	0.72	17.37	0.02
	Reverse	−21.92	1.10	0.73	17.70	

The hysteresis Index (HI) defined according to **eq. 3-1** was close to zero (see **Table 3-1**), suggesting that the *J-V* hysteresis is negligible at this scan rate

$$\mathrm{HI} = \frac{\mathrm{PCE}_{\mathrm{reverse}} - \mathrm{PCE}_{\mathrm{forward}}}{\mathrm{PCE}_{\mathrm{reverse}}} \tag{3-1}$$

where $\mathrm{PCE}_{\mathrm{reverse}}$ and $\mathrm{PCE}_{\mathrm{forward}}$ are the PCE values measured in the forward and reverse scans, respectively.

However, the hysteresis increased with decreasing the scan rates from 200 to 10 mV s^{-1} (**Fig. 3-2**).

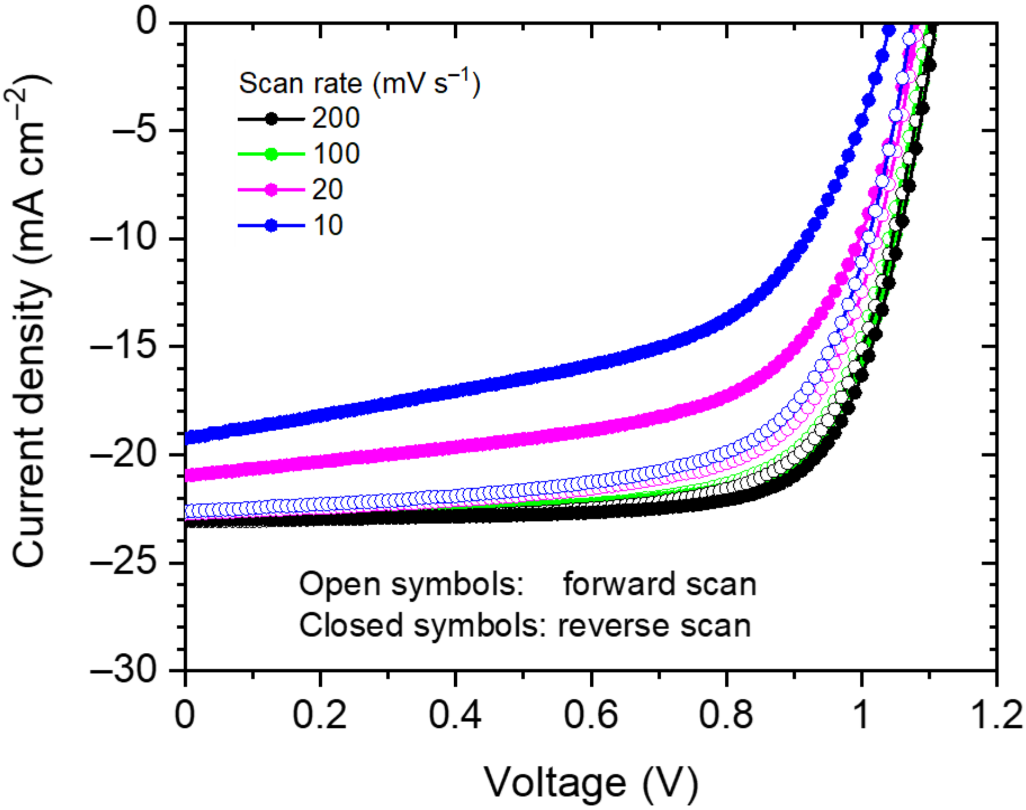

Figure 3-2. Scan-rate-dependent *J–V* curves of PSCs.

The negative HI values obtained at the lower scan rates mean "inverted hysteresis", for which the PCE is higher in the forward scan than that in the reverse scan (**Table 3-2**).

Table 3-2. Scan-rate-dependent J_{sc}, V_{oc}, FF, PCE, and HI values of PSCs. These parameters were extracted from *J–V* curves shown in **Fig. 3-2**.

Scan rate ($mV\ s^{-1}$)	Scan direction	*J*sc ($mA\ cm^{-2}$)	*V*oc (V)	FF	PCE (%)	HI
200	Forward	−23.07	1.10	0.71	18.14	0.04
	Reverse	−23.01	1.11	0.74	18.88	
100	Forward	−22.99	1.10	0.71	17.89	0.02
	Reverse	−22.82	1.10	0.73	18.29	
20	Forward	−22.73	1.08	0.68	16.79	−0.20
	Reverse	−20.96	1.08	0.57	13.97	
10	Forward	−22.63	1.07	0.67	16.25	−0.48
	Reverse	−19.25	1.04	0.45	10.98	

It has been reported that one of the relevant origins of the inverted hysteresis is the ion migration in PSCs.[3,11,21] The migration of different ionic species in perovskite films could cause the *J–V* hysteresis, the degree of which depends on the voltage scan rates,[3] directions (forward-to-reverse or reverse-to-forward bias scans),[22] ranges[21,23] and temperature.[24] Thus, I measured *J–V* curves in the consecutive reverse-to-forward scans (**Fig. 3-3**a), which are opposite to the forward-to-reverse scans I used earlier. The scan rate was 10 mV s^{-1}. In this case, the reverse scan is better than the forward scan in terms of the PCE. For comparison, I again measured *J–V* curves in the consecutive forward-to-reverse scans (**Fig. 3-3**b). The results in these figures tell us that the scan directions are not so important that the first scan provides the higher PCE and repeating the scans decreased the PCEs.

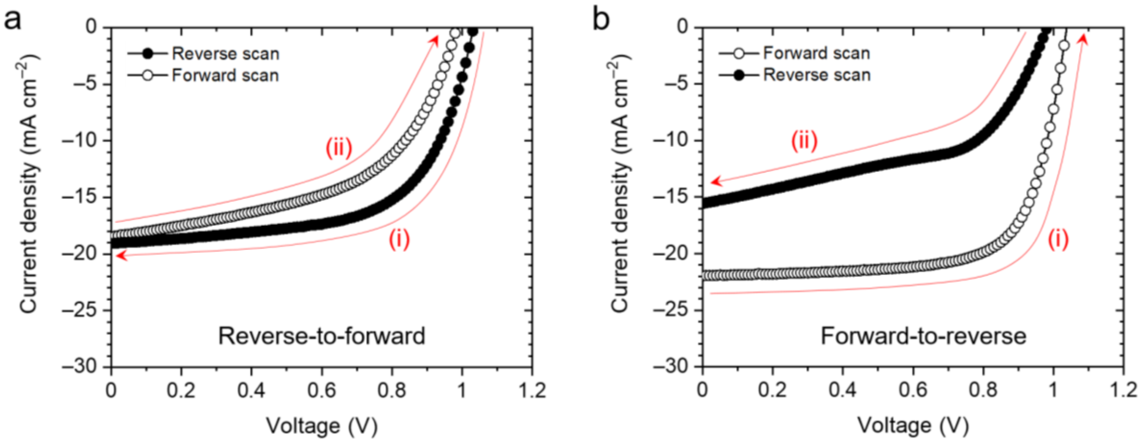

Figure 3-3. *J–V* curves of PSCs measured with a) reverse-to-forward and b) forward-to-reverse scans at a scan rate of 10 mV s^{-1}. Red lines indicate the scanning directions. The measurement temperature was room temperature.

Next, I measured *J–V* curves in a wider scan range between −0.1 V to 2.0 V at a scan rate of 200 mV s^{-1} (**Fig. 3-4**). The hysteresis began to appear with this scan range although the hysteresis was not clearly observed when I used the small scan range from −0.1 V to 1.2 V (**Fig. 3-2**). This may mean that applying a high voltage to PSCs caused more serious hysteresis.

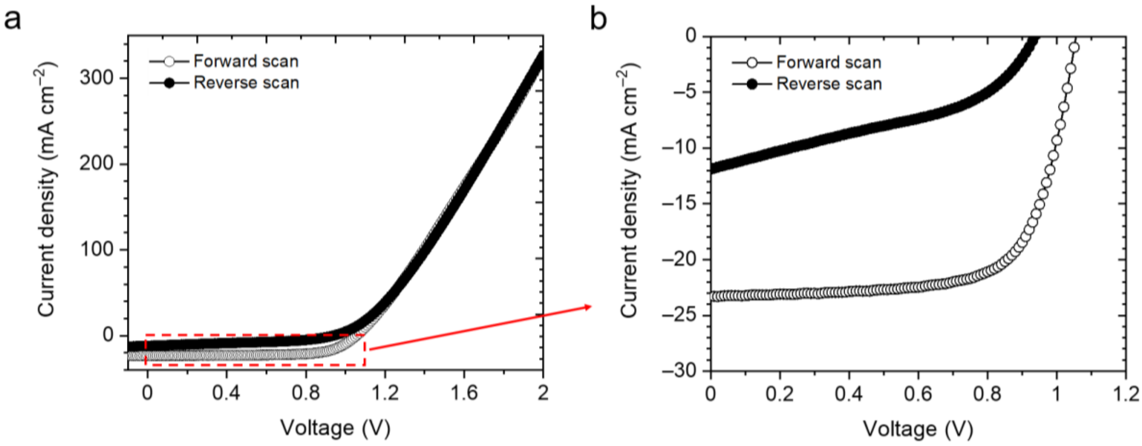

Figure 3-4. a) *J–V* curves of PSCs measured with forward-to-reverse scans in a scan range between −0.1 V to 2.0 V. b) is the enlarged *J–V* curves. The scan rate was 200 mV s^{-1} and the measurement temperature was room temperature.

For a better understanding on the hysteresis, I measured *J–V* curves at a high temperature of 60 °C at a scan rate of 200 mV s^{-1}, resulting in the larger *J–V* hysteresis (**Fig. 3-5**a). The hysteresis again decreased after cooling the PSCs to room temperature

(**Fig. 3-5**b). Considering the aforementioned experimental results, the ion migration is likely in our PSCs, which induces the *J–V* hysteresis.

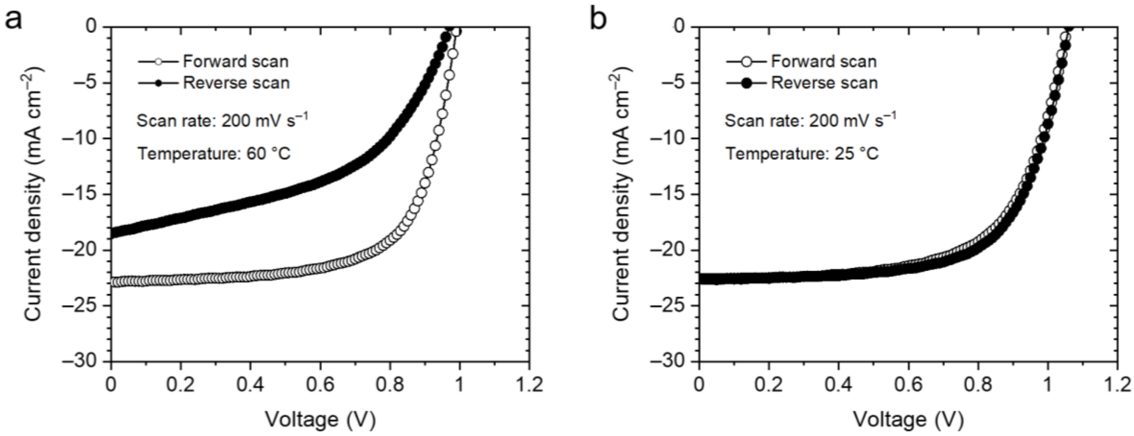

Figure 3-5. *J–V* curves of PSCs measured at a high temperature of 60 °C a) or after the device temperature returning to room temperature. The scan rate is 200 mV s^{-1}.

I speculated that the –OH groups attract the positive ions existing near the SnO_2 surface in our PSCs although most of the positive ions move to the opposite spiro-OMeTAD side along the internal built-in field. The –OH groups were previously identified from the SnO_2 surface.[25,26] To observe the –OH groups in our samples, I characterized the SnO_2 surface with XPS. The Sn 3d core level peak was detected (**Fig. 3-6**a). By analyzing the O 1s core level region (**Fig. 3-6**b), an XPS peak originating from the –OH groups was identified at 531.7 eV near a main oxygen peak at 530.2 eV. This is proof of the presence of the –OH groups on the SnO_2 surface according to the literature,[27–29], which is expected to induce the localization of the positive ions.

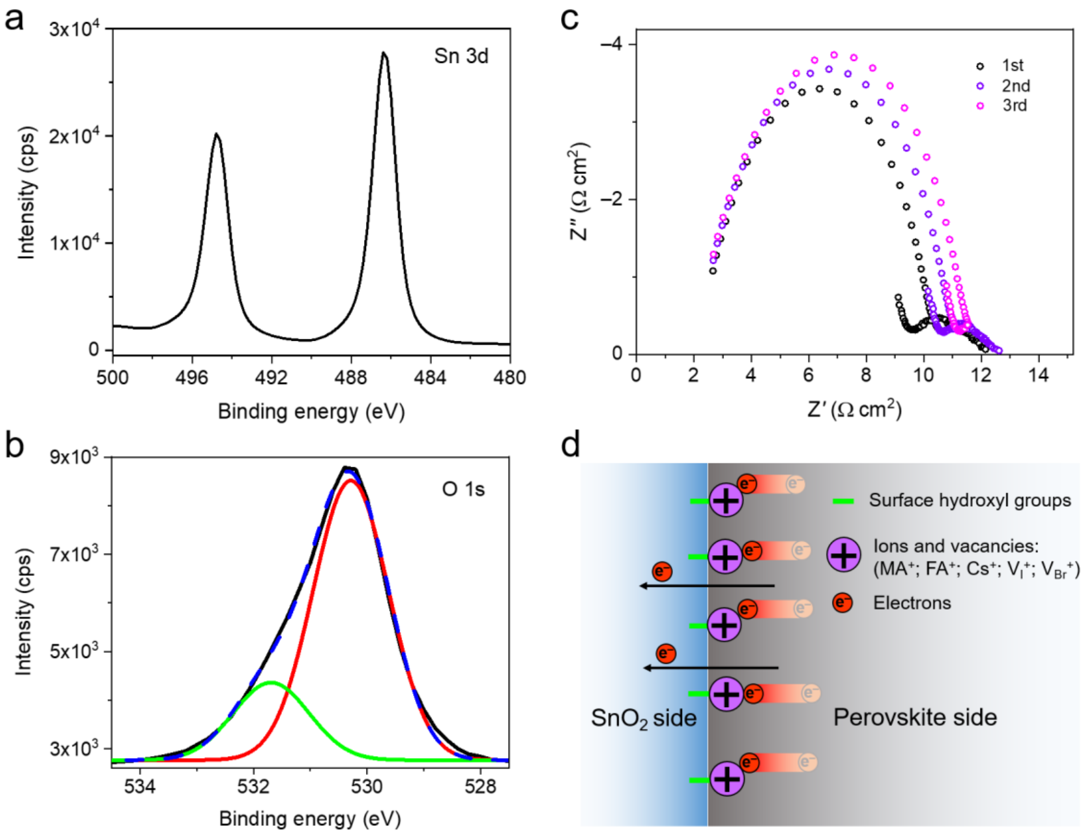

Figure 3-6. a, b) XPS peaks of a SnO_2 thin film in the Sn 3d (a) and O 1s (b) regions. c) EIS results of PSCs. The EIS measurements were repeated three times. d) Illustration showing the positive ion localization caused by the surface negative charges (–OH) of SnO_2. The possible mobile positive ions are MA^+ (methylammonium ion), FA^+ (formamidinium ion), Cs^+, V_I^+ (iodine vacancy), and V_{Br}^+: (bromine vacancy).

Electrochemical impedance spectroscopy (EIS) measurements were also carried out on the PSCs to characterize the interfacial charge dynamics caused by the localized positive ions. EIS measurements were performed using a Solartron 1260 frequency-response analyzer from 1 MHz to 70 mHz at an excitation amplitude of 20 mV. **Figure 3-6**c shows EIS data recorded at the V_{OC} condition under illumination. The EIS measurements consisted of a series of three consecutive measurements to check the consistency of the results during the entire EIS measurement procedure. The high-frequency semicircle for every consecutive spectrum increased. The low-frequency impedance did not have a clear pattern and did not change in shape or magnitude throughout the EIS measurement procedure. The increase in impedance at 0.07 Hz (lowest measured frequency) from 12.2 to 13.8 Ω cm^2 was predominantly caused by the high-frequency semicircle. This feature was previously attributed to poor electron extraction or recombination of charge carriers at the interfaces between the charge transport layer and the perovskite layer.[30] Recently, it was reported that the short-term increase in high-frequency impedance is ~100% reversible by keeping PSCs in the dark.[31] This feature was related to the ion migration and accumulation, which leads to the increased non-radiative recombination.[31] Therefore, I attributed the short-term increase in high-frequency impedance in **Fig. 3-6**c to the localized ionic charges at the negatively charged surface of SnO_2. The localized and accumulated ions including charged vacancies (especially, iodine vacancies) are well known to act as trap-assisted charge recombination centers in PSCs.[11,13,32,33] Therefore, these localized ions as depicted in **Fig. 3-6**d, could be one of the reasons of the observed large hysteresis.

It is possible to reduce the presence of –OH groups by annealing metal oxide films at high temperatures >800 °C.[34] However, after exposing a SnO_2 film to ambient condition even with short time, the –OH groups appear again.[35]. Therefore, I deactivated the surface –OH groups by using a SAM of a fullerene (C_{60}) derivative. The C_{60} derivative used here was C_{60} pyrrolidine tris-acid (CPTA) because this material has the ability to form strong chemical bonding with the SnO_2 surface[36,37] and to behave as a good electron acceptor. The CPTA-SAM was formed on the SnO_2 surface by spin-coating at 4,000 rpm for 30 sec from a CPTA solution in DMF with a concentration of 0.5 mg ml^{-1}. To remove physiosorbed CPTA molecules from the SnO_2 surface, the substrate was washed by DMF and dried at 100 °C for 5 min. The existence of the CPTA-SAM was confirmed by the appearance of XPS peaks from the C 1s and N 1s core levels and the decreased intensities of XPS peaks from the Sn 3d and O 1s core levels (**Fig. 3-7**). Even after washing the substrates with DMF, the intensities of all the XPS peaks from the C 1s, N 1s, Sn 3d and O 1s core levels were unchanged (**Fig. 3-7**), indicating that most of the CPTA molecules are chemically bounded with the SnO_2 surface.

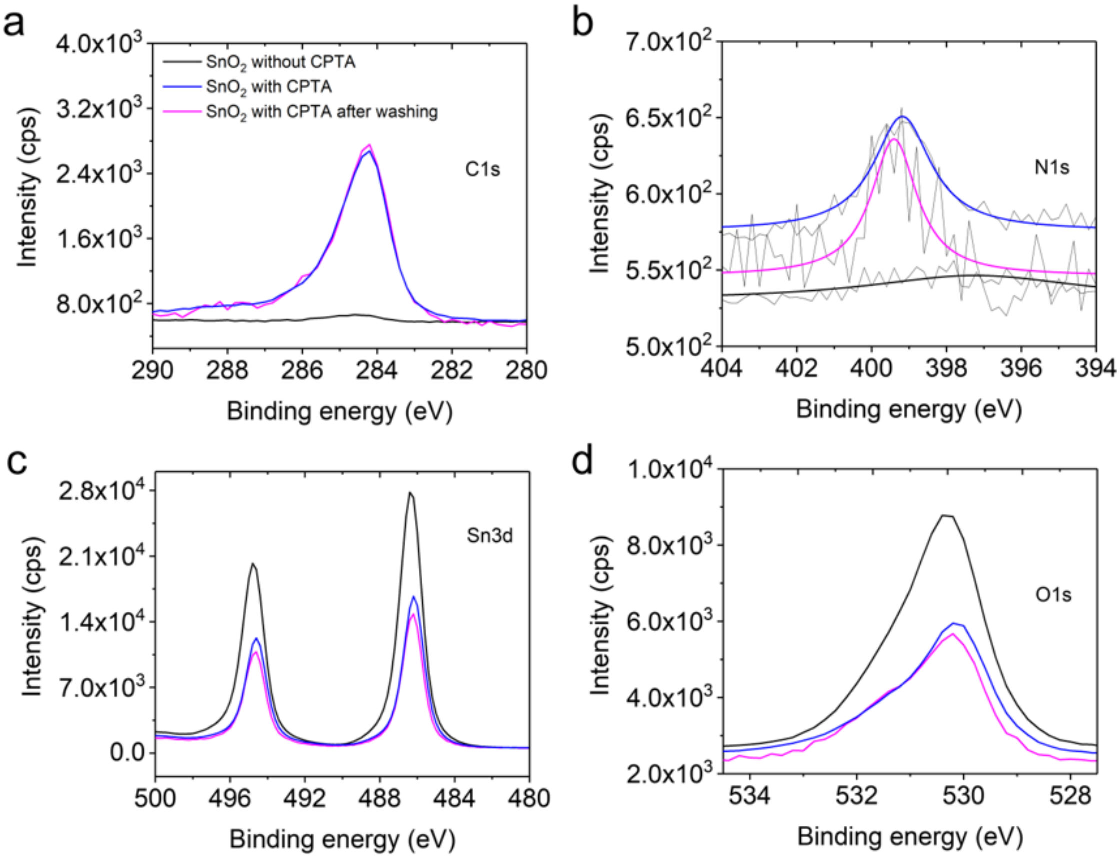

Figure 3-7 a) C 1s, b) N 1s, c) Sn 3d, and d) O 1s core level peaks in XPS results of SnO_2 films without (black lines) and with (colored lines) CPTA treatment. XPS was carried out before (blue lines) and after (pink lines) removing non-chemically-bounded CPTA molecules by washing with DMF.

With the CPTA-SAM formation, the –COO– groups were formed through the esterification reaction[36,38] between the CPTA molecules and the surface –OH groups. This was supported by the appearance of an XPS peak originating from the –COO– groups (**Fig. 3-8**). In addition, the amount of the –OH groups at the SnO_2 surface was reduced by ~60% after the CPTA-SAM formation.

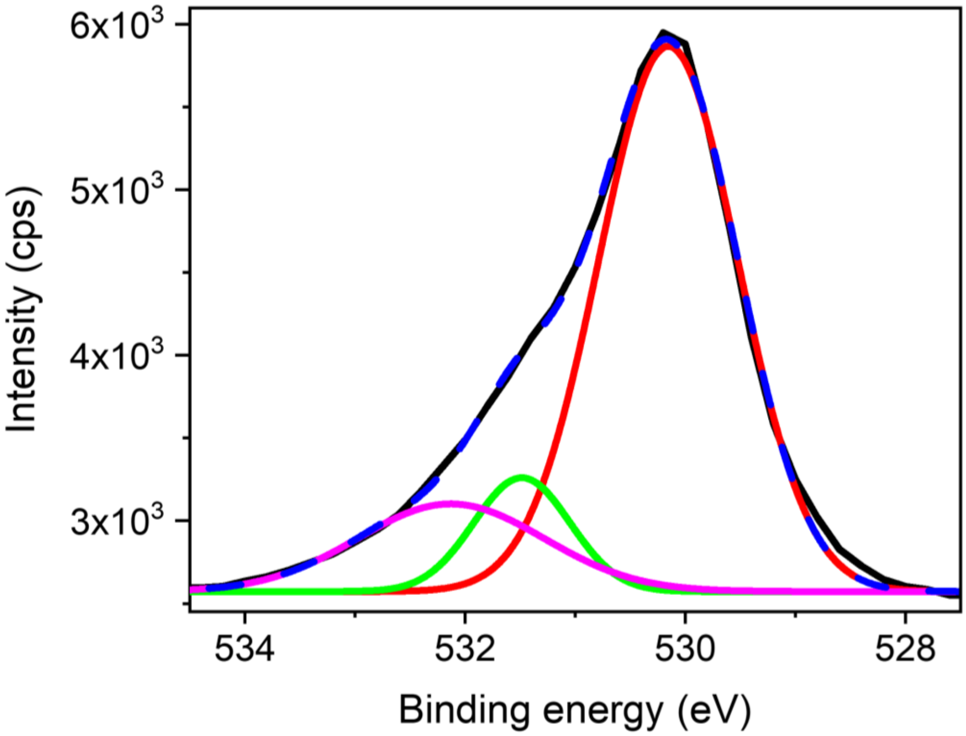

Figure 3-8. Deconvoluted O 1s core level peaks of SnO_2 treated with the SAM. (The measured spectrum (black line) was deconvoluted into three peaks. The red line corresponded to the oxygen inside the SnO_2 lattice (530.1 eV), the green line corresponded to the −OH groups at the SnO_2 surface (531.4 eV), and the pink line corresponded to the −COO− groups formed by the esterification reaction between the −OH groups and the CPTA molecules. The dashed black line was the sum of the deconvoluted three peaks.

To check the influence of deactivating the –OH groups by the CPTA-SAM as illustrated in **Fig. 3-9**a and b on the *J–V* hysteresis, I fabricated PSCs with the CPTA-SAM treatment. Adding the CPTA-SAM significantly reduced the *J–V* hysteresis of PSCs (**Fig. 3-9**c and **Table 3-3**). The average PCEs of eight devices with the CPTA-SAM were 18.06 and 18.12% in the forward and reverse scans, respectively (**Table 3-4**). In addition, no hysteresis was observed in PSCs with the CPTA-SAM even at a high temperature of 60 °C (**Fig. 3-9**d). Furthermore, there was no increase in the size of the semicircle in EIS results shown in **Fig. 3-9**e.

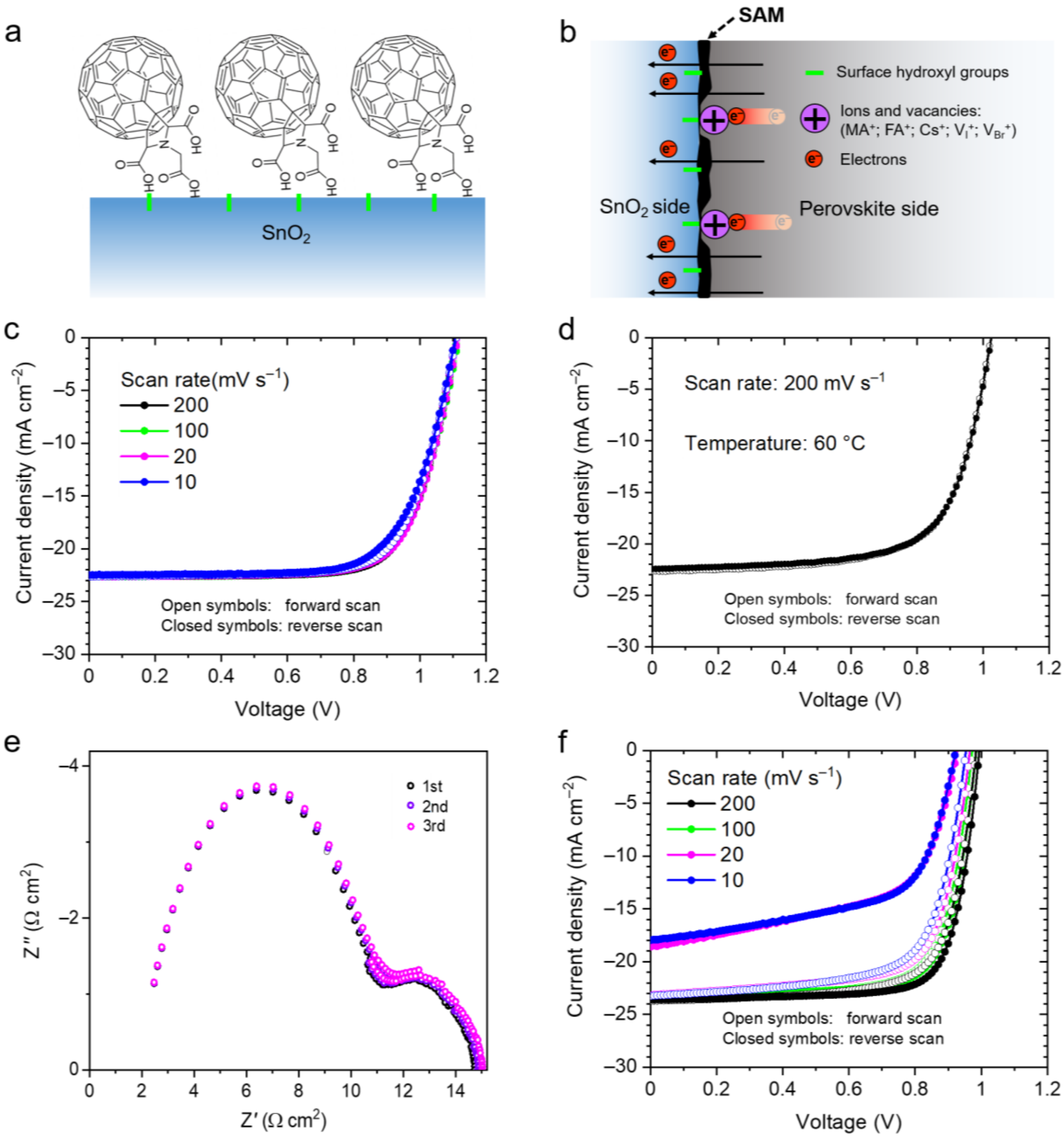

Figure 3-9. Illustration showing a) a CPTA-SAM formed on the SnO$_2$ surface and b) reduced localized ionic charges at the surface of SnO$_2$ because of the deactivation of the surface –OH groups. c) Scan-rate-dependent *J*–*V* curves of PSCs with the CPTA-SAM at room temperature. d) *J*–*V* curves measured at a fast scan rate of 200 mV s^{-1} at 60 °C. e) EIS results of PSCs with the CPTA-SAM. f) Scan-rate-dependent *J*–*V* curves of PSCs with a C$_{60}$ layer at room temperature.

Table 3-3. Scan-rate-dependent J_{sc}, V_{oc}, FF, PCE, and HI values of PSCs with the CPTA-SAM. These parameters were extracted from the *J–V* curves shown in **Fig. 3-9**c.

Scan rate (mV s^{-1})	Scan direction	Jsc (mA cm^{-2})	Voc (V)	FF	PCE (%)	HI
200	Forward	−22.61	1.11	0.74	18.46	0.00
	Reverse	−22.59	1.11	0.73	18.50	
100	Forward	−22.63	1.11	0.73	18.37	0.00
	Reverse	−22.58	1.12	0.73	18.43	
20	Forward	−22.64	1.11	0.73	18.25	0.00
	Reverse	−22.51	1.11	0.73	18.33	
10	Forward	−22.64	1.11	0.72	18.10	−0.04
	Reverse	−22.47	1.11	0.70	17.36	

Table 3-4. J_{sc}, V_{oc}, FF, PCE, and HI values of PSCs with the CPTA-SAM. These parameters were extracted from *J–V* curves measured at a scan rate of 200 mV s^{-1}.

	Scan direction	Jsc (mA cm^{-2})	Voc (V)	FF	PCE (%)	HI
Average (8 devices)	Forward	−22.25	1.11	0.73	18.06	0.00
	Reverse	−22.22	1.11	0.74	18.12	

The improved electron extraction to SnO_2 by the use of the CPTA-SAM is likely for the reduced hysteresis on the basis of literature.[39,40] Therefore, I prepared additional PSCs using a thin layer of pure C_{60}. Using this C_{60} layer can distinguish whether the decreased hysteresis resulted from the improved electron extraction or reduced localization of the positive ions because the surface –OH groups still exist below the C_{60} layer. As shown in **Fig. 3-10**, the PL intensity reduction was similar when a perovskite film was prepared on the C_{60} layer or the CPTA-SAM, indicating the similar electron extraction efficiency in both the cases. The reduced PL intensities also pointed to the existence of C_{60} even after the spin-coating of the perovskite film. The pronounced *J–V* hysteresis was observed when C_{60} was used in PSCs (**Fig. 3-9**f and **Table 3-5**) despite the similar electron extraction characteristics. This indicates that the deactivation of the surface –OH groups is very important for reducing the hysteresis. Furthermore, the

CPTA-SAM and the C_{60} layer could have different dipole moments, which may affect the ion localization and the PSC performance.

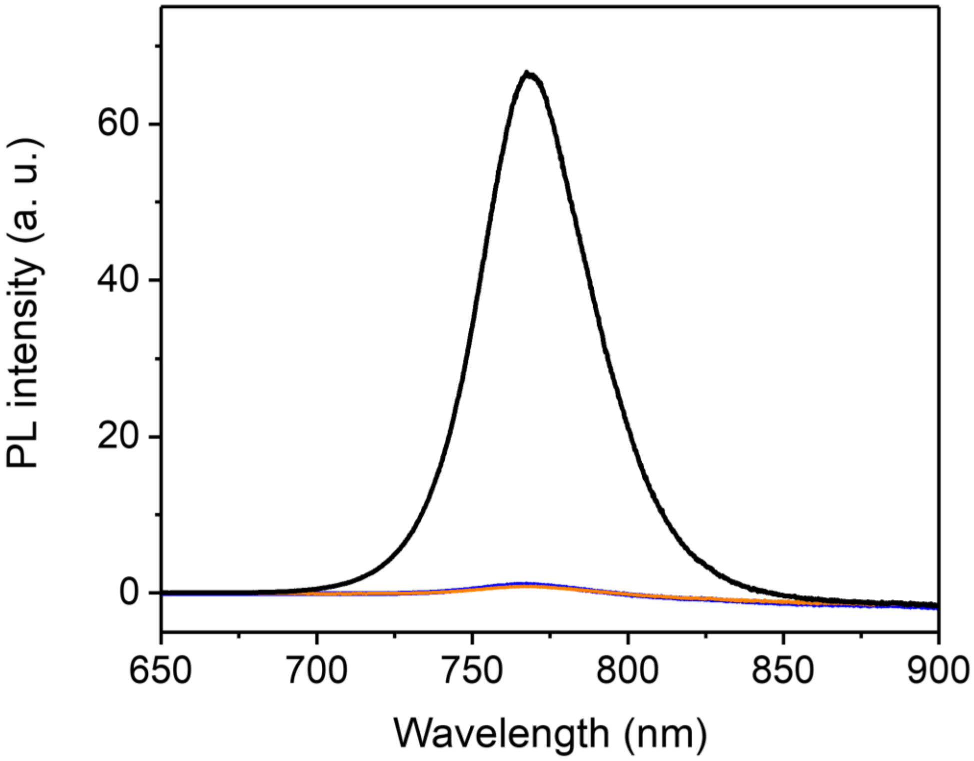

Figure 3-10. Steady-state PL spectra of perovskite films fabricated on different substrates of glass/ITO/SnO_2 (black line), glass/ITO/SnO_2/CPTA-SAM (blue line), and glass/ITO/SnO_2/C_{60} (orange line).

Table 3-5. Scan-rate-dependent J_{sc}, V_{oc}, FF, PCE, and HI values of PSCs with the C_{60} layer. These parameters were extracted from the *J*–*V* curves shown in **Fig. 3-9**f.

Scan rate (mV s^{-1})	Scan direction	Jsc (mA cm^{-2})	Voc (V)	FF	PCE (%)	HI
200	Forward	−23.71	0.98	0.73	16.94	0.06
	Reverse	−23.61	0.99	0.77	18.05	
100	Forward	−23.51	0.97	0.73	16.70	0.03
	Reverse	−23.33	0.98	0.75	17.19	
20	Forward	−23.18	0.97	0.71	15.82	−1.07
	Reverse	−18.59	0.93	0.44	7.63	
10	Forward	−23.24	0.95	0.69	15.22	−1.04
	Reverse	−17.96	0.92	0.45	7.46	

In addition to the ion migration, unbalanced charge transport,[41–43] ferroelectricity,[43,44] capacitive effect,[43,45] and defect-induced electronic traps[46] are known to induce the *J–V* hysteresis. There is a possibility that all these factors changed in our PSCs simultaneously when the SnO_2 surfaces were treated differently although every perovskite film fabricated on the untreated, CPTA-treated, and C_{60}-coated surfaces had similar morphologies (**Fig. 3-11**). In my future study, I will carry out additional experiments to clarify the more detailed origins of the *J-V* hysteresis.

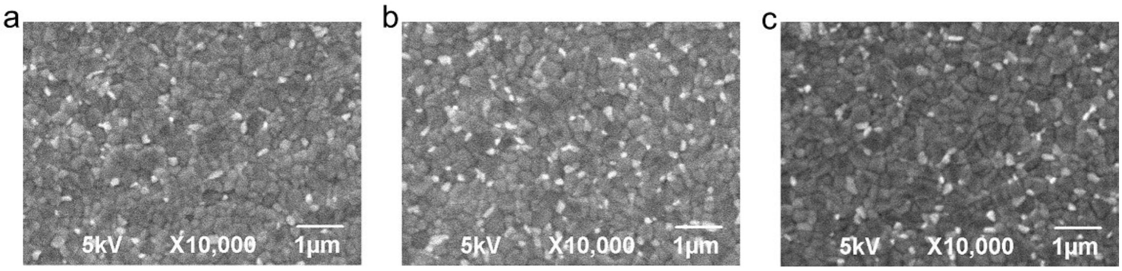

Figure 3-11. Top-view SEM images of perovskite films deposited on different substrates of a) glass/ITO/SnO_2, b) glass/ITO/SnO_2/CPTA-SAM, and c) glass/ITO/SnO_2/C_{60}.

Next, I measured the stability of PSCs with and without the CPTA-SAM under continuous illumination with an intensity of 100 mW cm^{-2} at room temperature. **Figure 3-12**a shows time dependence of the PCE evolution of PSCs. The PCEs of PSCs without the CPTA-SAM significantly dropped. It is worth mentioning here that PSCs with the CPTA-SAM had no decrease of the PCEs after 1,000 hours of the continuous illumination. Furthermore, I obtained the improved stability with the CPTA-SAM under the illumination even at a high temperature of 60 °C (**Fig. 3-12**b). I also investigated the stability of PSCs with the C_{60} layer. There was no improvement in stability when using C_{60} (**Fig. 3-13**). These results clearly demonstrated the importance of using the SAM treatment for fabricating stable PSCs

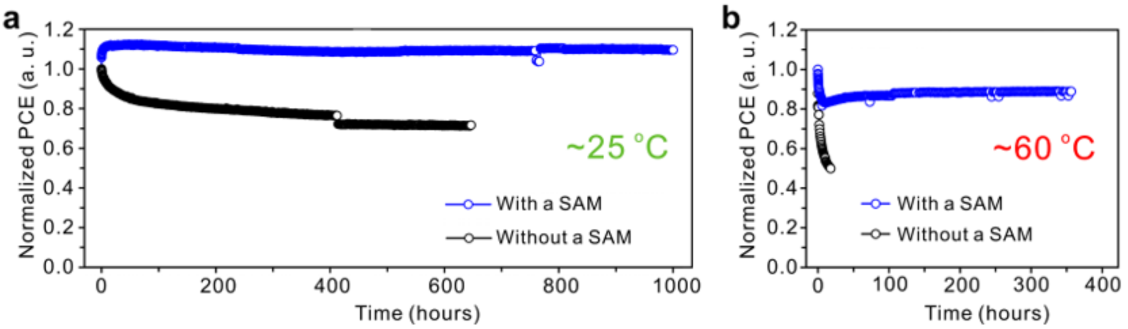

Figure 3-12. PCE evolution of PSCs at room temperature (25 °C) (a) and at elevated temperature (60 °C) (b).

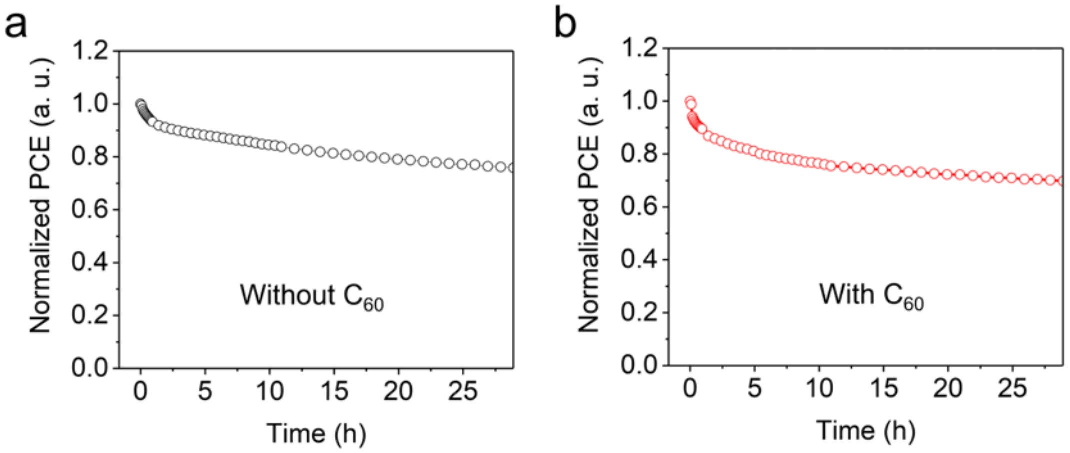

Figure 3-13. PCE evolution of PSCs a) without and b) with the C_{60} layer under continuous illumination at room temperature.

The aforementioned results also provide us information why metallic lead is formed at the interface between SnO_2 and perovskite layers as discussed in Chapter 2. It would reasonable that the localized positive ions trapped the electrons. Then, these trapped electrons interact with $[PbI_6]^{4-}$ octahedral to form the Pb^0 as illustrated in **Fig. 3-14** according to eq. 3-2 below.

$$[PbI_6]^{4-} + 2e^- \rightarrow Pb^0 \downarrow + 6I^- \qquad (3\text{-}2)$$

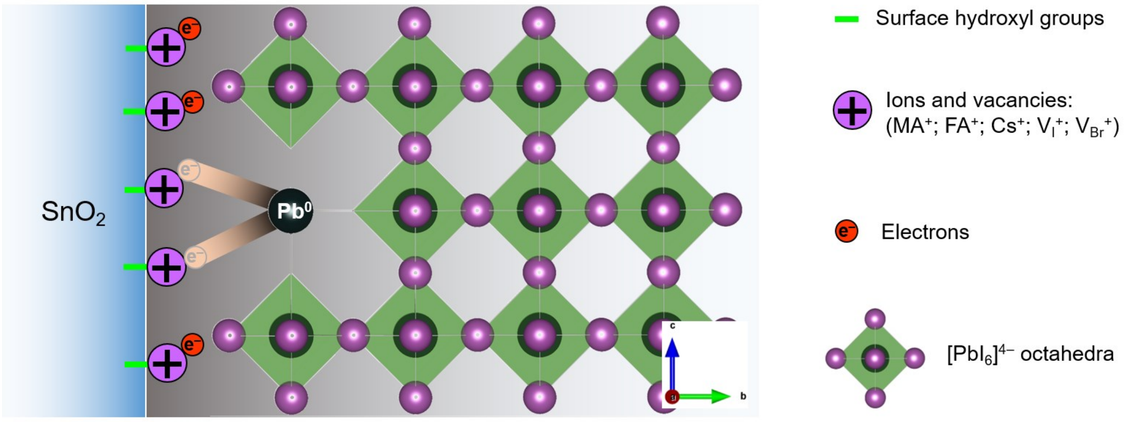

Fig. 3-14. Schematic of metallic Pb^0 formation during the degradation of PSCs.

3.3 Conclusions

In summary, I found that the *J*–*V* hysteresis and degradation can be suppressed by chemically modifying the SnO_2 surface with a SAM. I concluded that one reason for the suppressed hysteresis and degradation is the deactivation of the surface –OH groups which attract the positive ions. I obtained almost no degradation in PSCs with CPTA-SAM after 1,000 hours of continuous illumination at room temperature. These findings will provide insights into mechanisms of the hysteresis and long-term stability of PSCs.

References

[1] National renewable energy laboratory. Best research-cell efficiency chart. https://www.nrel.gov/pv/assets/pdfs/best-research-cell-efficiencies.20200406.pdf. (accessed: April 14, 2020).

[2] D. H. Kang, N. G. Park, *Adv. Mater.* **2019**, *31*, 1805214.

[3] W. Tress, N. Marinova, T. Moehl, S. M. Zakeeruddin, M. K. Nazeeruddin, M. Grätzel, *Energy Environ. Sci.* **2015**, *8*, 995.

[4] L. Meng, J. You, Y. Yang, *Nat. Commun.* **2018**, *9*, 5265.

[5] C. Eames, J. M. Frost, P. R. F. Barnes, B. C. O'Regan, A. Walsh, M. S. Islam, *Nat. Commun.* **2015**, *6*, 7497.

[6] S. Meloni, T. Moehl, W. Tress, M. Franckeviius, M. Saliba, Y. H. Lee, P. Gao, M. K. Nazeeruddin, S. M. Zakeeruddin, U. Rothlisberger, M. Graetzel, *Nat. Commun.* **2016**, *7*, 10334.

[7] D. Di Girolamo, N. Phung, F. U. Kosasih, F. Di Giacomo, F. Matteocci, J. A. Smith, M. A. Flatken, H. Köbler, S. H. T. Cruz, A. Mattoni, L. Cinà, B. Rech, A. Latini, G. Divitini, C. Ducati, A. Di Carlo, D. Dini, A. Abate, **2020**, *2000310*, DOI 10.1002/aenm.202000310.

[8] J. P. Correa-Baena, S. H. Turren-Cruz, W. Tress, A. Hagfeldt, C. Aranda, L. Shooshtari, J. Bisquert, A. Guerrero, *ACS Energy Lett.* **2017**, *2*, 681.

[9] R. A. Belisle, W. H. Nguyen, A. R. Bowring, P. Calado, X. Li, S. J. C. Irvine, M. D. McGehee, P. R. F. Barnes, B. C. O'Regan, *Energy Environ. Sci.* **2017**, *10*, 192.

[10] Y. Shao, Y. Fang, T. Li, Q. Wang, Q. Dong, Y. Deng, Y. Yuan, H. Wei, M. Wang, A. Gruverman, J. Shield, J. Huang, *Energy Environ. Sci.* **2016**, *9*, 1752.

[11] W. Tress, *J. Phys. Chem. Lett.* **2017**, *8*, 3106.

[12] S. A. L. Weber, I. M. Hermes, S. H. Turren-Cruz, C. Gort, V. W. Bergmann, L. Gilson, A. Hagfeldt, M. Grätzel, W. Tress, R. Berger, *Energy Environ. Sci.* **2018**, *11*, 2404.

[13] T. S. Sherkar, C. Momblona, L. Gil-Escrig, J. Ávila, M. Sessolo, H. J. Bolink, L. J. A. Koster, *ACS Energy Lett.* **2017**, *2*, 1214.

[14] K. Domanski, B. Roose, T. Matsui, M. Saliba, S. H. Turren-Cruz, J. P. Correa-Baena, C. R. Carmona, G. Richardson, J. M. Foster, F. De Angelis, J. M. Ball, A. Petrozza, N. Mine, M. K. Nazeeruddin, W. Tress, M. Grätzel, U. Steiner, A. Hagfeldt, A. Abate, *Energy Environ. Sci.* **2017**, *10*, 604.

[15] J. W. Lee, Z. Dai, T. H. Han, C. Choi, S. Y. Chang, S. J. Lee, N. De Marco, H. Zhao, P. Sun, Y. Huang, Y. Yang, *Nat. Commun.* **2018**, *9*, 3021.

[16] M. H. Futscher, J. M. Lee, L. McGovern, L. A. Muscarella, T. Wang, M. I. Haider, A. Fakharuddin, L. Schmidt-Mende, B. Ehrler, *Mater. Horizons* **2019**, *6*, 1497.

[17] W. Zhou, S. Chen, Y. Zhao, Q. Li, Y. Zhao, R. Fu, D. Yu, P. Gao, Q. Zhao, *Adv. Funct. Mater.* **2019**, *29*, 1809180.

[18] S. Yang, S. Chen, E. Mosconi, Y. Fang, X. Xiao, C. Wang, Y. Zhou, Z. Yu, J. Zhao, Y. Gao, F. De Angelis, J. Huang, *Science* **2019**, *365*, 473.

[19] S. Bai, P. Da, C. Li, Z. Wang, Z. Yuan, F. Fu, M. Kawecki, X. Liu, N. Sakai, J. T. W. Wang, S. Huettner, S. Buecheler, M. Fahlman, F. Gao, H. J. Snaith, *Nature* **2019**, *571*, 245.

[20] J. Cao, S. X. Tao, P. A. Bobbert, C. P. Wong, N. Zhao, *Adv. Mater.* **2018**, *30*, 1707350.

[21] F. Wu, B. Bahrami, K. Chen, S. Mabrouk, R. Pathak, Y. Tong, X. Li, T. Zhang, R. Jian, Q. Qiao, *ACS Appl. Mater. Interfaces* **2018**, *10*, 25604.

[22] G. A. Nemnes, C. Besleaga, A. G. Tomulescu, A. Palici, L. Pintilie, A. Manolescu, I. Pintilie, *Sol. Energy* **2018**, *173*, 976.

[23] Y. Jiang, Y. Feng, X. Sun, R. Qin, H. Ma, *J. Phys. D. Appl. Phys.* **2019**, *52*, 385501.

[24] Y. Zou, R. J. Holmes, *Adv. Energy Mater.* **2016**, *6*, 1501994.

[25] H. Z. Abdullah, S. H. Amirnordin, S. A. B. Ab. Aziz, H. A. Rahman, H. Taib, *Adv. Mater. Res.* **2013**, *795*, 334.

[26] G. S. Han, J. Kim, S. Bae, S.-H. Han, Y. J. Kim, O. Y. Gong, P. Lee, M. J. Ko, H. S. Jung, *ACS Energy Lett.* **2019**, *4*, 1845.

[27] M. H. Futscher, T. Schultz, J. Frisch, M. Ralaiarisoa, E. Metwalli, M. V Nardi, J. Phys.: Condens. Matter **2019**, *31*, 064002.

[28] C. Donley, D. Dunphy, D. Paine, C. Carter, K. Nebesny, P. Lee, D. Alloway, N. R. Armstrong, *Langmuir* **2002**, *18*, 450.

[29] H. Jadhav, S. Suryawanshi, M. A. More, S. Sinha, *Appl. Surf. Sci.* **2017**, *419*, 764.

[30] H. J. Snaith, A. Pockett, P. J. Cameron, G. E. Eperon, L. M. Peter, N. Sakai, *Phys. Chem. Chem. Phys.* **2017**, *19*, 5959.

[31] D. Klotz, G. Tumen-Ulzii, C. Qin, T. Matsushima, C. Adachi, *RSC Adv.* **2019**, *9*, 33436.

[32] P. Calado, A. M. Telford, D. Bryant, X. Li, J. Nelson, B. C. O'Regan, P. R. F. Barnes, *Nat. Commun.* **2016**, *7*, 13831.

[33] A. Pockett, M. J. Carnie, *ACS Energy Lett.* **2017**, *2*, 1683.

[34] T. Morimoto, M. Nagao, F. Tokuda, *Bull. Chem. Soc. Jpn.* **1968**, *41*, 1533.

[35] R. G. Pavelko, H. Daly, C. Hardacre, A. A. Vasiliev, E. Llobet, *Phys. Chem. Chem. Phys.* **2010**, *12*, 2639.

[36] Y. C. Wang, X. Li, L. Zhu, X. Liu, W. Zhang, J. Fang, *Adv. Energy Mater.* **2017**, *7*, 1701144.

[37] M. Zhong, Y. Liang, J. Zhang, Z. Wei, Q. Li, D. Xu, *J. Mater. Chem. A* **2019**, *7*, 6659.

[38] J. Chen, X. Zhao, S. Kim, N. Park, *Adv. Mater.* **2019**, *31*, 1902902.

[39] J. Carrillo, A. Guerrero, S. Rahimnejad, O. Almora, I. Zarazua, E. Mas-Marza, J. Bisquert, G. Garcia-Belmonte, *Adv. Energy Mater.* **2016**, *6*, 1502246.

[40] Y. Shao, Z. Xiao, C. Bi, Y. Yuan, J. Huang, *Nat. Commun.* **2014**, *5*, 5784.

[41] Q. Jiang, L. Zhang, H. Wang, X. Yang, J. Meng, H. Liu, Z. Yin, J. Wu, X. Zhang, J. You, *Nat. Energy* **2017**, *2*, 16177.

[42] D. Yang, R. Yang, K. Wang, C. Wu, X. Zhu, J. Feng, X. Ren, G. Fang, S. Priya, S. (Frank) Liu, *Nat. Commun.* **2018**, *9*, 3239.

[43] B. Chen, M. Yang, S. Priya, K. Zhu, *J. Phys. Chem. Lett.* **2016**, *7*, 905.

[44] J. Wei, Y. Zhao, H. Li, G. Li, J. Pan, D. Xu, Q. Zhao, D. Yu, *J. Phys. Chem. Lett.* **2014**, *5*, 3937.

[45] B. Chen, M. Yang, X. Zheng, C. Wu, W. Li, Y. Yan, J. Bisquert, G. Garcia-Belmonte, K. Zhu, S. Priya, *J. Phys. Chem. Lett.* **2015**, *6*, 4693.

[46] J. W. Lee, S. G. Kim, S. H. Bae, D. K. Lee, O. Lin, Y. Yang, N. G. Park, *Nano Lett.* **2017**, *17*, 4270.

Chapter 4

Understanding the degradation of spiro-OMeTAD-based perovskite solar cells at high temperature

G. Tumen-Ulzii, C. Qin, D. Klotz, M. R. Leyden, T. Matsushima, and C. Adachi, *Advanced Energy Materials,* (2020) (submitted).

4.1 Introduction

Highly efficient PSCs with PCEs of over 20% have been reported[1–3] and the choosing an appropriate HTL material is the crucial issue. Since the first introduction of a solid-state HTL material in 2012,[4] spiro-OMeTAD has continuously been used for PSCs with proper dopants.[5] While spiro-OMeTAD is the best choice for fundamental research because of the superior performance of PSCs with this material being realized, a high material cost of spiro-OMeTAD, which is related to its so many synthesis steps, restricts the development of low-cost PSCs towards commercialization.[6] Therefore, the recent research trend is to find lower-cost alternative HTL materials without reducing PSC performance. For this purpose, various types of HTL materials including small organics,[7–9] polymers,[10–12] and inorganics[13–15] have been developed. Among these reported materials, spiro-OMeTAD is still excellent material in terms of PCEs.

Besides the PCEs and material cost, the long-term stability is important for future commercialization of PSCs. Recently, PSCs employing spiro-OMeTAD has delivered promising stability at room temperature.[3,16] PSCs should maintain their performance even at high temperature for the practical use. However, spiro-OMeTAD-based PSCs loss their performance quickly at high temperature.[17–20] To understand this reason, researchers have focused on high-temperature degradation mechanisms of spiro-OMeTAD-based PSCs. For example, Jena et al. studied PSCs with spiro-OMeTAD after the operation at high temperature. They removed the degraded metal and spiro-OMeTAD layers and, then, re-fabricated new spiro-OMeTAD and metal layers on top of the perovskite layer. In this case, PCEs returned to an initial value.[17] There was no decrease in PCE when the perovskite layer was heated at high temperature before fabricating the spiro-OMeTAD layer.[18] After the deposition of the spiro-OMeTAD layer without the upper metal layer, heating caused PCEs to decrease.[18] Considering these reports, the high-temperature degradation of PSCs is directly related to the spiro-OMeTAD layer and not the other layers.

In a previous study, it has been reported that the high-temperature degradation is caused by Au diffusion into the spiro-OMeTAD layer[20] or the crystallization of the spiro-OMeTAD layer because of reduced glass transition temperature (T_g).[17,21] However, more fundamental studies are needed to understand the other possible degradation mechanisms.

Therefore, I studied the high-temperature degradation of spiro-OMeTAD-based PSCs in this chapter. I found that post-doping of spiro-OMeTAD by iodine diffused from the perovskite layer is a feasible reason for the degradation of PSCs at a high temperature of 85 °C. The HOMO level of the spiro-OMeTAD layer changed from −5.3 to −5.8 eV by the iodine doping, which led to the formation of a hole extraction barrier with the perovskite layer having the VBM of −5.5 eV. I confirmed the reduced hole extraction by a significant increase in PL intensity from the spiro-OMeTAD layer deposited on the perovskite layer after heating at 85 °C. When I inserted an iodine-blocking layer between the spiro-OMeTAD layer and the perovskite layer or replaced the iodine-containing perovskite layer with an iodine-free (bromine-based) perovskite layer, I obtained better stability even at 85 °C, because of the suppressed iodine doping into spiro-OMeTAD.

4.2 Results and discussion

I used a spin-coated S-2 perovskite film with the composition of $Cs_{0.05}(FA_{0.85}MA_{0.15})_{0.95}(PbI_{0.85}Br_{0.15})_3$ as the light absorber of PSCs because of its high efficiency and stability as adopted in Chapter 2. The fabricated PSCs architecture (ITO/SnO_2/perovskite/spiro-OMeTAD/Au), device fabrication conditions and evaluation methods were the same as those shown in Chapter 2. Thirty-six PSCs fabricated in the same batch and encapsulated without exposure to air had very similar PCEs (**Fig. 4-1**a), along with negligible hysteresis in their *J–V* curves measured in the consecutive forward and reverse scans (**Fig. 4-1**b). Further, I evaluated the storage stability in the dark at room temperature (~25 °C) or high temperature (85±1 °C). For the evaluation of the dark storage durability, *J−V* curves of the encapsulated PSCs were measured periodically under the AM 1.5G 100 mW cm^{-2} simulated solar illumination. In between the *J−V* scans, the PSCs were stored at ~25 or ~85 °C in the dark at the open-circuit condition.

The PSCs did not degrade at 25 °C for 120 hours of the dark storage (black circles in **Fig. 4-1**c). However, the serious PSC degradation occurred within 20 hours of the dark storage at 85 °C (red squares in **Fig. 4-1**c). The similar behaviour was reported in the previous literature.[17,22]

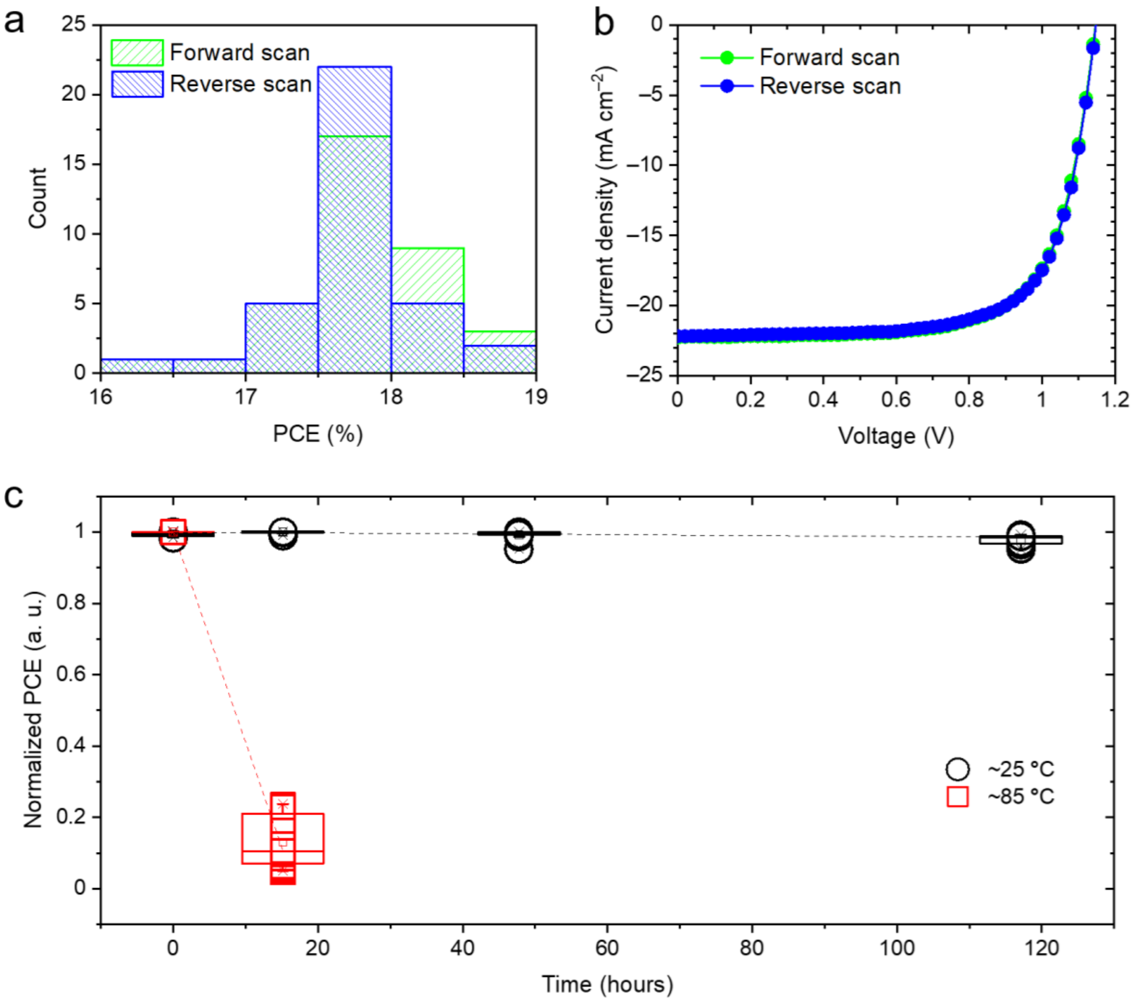

Figure 4-1. a) PCEs of thirty-six PSCs measured in the forward and reverse scans. b) *J*–*V* curves of a representative PSC. c) Dark storage stability of PSCs at ~25 or ~85 °C. Twelve PSCs were tested at each temperature, and average values are shown in (c).

It has been reported that the PSC degradation at high temperature is due to the morphological degradation of spiro-OMeTAD layer, which is associated with the reduced T_g of the spiro-OMeTAD layer by chemical doping.[1,17,21] The morphological degradation of spiro-OMeTAD layer is easily observed by polarized optical microscope.[17,21] Therefore, I first measured the T_g of our chemically undoped and doped spiro-OMeTAD powder. For the doped powder, the spiro-OMeTAD solution mixed with LiTFSI, 4-tBP, and FK-209 dopants with same conditions mentioned in the experimental section of Chapter 2 was prepared. Doped spiro-OMeTAD powder was obtained by drying this solution in vacuum overnight, followed by heating at 130 °C for 30 min in vacuum. Differential scanning calorimetry (DSC) was performed on the undoped and doped spiro-OMeTAD powder using a calorimeter (Netzsch DSC204 F1 Phoenix) at a scan rate of 10 °C min^{-1}. The undoped powder used here means the as-purchased product. The T_g was determined during the second DSC scan.

Figure 4-2a shows DSC results. The T_g value of the doped spiro-OMeTAD powder was ~116 °C, while the T_g value of the undoped spiro-OMeTAD powder was 125 °C. The reduced T_g by the chemical doping is consistent with literature.[1,17,21] Next, I measured polarized optical microscope images of the chemically doped spiro-OMeTAD layers deposited on the perovskite layer after storing at 25 or 85 °C for 20 hours (**Fig. 4-2**b and c) to check the crystallization of spiro-OMeTAD layers as reported previously.[17,21] I did not clearly see the crystallization from our samples heating at 85 °C, probably because the T_g measured here is higher than the heating temperature of 85 °C. On the other hand, heating the spiro-OMeTAD layer directly fabricated on a glass substrate at 140 °C, which is higher than the T_g, resulted in the significant crystallization (**Fig. 4-2**d). Thus, the serious degradation of PSCs at 85 °C as discussed in **Fig. 4-1**c may not be correlated with the morphological degradation.

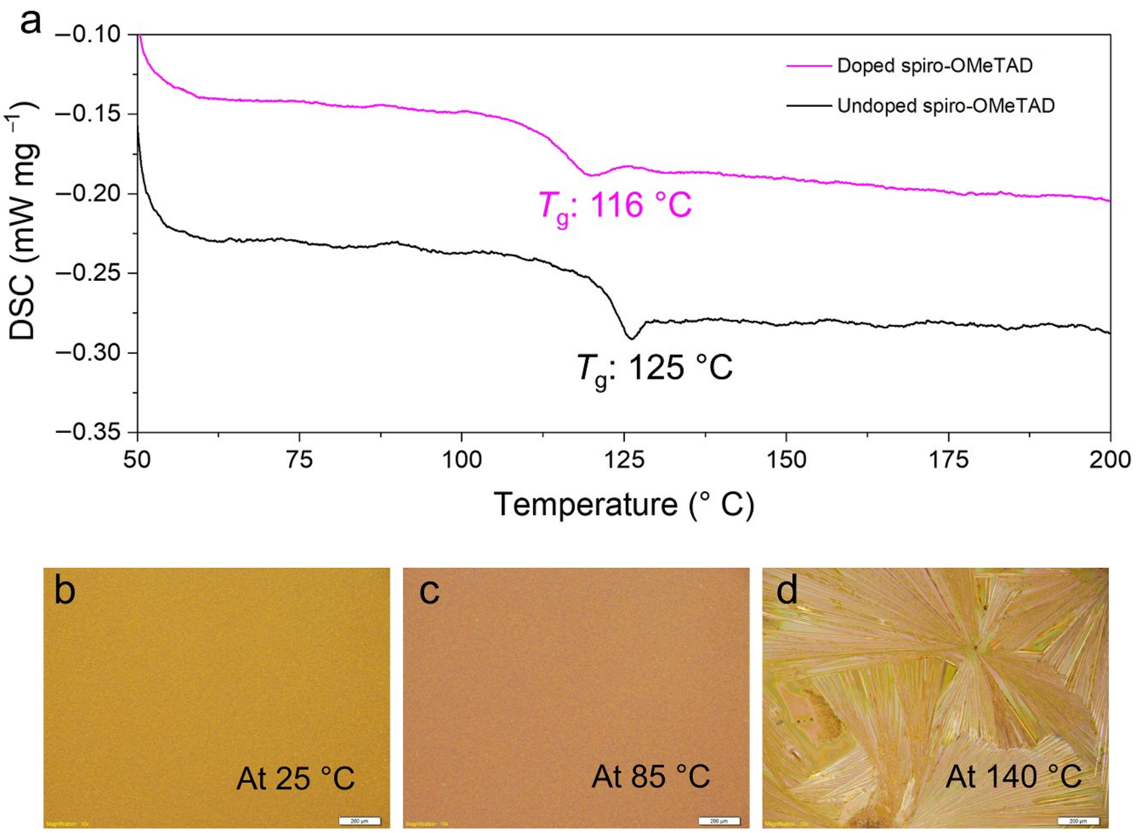

Figure 4-2. a) DSC results of undoped (black) and doped (pink) spiro-OMeTAD power. b−d) Polarized optical microscope images of doped spiro-OMeTAD films after storing at 25 (b) or 85 °C (c) for 20 hours or at 140 °C for 3 hours (d).

To investigate the chemical degradation of spiro-OMeTAD, I used matrix assisted laser desorption/ionization-time of flight-mass spectrometry (MALDI–TOF–MS). Samples of glass substrate/ITO/SnO_2/perovskite/spiro-OMeTAD were prepared and stored at 25 or 85 °C for 20 hours. The spiro-OMeTAD layer was selectively washed away by CB from the aforementioned film samples. This CB solution containing spiro-OMeTAD was used for MALDI–TOF–MS (BRUKER Autoflex-III).

I did not clearly detect the chemical-structure change of spiro-OMeTAD after storing the film samples at 25 or 85 °C for 20 hours, because of the observation of only a single peak at 1225, which corresponds to the molecular weight of intact spiro-OMeTAD (**Fig. 4-3**a). Furthermore, I conducted XPS for the elemental analysis at the surfaces of the spiro-OMeTAD layers after storing at 25 or 85 °C for 20 hours. There was almost no observable change of the C 1s, O 1s, and N 1s core level peaks (**Fig. 4-3**(b–d)), and other peaks originating from the dopants (**Fig. 4-4**). Therefore, the large chemical degradation is unlikely in the spiro-OMeTAD layer even after heating at 85 °C.

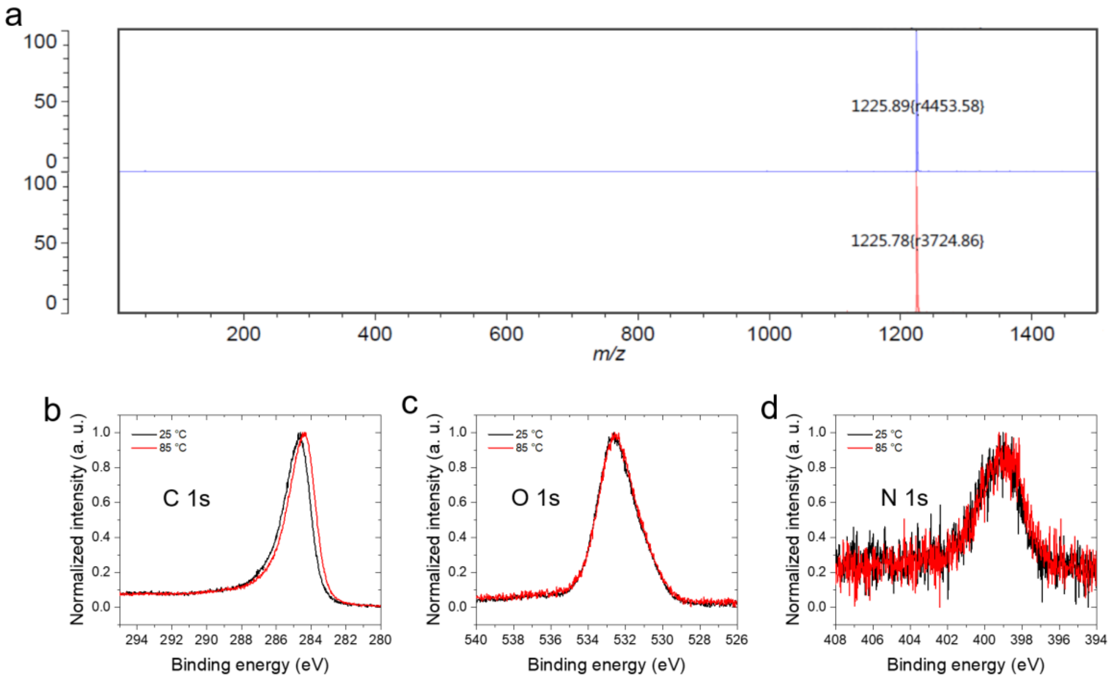

Figure 4-3. a) MALDI–TOF–MS results of spiro-OMeTAD after storing at 25 or 85 °C. b–d) XPS results of C 1s (b), O 1s (c), N 1s (d) core levels of spiro-OMeTAD after storing at 25 or 85 °C.

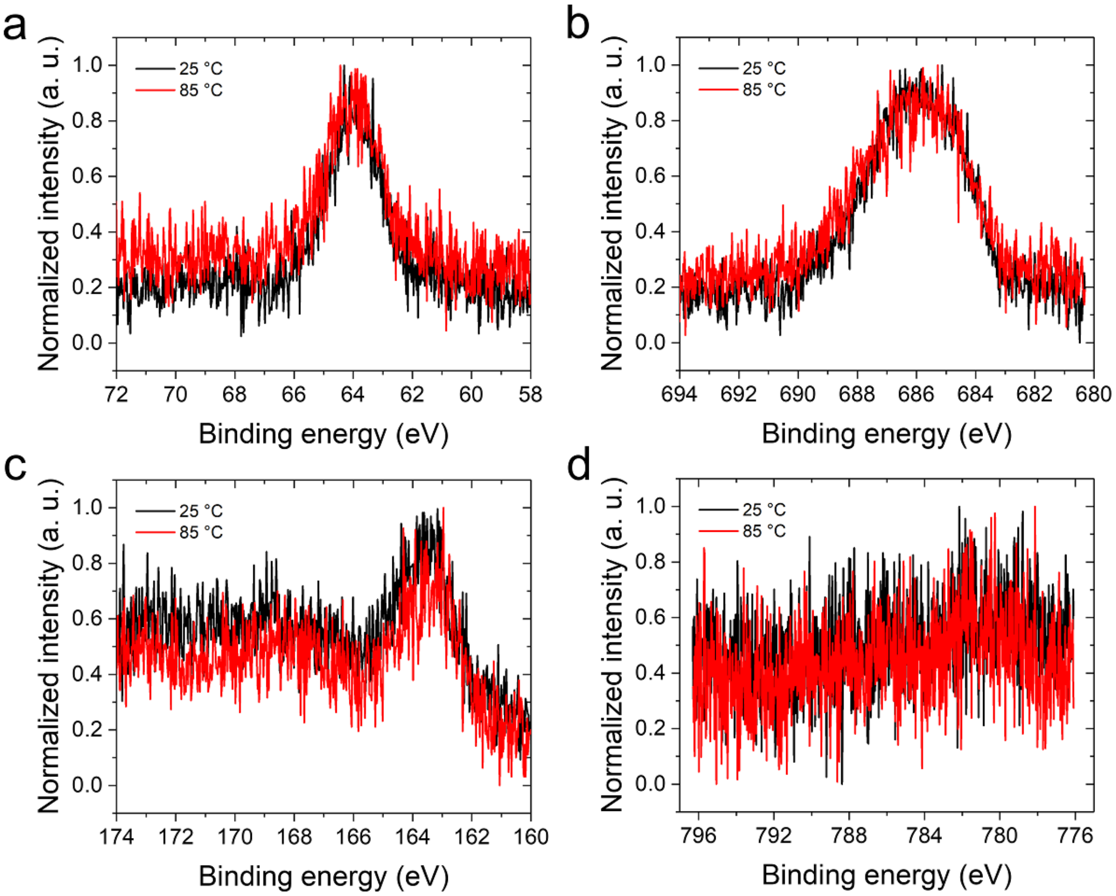

Figure 4-4. XPS results of (a) Li 1s, (b) F 1s, (c) S 2p, and (d) Co 2p peaks of the dopant elements in spiro-OMeTAD films.

To investigate a reason why PSCs quickly degraded at 85 °C, I measured the HOMO levels of the spiro-OMeTAD layers using photoelectron yield spectroscopy (AC-3, Rikenkeiki). The sample structure used here was glass substrate/ITO/SnO_2/perovskite/spiro-OMeTAD, which were stored at 25 or 85 °C for 20 hours.

Figure 4-5a shows photoelectron yield spectroscopy results. The spiro-OMeTAD layers had a HOMO level of about −5.3 eV after these layers were stored at 25 °C for 20 hours. This value was the same as that of as-spin-coated spiro-OMeTAD layers and is consistent with the previously reported literature.[1] However, after heating at 85 °C for 20 hours, their HOMO level increased to about −5.8 eV. Since the VBM of the perovskite layer is −5.5 eV, which was measured using the same method, the HOMO level of spiro-OMeTAD is higher than the VBM of perovskite layer. On the other hand, as explained in Chapter 1, excitons are formed in perovskite layer by the photoexcitation. Then the excitons are dissociated into free charges of electrons and holes. Subsequently, electrons are extracted into SnO_2, and holes are extracted into spiro-OMeTAD. However, the increase in the HOMO level of spiro-OMeTAD can affect the hole extraction from perovskite into spiro-OMeTAD. The difference in energy levels of VBM of perovskite and HOMO level of spiro-OMeTAD indicates the energy barrier for the hole extraction as illustrated in **Fig. 4-5**b. Therefore, I assume that the inefficient hole extraction is one of the potential reasons for the significant PSC degradation at the high temperature.

To further investigate the hole extraction, I measured steady-state PL from the perovskite layers (**Fig. 4-5**c). I observed strong PL from the perovskite layer without spiro-OMeTAD (green line). The deposition of spiro-OMeTAD on top of the perovskite layer induced a significant decrease in the PL intensity (black line), indicating efficient hole extraction.[17,23] It is worth mentioning here that, after heating the perovskite/spiro-OMeTAD samples at 85 °C for 20 hours, the PL intensities significantly increased (red line). This is proof of the inefficient hole extraction resulting from the lower-lying HOMO level of the spiro-OMeTAD layer after the heating. Zhao et al. reported a similar increase in PL intensity and attributed this effect to loss of the hole extraction because of the crystallization of spiro-OMeTAD at 85 °C.[17] However, I did not clearly see the crystallization in my heated spiro-OMeTAD layers as discussed earlier.

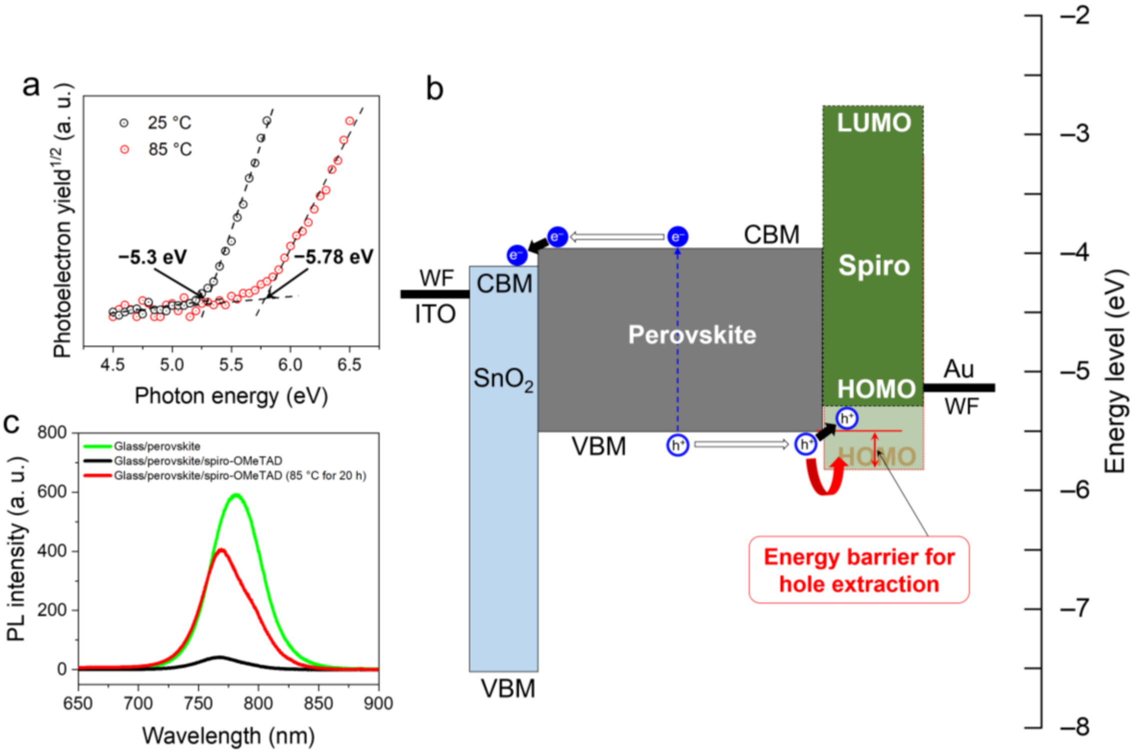

Figure 4-5. a) Photoelectron yield spectroscopy results of the spiro-OMeTAD layers stored at 25 or 85 °C. b) Energy-level diagrams of PSCs before and after heating spiro-OMeTAD at 85 °C. c) PL spectra of the perovskite/spiro-OMeTAD layers.

At high temperature, iodide ions (I^-) diffuse into the spiro-OMeTAD layer from the perovskite layer, which decreases the electrical conductivity of spiro-OMeTAD because I^- ions behave as a reducing agent.[22,24] Iodine (I_2) was reportedly released from a perovskite layer at high temperature.[25,26] Triiodide (I^{3-}) ions can be spontaneously formed by the reaction between I^- and I_2.[27,28] Since both I^{3-} and I_2 have the oxidizing ability,[29–31] the post-doping of spiro-OMeTAD with I^{3-} or I_2 is one origin of making the HOMO level deeper although what kind of interaction between spiro-OMeTAD and I^{3-} or I_2 exists in the PSC architecture has not been clear yet. Considering the higher redox potential of I_2/I^- than that of I_3^-/I^-,[30,31] I_2 could be a stronger oxidizing agent than I^{3-} for spiro-OMeTAD.

To detect the iodine release from the perovskite layer, I performed a simple experiment as follows. I soaked a perovskite film into toluene (**Fig. 4-6**a). After heating toluene at 85 °C for one hour, the toluene color apparently became pink (**Fig. 4-6**b). The absorption peaks emerged at ~300 and ~500 nm in toluene stored with the perovskite sample (**Fig. 4-6**c). These two peaks were assigned to iodine[28,32,33] and had stronger in absorbance when the toluene was stored at 85 °C than at 25 °C. The iodine release from a perovskite layer was also detected in vacuum using mass spectrometry.[25] Although the I_2 release in toluene or in vacuum is not directly correlated with that in solid-state films, it strongly suggests that iodine comes from the perovskite layer, especially at high temperature.

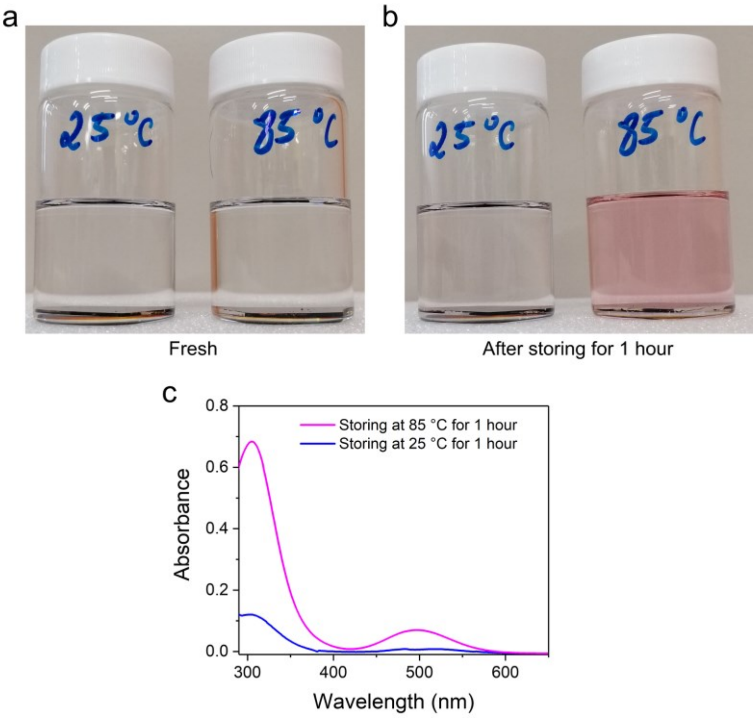

Figure 4-6. Photographs of toluene, in which a perovskite film was immersed. a) was taken just after the perovskite immersion. b) was taken after toluene was stored at 25 or 85 °C for one hour. c) Absorption spectra of toluene after storing at 25 or 85 °C for one hour.

To further check the post-doping of spiro-OMeTAD with iodine, I exposed spiro-OMeTAD films to I_2 vapour as illustrated in **Fig. 4-7**a. The sample architecture was glass substrate/ITO/spiro-OMeTAD. This sample and 0.2 g of solid I_2 particles were placed inside a tightly sealed glass vessel with a volume of 50 cm^3. After the I_2 exposure, the samples were stored in the vacuum for 10 min to remove the excess I_2 from the spiro-OMeTAD layer surfaces. Then, the HOMO levels were measured using the same photoelectron yield spectroscopy. **Figure 4-7**b shows a plot of measured HOMO levels of spiro-OMeTAD as a function of I_2 exposure time. The HOMO levels gradually became deeper over time. After the I_2 exposure for 90 seconds, the HOMO value reached −5.8 eV, which is similar to that of the spiro-OMeTAD layer after heating at 85 °C (**Fig. 4-5**a).

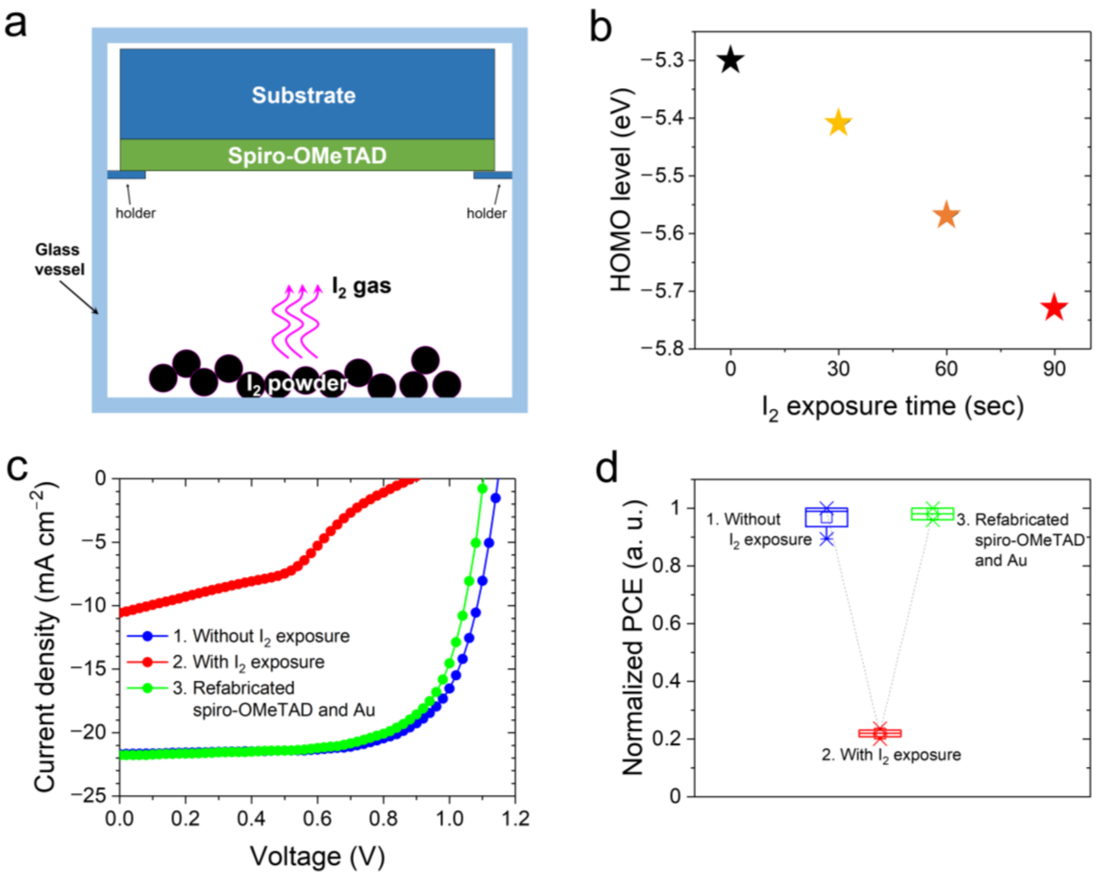

Figure 4-7. a) Sketch of the I_2 exposure to the spiro-OMeTAD layer. b) HOMO levels of spiro-OMeTAD as a function of I_2 exposure time. c) *J*–*V* curves of PSCs fabricated with spiro-OMeTAD unexposed (blue) or exposed (red) to I_2 for 90 sec. The green circles in (c) indicate the recovered PSC performance by refabricating the fresh spiro-OMeTAD and Au layers. d) Change of PCEs calculated from four PSCs fabricated in the same batch.

I fabricated PSCs by vacuum-depositing the Au electrode on top of the spiro-OMeTAD layer exposed to I_2 for 90 sec. As can be seen in **Fig. 4-7**c and d, the I_2-exposed PSCs had the degraded PCEs of ~3.7%, which are significantly lower than those of I_2-unexposed PSCs (~17.4%). On the basis of the earlier discussion, the lower device performance is probably due to the I_2 doping, making the HOMO level of spiro-OMeTAD deeper. Next, I removed the Au electrode and the I_2-exposed spiro-OMeTAD layer from the perovskite surface in the aforementioned low-performance PSCs. Then, I refabricated fresh spiro-OMeTAD and Au layers on the same perovskite layer without the I_2 exposure. Interestingly, this refabrication procedure increased the PCEs to 16.7%. These results suggest that the I_2 exposure affects the spiro-OMeTAD layer and not the other layers and is one origin of the PSC degradation at the high temperature.

Other than the interaction of spiro-OMeTAD with iodine, iodine vacancies formed in a perovskite film as a result of the iodine migration should have an impact on the performance of PSCs. To understand this effect, I heated samples with a structure of glass substrate/ITO/SnO_2/perovskite at 85 °C for 20 hours. This heating condition is similar to that used to study the PSC degradation at high temperature in this chapter. The reference samples were stored at 25 °C for 20 hours. Then, I deposited the spiro-OMeTAD and Au electrodes on top of heated and unheated samples to complete the PSCs. **Figure 4-8** shows the performance statistics of PSCs. The J_{SC} and FF of PSCs did not change largely when the perovskite films were stored at different temperatures. However, the V_{OC} slightly decreased from ~1.1 to ~1.05 V, and the reason of which is still unclear. This V_{OC} decrease led to a decrease in PCE from ~17 to ~16%. Since this PCE decrease by heating is much smaller than that of complete PSCs when operated at

85 °C (**Fig. 4-1c)**, the iodine doping into spiro-OMeTAD more significantly causes the PSC performance degradation than the iodine vacancy formation.

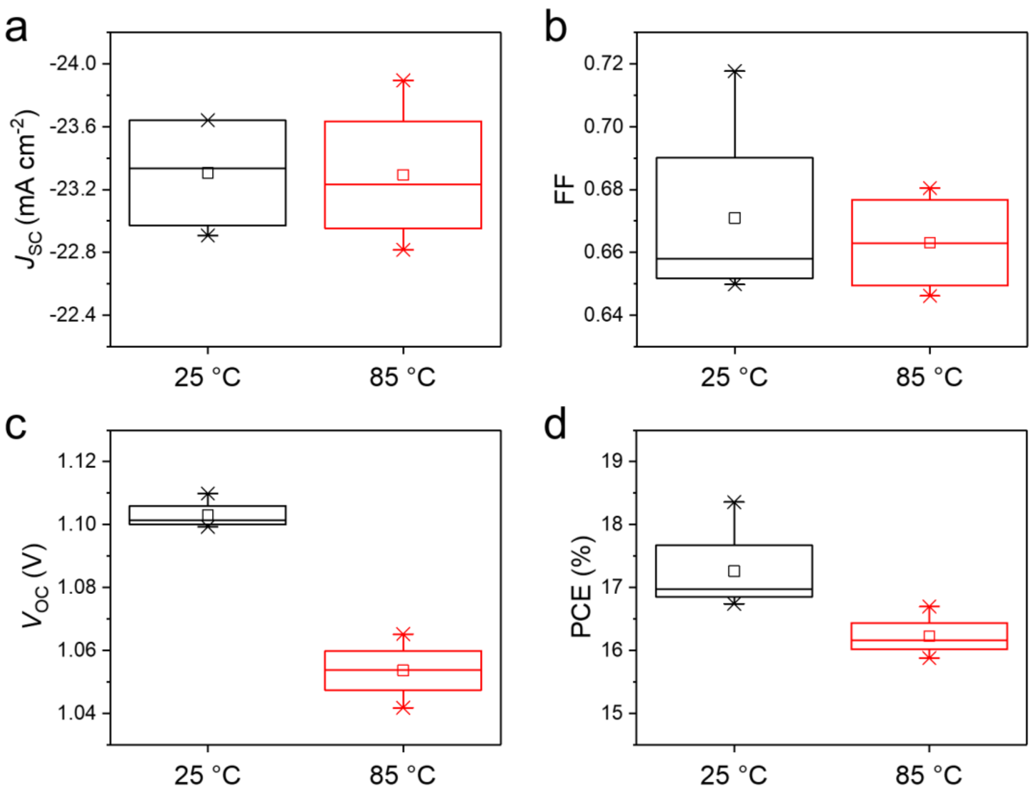

Figure 4-8. Device performance of PSCs, in which the perovskite films stored at different temperatures of 25 (black) or 85 °C (red) before deposition of spiro-OMeTAD and Au electrodes.

Since it is difficult to suppress the iodine release from the iodine-containing perovskite films at high temperature, I tried to block the iodine penetration into the spiro-OMeTAD layer by adding an iodine-blocking layer at the perovskite/spiro-OMeTAD interface. For the iodine-blocking layer, I used a thin lithium fluoride (LiF), polymethylmethacrylate (PMMA), or nickel oxide (NiO_x) nanoparticle layer. NiO_x nanoparticles have been used as the HTL of PSCs.[34] The LiF layer was prepared by thermal evaporation under vacuum. The deposition rate and pressure were the same as those we used for the Au deposition. A PMMA layer was deposited by spin-coating from a 5 or 10 mg ml^{-1} solution in CB at 1,000 rpm for 30 sec. NiO_x nanoparticles were synthesized according to literature.[32] The synthesized NiO_x nanoparticles were dissolved in a mixture of CB and oleic acid (1 : 0.01 by volume).[52] The NiO_x thin layer was deposited by spin-coating from this solution at 1,000 rpm for 30 sec. The spin-coated PMMA and NiO_x thin layers were annealed at 100 °C for 10 min.

The use of these blocking layers decreased the initial PCEs as shown in **Fig. 4-9**(a–c), probably because of the inefficient hole extraction. Besides the decrease of initial PCEs, importantly, the high-temperature stability was improved with these blocking layers as shown in **Fig. 4-9**(d–f). Increasing the thickness of the PMMA or LiF blocking layer increased the high-temperature stability. Based on these results, I infer that introducing the concept of using the iodine-blocking layer has a potential of improving the high-temperature stability of PSCs. In my future study, I will look for a more effective blocking layer to obtain the compatibility of high-temperature stability and high PCEs.

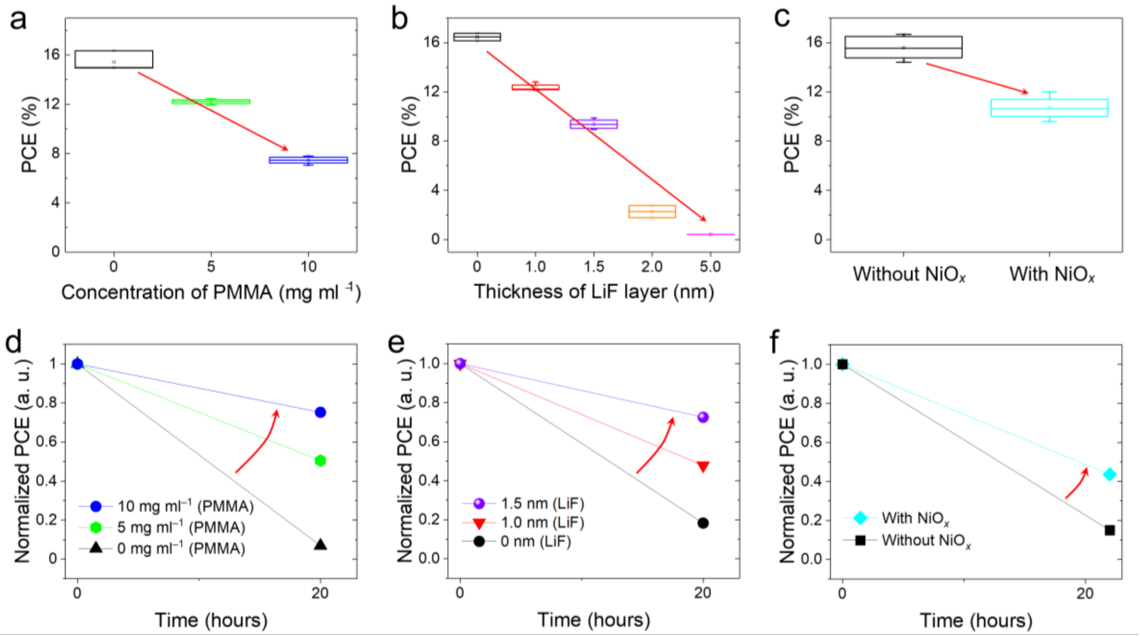

Figure 4-9. a–c) Plots of PCEs of PSCs as a function of thickness of a) PMMA, b) LiF, and c) NiO_x blocking layers. d–f) Dark storage stability at 85 °C for PSCs with an iodine-blocking layer of d) PMMA, e) LiF, or f) NiO_x

To avoid the detrimental effect of the iodine doping into spiro-OMeTAD, I chose the 100% bromine-based formamidinium lead tribromide ($FAPbBr_3$) based perovskite as the light absorber for the fabrication of PSCs. The device architecture was the same as the aforementioned iodine-based PSC architecture except the perovskite composition. For the fabrication of the $FAPbBr_3$ perovskite film, 1.2 M of formamidinium bromide (FABr) and 1.2 M of $PbBr_2$ were dissolved in DMSO to prepare a precursor solution. The $FAPbBr_3$ perovskite film was spin-coated on the SnO_2 surface from this solution at 4,000 rpm for 30 sec. Five seconds before the end of the substrate rotation, 120 μl of chlorobenzene was dropped onto the spinning substrate. Subsequently, this perovskite layer was annealed at 140 °C for 20 min. The other PSC fabrication conditions were the same as those described in Chapter 2.

Figure 4-10a shows the PCEs of iodine-free PSCs. The average PCEs were ~5%. These low PCEs of iodine-free PSCs compared than that of iodine-based PSCs with PCEs of ~18% (**Fig. 4-1**b) are assigned to wide band gap (2.2 eV) of iodine-free $FAPbBr_3$ perovskite absorber. Indeed, the J_{SC} of PSCs was very low about ~7 mA cm^{-2} (**Fig. 4-10**b).

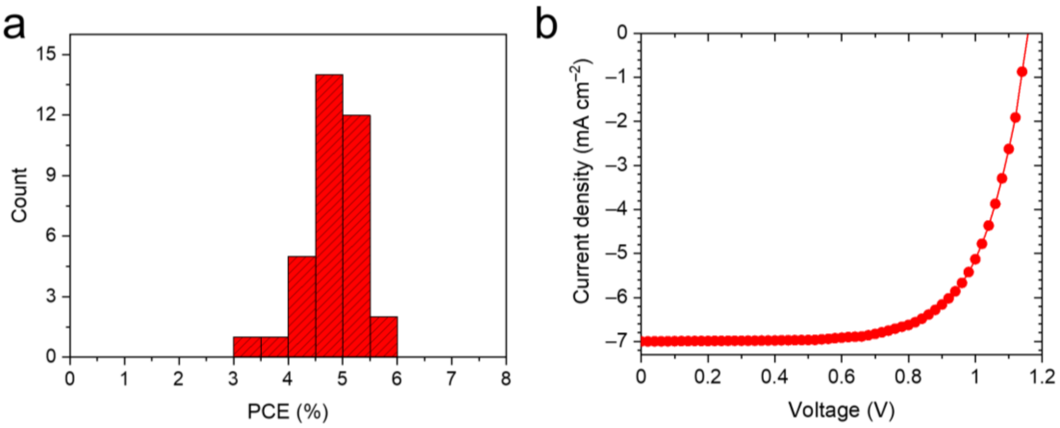

Figure 4-10. a) PCEs' statistics of iodine-free PSCs operated in the forward and reverse bias scans. b) $J-V$ curves of a representative iodine-free PSC that had the highest PCE.

Next, I checked the stability of iodine-free PSCs at high temperature. **Figure 4-11**a reveals that the high-temperature stability at 85 °C was much better for iodine-free PSCs than for iodine-based PSCs (**Fig. 4-1**c) although the spiro-OMeTAD HTL was included in both the architectures. In contrast to the previously discussed results regarding the iodine-based perovskite, the HOMO level of the spiro-OMeTAD layer fabricated on the iodine-free perovskite was unchanged at −5.3 eV (**Fig. 4-11**b) and an increase in PL intensity of the iodine-free perovskite was not observed after 180 hours of heating at 85 °C (**Fig. 4-11**c). These results indicate that using iodine-free perovskites leads to the high-temperature stability because of the absence of the detrimental iodine release.

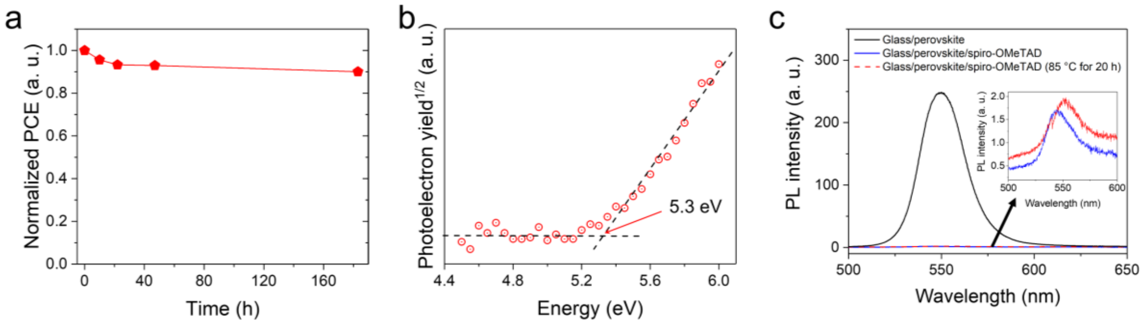

Figure 4-11. a) Dark stability of iodine-free PSCs at 85 °C. b) Photoelectron yield spectroscopy results of the spiro-OMeTAD layer prepared on the iodine-free perovskite layer and stored after 180 hours of heating at 85 °C. c) Steady-state PL spectra of iodine-free perovskite/spiro-OMeTAD samples. The inset in (c) shows the magnified PL spectra.

4.3 Conclusions

I investigated the high-temperature degradation of PSCs with the spiro-OMeTAD HTL in detail. I found that post-doping of spiro-OMeTAD with iodine, which comes from the perovskite layer at high temperature, is one possible issue that accelerates the PSC degradation. The iodine doping increased the HOMO level of spiro-OMeTAD to −5.8 eV from original −5.3 eV and, therefore, formed the hole extraction barrier at the perovskite/spiro-OMeTAD interface. I demonstrated that covering the perovskite layer with an iodine-blocking layer or using an iodine-free perovskite as the light absorber is effective in suppressing the high-temperature degradation. Thus, this work sheds light upon the high-temperature degradation mechanism of PSCs with spiro-OMeTAD and suggests new strategies for the fabrication of stable spiro-OMeTAD-based PSCs.

References

[1] N. J. Jeon, H. Na, E. H. Jung, T. Y. Yang, Y. G. Lee, G. Kim, H. W. Shin, S. Il Seok, J. Lee, J. Seo, *Nat. Energy* **2018**, *3*, 682.

[2] Q. Jiang, Y. Zhao, X. Zhang, X. Yang, Y. Chen, Z. Chu, Q. Ye, X. Li, Z. Yin, J. You, *Nat. Photonics* **2019**, *13*, 460.

[3] H. Min, M. Kim, S. U. Lee, H. Kim, G. Kim, K. Choi, J. H. Lee, S. Il Seok, *Science* **2019**, *366*, 749.

[4] H. S. Kim, C. R. Lee, J. H. Im, K. B. Lee, T. Moehl, A. Marchioro, S. J. Moon, R. Humphry-Baker, J. H. Yum, J. E. Moser, M. Grätzel, N. G. Park, *Sci. Rep.* **2012**, *2*, 591.

[5] T. H. Schloemer, J. A. Christians, J. M. Luther, A. Sellinger, *Chem. Sci.* **2019**, *10*, 1904.

[6] H. D. Pham, Z. Wu, L. K. Ono, S. Manzhos, K. Feron, N. Motta, Y. Qi, P. Sonar, *Adv. Electron. Mater.* **2017**, *3*, 1700139.

[7] T. H. Schloemer, T. S. Gehan, J. A. Christians, D. G. Mitchell, A. Dixon, Z. Li, K. Zhu, J. J. Berry, J. M. Luther, A. Sellinger, *ACS Energy Lett.* **2019**, *4*, 473.

[8] Y. C. Kim, T. Y. Yang, N. J. Jeon, J. Im, S. Jang, T. J. Shin, H. W. Shin, S. Kim, E. Lee, S. Kim, J. H. Noh, S. I. Seok, J. Seo, *Energy Environ. Sci.* **2017**, *10*, 2109.

[9] T. Duong, J. Peng, D. Walter, J. Xiang, H. Shen, D. Chugh, M. Lockrey, D. Zhong, J. Li, K. Weber, T. P. White, K. R. Catchpole, *ACS Energy Lett.* **2018**, *3*, 2441.

[10] K. Choi, J. Lee, H. Il Kim, C. W. Park, G. W. Kim, H. Choi, S. Park, S. A. Park, T. Park, *Energy Environ. Sci.* **2018**, *11*, 3238.

[11] S. W. Tong, J. Balapanuru, D. Fu, K. P. Loh, *ACS Appl. Mater. Interfaces* **2016**, *8*, 29496.

[12] L. Meng, C. Sun, R. Wang, W. Huang, Z. Zhao, P. Sun, T. Huang, J. Xue, J. W. Lee, C. Zhu, Y. Huang, Y. Li, Y. Yang, *J. Am. Chem. Soc.* **2018**, *140*, 17255.

[13] N. Arora, M. I. Dar, A. Hinderhofer, N. Pellet, F. Schreiber, S. M. Zakeeruddin, M. Grätzel, *Science* **2017**, *358*, 768.

[14] S. S. Mali, J. V. Patil, H. Kim, R. Luque, C. K. Hong, *Mater. Today* **2019**, *26*, 8.

[15] J. Cao, H. Yu, S. Zhou, M. Qin, T. K. Lau, X. Lu, N. Zhao, C. P. Wong, *J. Mater. Chem. A* **2017**, *5*, 11071.

[16] M. Saliba, T. Matsui, J. Y. Seo, K. Domanski, J. P. Correa-Baena, M. K. Nazeeruddin, S. M. Zakeeruddin, W. Tress, A. Abate, A. Hagfeldt, M. Grätzel, *Energy Environ. Sci.* **2016**, *9*, 1989.

[17] X. Zhao, H. S. Kim, J. Y. Seo, N. G. Park, *ACS Appl. Mater. Interfaces* **2017**, *9*, 7148.

[18] A. K. Jena, Y. Numata, M. Ikegami, T. Miyasaka, *J. Mater. Chem. A* **2018**, *6*, 2219.

[19] A. K. Jena, M. Ikegami, T. Miyasaka, *ACS Energy Lett.* **2017**, *2*, 1760.

[20] K. Domanski, J. P. Correa-Baena, N. Mine, M. K. Nazeeruddin, A. Abate, M. Saliba, W. Tress, A. Hagfeldt, M. Grätzel, *ACS Nano* **2016**, *10*, 6306.

[21] T. Malinauskas, D. Tomkute-Luksiene, R. Sens, M. Daskeviciene, R. Send, H. Wonneberger, V. Jankauskas, I. Bruder, V. Getautis, *ACS Appl. Mater. Interfaces* **2015**, *7*, 11107.

[22] I. Mesquita, L. Andrade, A. Mendes, *ChemSusChem* **2019**, *12*, 2186.

[23] J. Y. Seo, H. S. Kim, S. Akin, M. Stojanovic, E. Simon, M. Fleischer, A. Hagfeldt, S. M. Zakeeruddin, M. Grätzel, *Energy Environ. Sci.* **2018**, *11*, 2985.

[24] S. Kim, S. Bae, S. W. Lee, K. Cho, K. D. Lee, H. Kim, S. Park, G. Kwon, S. W. Ahn, H. M. Lee, Y. Kang, H. S. Lee, D. Kim, *Sci. Rep.* **2017**, *7*, 1200.

[25] E. J. Juarez-Perez, L. K. Ono, M. Maeda, Y. Jiang, Z. Hawash, Y. Qi, *J. Mater. Chem. A* **2018**, *6*, 9604.

[26] F. Fu, S. Pisoni, Q. Jeangros, J. Sastre-Pellicer, M. Kawecki, A. Paracchino, T. Moser, J. Werner, C. Andres, L. Duchêne, P. Fiala, M. Rawlence, S. Nicolay, C. Ballif, A. N. Tiwari, S. Buecheler, *Energy Environ. Sci.* **2019**, *12*, 3074.

[27] Kaiho, T. Iodine chemistry and applications. 8–14, John Wiley & Sons (2015) ISBN:9781118466292.

[28] S. Wang, Y. Jiang, E. J. Juarez-Perez, L. K. Ono, Y. Qi, *Nat. Energy* **2017**, *2*, 16195.

[29] P. Yuan, J. Wu, W. Sun, Q. Zhu, M. Zhang, J. Zou, X. Wang, X. Liu, Y. Yang, Z. Lan, *Energy Technol*. **2020**, *8*, 1901171.

[30] G. Boschloo, A. Hagfeldt, *Acc. Chem. Res.* **2009**, *42*, 1819.

[31] J. Datta, A. Bhattacharya, K. K. Kundu, *Bull. Chem. Soc. Jpn.* **1988**, *61*, 1735.

[32] J. J. Custer, S. Natelson, *Anal. Chem.* **1949**, *21*, 1005.

[33] G. Y. Kim, A. Senocrate, T. Y. Yang, G. Gregori, M. Grätzel, J. Maier, *Nat. Mater.* **2018**, *17*, 445.

[34] J. Tirado, M. Vásquez-Montoya, C. Roldán-Carmona, M. Ralaiarisoa, N. Koch, M. K. Nazeeruddin, F. Jaramillo, *ACS Appl. Energy Mater.* **2019**, *2*, 4890.

Chapter 5

Conclusions and perspective

The work presented in this thesis focused on clarifying the light, ion migration and temperature induced degradation mechanisms of PSCs. Below are my findings obtained in this thesis:

In **Chapter 2**, I have revealed that excess PbI_2 crystals accelerate the light-induced degradation of PSCs. It was possible to improve the stability by reducing excess PbI_2 in perovskite films. The PCEs of PSCs, in which excess PbI_2 crystals were not present, retained 99% of their initial values after 520 h of continuous illumination while the PCEs of PSCs with excess PbI_2 crystals reduced to 47% of the initial value. The degradation of PSCs was related to the photo-degradation of excess PbI_2 crystals into metallic Pb and I_2 under light illumination. Interestingly, metallic Pb was formed at the interface of SnO_2 and perovskite only. The generated Pb acted as a quencher for carriers, which gradually made the PCEs lower.

In **Chapter 3**, I found that the migration of positive ions and successive localization caused by hydroxyl groups (–OH) existing at the SnO_2 surface is one of the critical reasons for the *J*–*V* hysteresis and degradation of PSCs. In addition, this localization of positive ions trapped electrons, perhaps inducing the metallic Pb formed at the interface of the SnO_2 layer and the perovskite layer. I suppressed the *J*–*V* hysteresis and degradation by chemically modifying the SnO_2 surface with a SAM. I obtained almost no degradation in PSCs with a SAM after 1,000 hours of continuous illumination.

In **Chapter 4**, I investigated the degradation mechanism of PSCs at high temperature. I observed that PSCs with the spiro-OMeTAD HTL degraded very quickly at a high temperature of 85 °C. One of the origins of this degradation at the high temperature was the post-doping of spiro-OMeTAD with iodine, which originated from the perovskite layer at high temperature. The iodine doping increased the HOMO level of spiro-OMeTAD to −5.8 eV from original −5.3 eV and, therefore, formed the hole extraction barrier at the perovskite/spiro-OMeTAD interface. I demonstrated that covering the perovskite layer with an iodine-blocking layer is effective in suppressing the high-temperature degradation. Furthermore, I used an iodine-free perovskite as the light absorber to clarify the high-temperature degradation because of the absence of detrimental iodine.

Overall, I studied the light, ion migration and temperature induced degradation mechanisms of PSCs. By understanding the mechanisms, I engineered the PSCs and obtained very stable PSCs under continuous illumination at room temperature, which is one of the best stability reported so far. Furthermore, I established the basic idea for fabricating stable PSCs with spiro-OMeTAD even at high temperature.

Based on my results in this thesis, I can estimate the lifetime, at which efficiency decreases to 80% of the initial under continuous illumination, of my PSCs at 13,000 h (**Fig. 5-1**a). This value roughly corresponds to 1.5 years. I would like to continue studying the degradation of PSCs to improve the lifetime from present 1.5 to ~20 years required for practical use. In addition, measuring the stability of PSCs with accelerated testing methods such as under concentrated sun light would be helpful to estimate stability of very long duration. On the other hand, analyzing degradation mechanisms at high temperature as well as developing stable PSCs at high temperature are still required. I found that the detrimental iodine gas is the potential source of the degradation at high temperature. It is possible to inhibit the high-temperature degradation by using the concept of the iodine blocking layers. In this regard, if even higher quality perovskite films, such as single-crystal films, can be obtained, detrimental iodine release may be suppressed. I will pursue such higher quality films by optimizing or developing the perovskite compositions. In addition, developing a more effective iodine blocking layer to obtain even better high-temperature stability without decreasing PCEs would be useful. On the other hand, instead of spiro-OMeTAD, developing new HTL materials, which are robust and chemically inert to detrimental iodine, will be another purpose of my future study to fasten the commercialization of PSC technology. In contrast, the study on the improvement of PCE towards the theoretical limit of 33% is highly desirable. To further increase the PCE, passivation of defects at the surface of perovskite layers should be important, because such defects strongly behave as carrier recombination centers or carrier traps. On the other hand, tandem structured solar cells combining a PSC with other solar cell such as silicon are emerging for more efficient harvesting of solar energy (**Fig. 5-1**b), since the Si-based absorber has the narrow bandgap about ~1.2 eV, and indeed, it absorbs solar energy at longer wavelengths. The bandgap of the perovskite absorber is easy to tune by changing the chemical composition, and it can be used as the absorber layer to receive solar energy at shorter wavelengths. Thus, by combining these absorbers, I can deliver high PCE, leading to more energy aimed for various new solar cell applications.

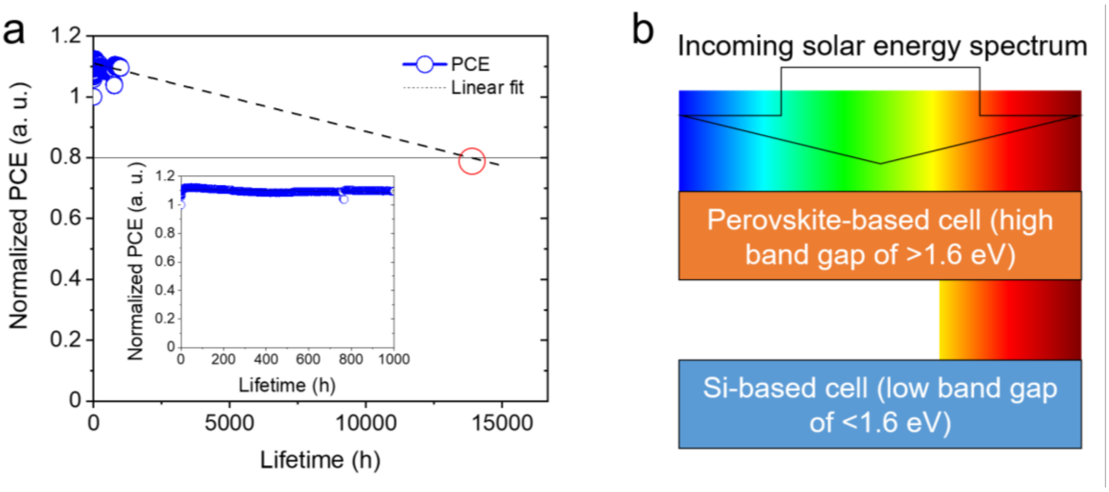

Figure 5-1. a) Estimated lifetime of the best device. The inset shows the original data b) A tandem structure for high efficiency solar cell in future study.

List of symbols

t	Goldschmidt tolerance factor
r	Radius of ion
q	Charge of ion
k	Boltzmann constant
Ω	Resistance
α	Photoactive cubic phase
δ	Photoinactive hexagonal phase
θ	Angle
°	Degree
°C	Degrees of Celsius
σ	Electrical conductivity
E_a	Activation energy
eV	Electron volt
J	Current density
I	Current
V	Voltage
P	Power
T	Temperature
T_g	Glass transition temperature
J_SC	Short-circuit current density
J_max	Maximum current density
V_OC	Open-circuit voltage
V_max	Maximum voltage

List of abbreviation

3D	Three-dimensional
2D	Two-dimensional
OILH	Organic-inorganic lead halide
VBM	Valence band maxima
CBM	Conduction band minima
HOMO	Highest occupied molecular orbital
LUMO	Lowest unoccupied molecular orbital
WF	Work function
PSC	Perovskite solar cell
PCE	Power conversion efficiency
MPP	Maximum power point
FF	Fill factor
ETL	Electron transport layer
HTL	Hole transport layer
TiO_2	Titanium dioxide
SnO_2	Tin oxide
spiro-OMeTAD	2,2',7,7'-Tetrakis[*N*,*N*-di(4-methoxyphenyl)amino]-9,9'-spirobifluorene
PEDOT: PSS	Poly(3,4-ethylenedioxythiophene) polystyrene sulfonate
MA	Methylammonium
MAI	Methylammonium iodide
MABr	Methylammonium bromide
$MAPbI_3$	Methylammonium lead triiodide
FA	Formamidinium
FAI	Formamidinium iodide

$FAPbBr_3$	Formamidinium lead tribromide
CsI	Cesium iodide
$PbBr_2$	Lead bromide
PbI_2	Lead iodide
C_{60}	Fullerene
CPTA	C_{60} pyrrolidine tris-acid
LiTFSI	Lithium bis(trifluoromethanesulfonyl)imide
4-tBP	4-Tert-butylpyridine
FK-209.	Tris(2-(1H-pyrazol-1-yl)-4-*tert*-butylpyridine)cobalt(III)tri[bis(trifluoromethane) sulfonimide]
PMMA	Polymethylmethacrylate
LiF	Lithium fluoride
NiO_x	Nickel oxide nanoparticle
DMF	*N,N*-dimethylformamide
DMSO	Dimethyl sulfoxide
CB	Chlorobenzene
PTFE	Polytetrafluoroethylene
PL	Photoluminescence
SEM	Scanning electron microscope images
XRD	X-ray diffraction patterns
XPS	X-ray photoelectron spectroscopy
EDS	Energy Dispersive Spectroscopy
–OH	Hydroxyl groups
SAM	Self-assembled monolayer
HI	Hysteresis Index
EIS	Electrochemical impedance spectroscopy
DSC	Differential scanning calorimetry
MALDI–TOF–MS	Matrix assisted laser desorption/ionization-time of flight-mass spectrometry

Publication list

Original Papers:

1. G. Tumen-Ulzii, C. Qin, D. Klotz, M. R. Leyden, P. Wang, M. Auffray, T. Fujihara, T. Matsushima, J-W. Lee, S-J. Lee, Y. Yang, C. Adachi, *Advanced Materials*, **32**, 1905035 (2020).

2. G. Tumen-Ulzii, T. Matsushima, D. Klotz, M. R. Leyden, P. Wang, C. Qin, J-W. Lee, S-J. Lee, Y. Yang, C. Adachi, *Communications Materials* **1***,* 31 (2020). https://doi.org/10.1038/s43246-020-0028-z

3. G. Tumen-Ulzii, C. Qin, D. Klotz, M. R. Leyden, T. Matsushima, C. Adachi, *Solar RRL,* (2020) (submitted).

4. G. Tumen-Ulzii, T. Matsushima, D. Klotz, C. Adachi, *Applied Physics Letters,* (2020) (submitted).

Joint Papers:

5. D. Klotz, G. Tumen-Ulzii, C. Qin, T. Matsushima, C. Adachi, *RSC Advances*, **9** (57), 33436–33445 (2019).

6. S. Watanabe, T. Cheng, G. Tumen-Ulzii, C. Qin, T. Matsushima, C. Adachi, *Applied Physics Letters*, **115**, 233502 (2019)

7. T. Cheng, G. Tumen-Ulzii, D. Klotz, S. Watanabe, T. Matsushima, C. Adachi, *ACS Applied Materials and Interfaces*, (2020) (accepted). https://doi.org/10.1021/acsami.0c06737

Patent:

1. G. Tumen-Ulzii, C. Qin, T. Matsushima, C. Adachi, Methods for Improving Stability of Perovskite Solar Cells and Perovskite Solar Cells Having Improved Stability. Japanese patent, JP2019-95479.

Conference presentations:

1. G. Tumen-Ulzii, C. Qin, D. Klotz, T. Matsushima, C. Adachi, *Asian Conference on Organic Electronic-2019*, Taipei, Taiwan (November 07, 2019). (Poster presentation)

2. G. Tumen-Ulzii, C. Qin, D. Klotz, T. Matsushima, C. Adachi, *Asia-Pacific International Conference on Perovskite, Organic Photovoltaics and Optoelectronics-2020*, Tsukuba, Japan (January 21, 2020). (Oral presentation)

3. G. Tumen-Ulzii, T. Matsushima, D. Klotz, C. Qin, C. Adachi, *Asia-Pacific International Conference on Perovskite, Organic Photovoltaics and Optoelectronics-2020*, Tsukuba, Japan (January 20, 2020). (Poster presentation)

Acknowledgements

First of all, I am deeply grateful to Professor Chihaya Adachi for allowing me to study for Ph.D. degree in his fascinating laboratory. He has been supporting me continuously by supervising my research work and providing outstanding experimental environment. I was able to obtain the experimental results shown in this thesis with his great support. With his support, I have worked hard as possible as I can. Furthermore, he always supports my family, and therefore, I and my family have enjoyed wonderful Japanese life in Fukuoka city.

I am also deeply grateful to the members of thesis defense committee, Professor Katsuro Hayashi and Professor Yuji Oki for their insightful comments and suggestions on my presentation and thesis.

I would like to express my deep gratitude to Professor Toshinori Matsushima for teaching me how to do research work. Usually, his questions and comments were very difficult to me because of my shallow knowledge. When I look back, it was great chance to learn many things by trying to find answers to his comments.

Also, I would like to express my deep gratitude to Professor Chuanjiang Qin, who led me to work on this topic and now he belongs to Changchun Institute of Science, China. He always used to tell me that “do not stop doing experiment”. You should do experiment at least 2 times per week. I think it was great advice for me to learn something new during my experiment.

I would like to express my deep gratitude to Associate Professor Hajime Nakanotani for his kind advice on my research work and his support on the classes and lectures at the department.

I would like to thank Dr. Dino Klotz, Dr. Matthew Leyden, Dr. Sung-Joon Lee and Professor Jin-Wook Lee and Professor Yang Yang for their kind collaboration on my research work.

I also would like to specially thank all of the members at Adachi lab (OPERA) for their kind support on my life, study and experiments. I especially thank Ms. Sachiko Higashikawa, Ms. Hiroko Kuratomi, Ms. Mayumi Kudo, Ms. Rei Sasagawa and Ms. Haruna Kato for their kind support on study and life in Japan.

Furthermore, I would like to thank Ministry of Education, Culture, Sports, Science and Technology (MEXT) and Japan Science and Technology Agency (JST), ERATO, Adachi Molecular Exciton Engineering Project for financially support.

I would also like to express my deep gratitude to all of members of my family for their continuous support and unchanged love. Especially, I would like to express my deep gratitude to my wife and son for their love and support, and also for their patience in my terrific research schedule for last 3 years.

July, 2020

Ganbaatar Tumen-Ulzii